JDSC | AMESDYC

e-ISSN: 3122-4326

Journal of Dynamical Systems and Complexity

SELECTED PAPERS | VOL. 1, NUMBER 3 | JULY–OCTOBER 2026

1. Convex Hull as a method for Characterizing Chaotic Systems

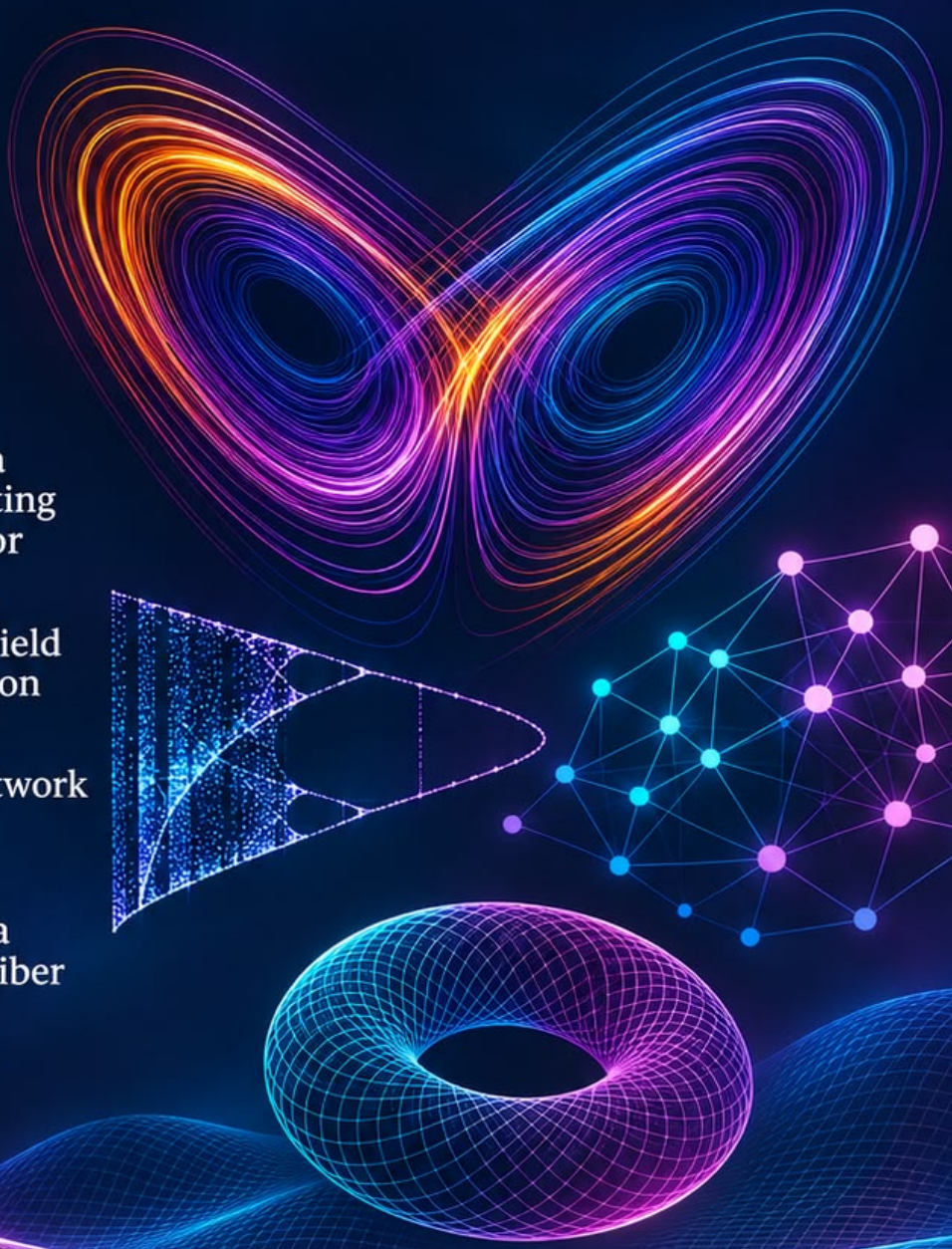
2. A Simple Gaussian Filter can Protect Images of Noise Injection in a Classification Task with Deep Neural Networks

3. Experimental Evaluation of a Hartley Oscillator Incorporating a Commercial SDC Memristor

4. Convergence Analysis of the Kuramoto Model via Mean-Field Coupling for Micro-Generation Networks

5. Physics-Informed Neural Network for Sparse-Sensor Inverse Heat Conduction

6. Noise-Induced Dynamics in a Multistable Erbium-Doped Fiber Laser: A Short Review From Extreme Events to Photonic Information Processing



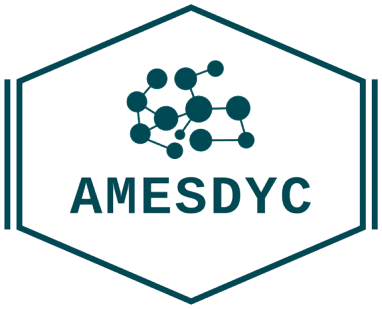
NONLINEAR DYNAMICS | COMPLEX SYSTEMS | MACHINE LEARNING | NETWORKS | PHOTONICS



Journal of Dynamical Systems and Complexity

Vol. 1 No. 3 (2026): Selected papers 2026

Edited by:
Esteban Tlelo Cuautle, and Guillermo Huerta Cuéllar



Asociación Mexicana de Sistemas Dinámicos y Complejidad

Journal of Dynamical Systems and Complexity
Vol. 1 No. 3 (2026): Selected papers 2026

Edited by:
Esteban Tlelo Cuautle, and Guillermo Huerta Cuéllar

JOURNAL OF DYNAMICAL SYSTEMS AND COMPLEXITY, year 1, issue 3, July 2026-October 2026. JDSC is a four-month Journal published by Asociación Mexicana de Sistemas Dinámicos y Complejidad, A. C. Rubí 20, Colinas de San Javier, Lagos de Moreno, Jalisco, México, C.P. 47463. https://sistemasdinamicos.amesdyc.org, e-mail: ediesca.conference@amesdyc.org.mx. Chief Editor: Esteban Tlelo Cuautle. INDAUTOR Certificate of Reserve: 04-2025-092411114800-102, e-ISSN: 3122-4326, by Instituto Nacional del Derecho de Autor. Responsible for the last update of this issue, technical staff of Asociación Mexicana de Sistemas Dinámicos y Complejidad, A. C., Rubí 20, Colinas de San Javier, Lagos de Moreno, Jalisco, México, C.P. 47463. Date of last modification, July 1st, 2026.

© 2026 Asociación Mexicana de Sistemas Dinámicos y Complejidad (AMESDYC)
Lagos de Moreno, Jalisco, México.

Rights Reserved
Total or partial reproduction of this work by any means or procedure is prohibited without the prior written authorization of AMESDYC and the editors of the Journal of Dynamical Systems and Complexity.

Impreso en México / *Printed in Mexico*

About the Journal

Journal of Dynamical Systems and Complexity (JDSC) is a multidisciplinary, peer-reviewed international journal published triannually (every four months) by the Asociación Mexicana de Sistemas Dinámicos y Complejidad, A. C. Under the leadership of Editor-in-Chief Dr. Esteban Tlelo-Cuautle, the journal serves as a specialized forum for researchers and practitioners in fields such as applied mathematics, multidisciplinary physics, engineering, robotics, and control systems.

JDSC is dedicated to advancing the knowledge of both linear and nonlinear dynamical systems. We welcome high-quality contributions, including original research articles, comprehensive reviews, and brief communications. Our scope covers theoretical developments, numerical simulations, computational algorithms, and experimental methods, with a particular interest in emerging phenomena in complex systems.

To ensure scientific excellence, JDSC employs a rigorous peer-review process. By submitting a manuscript, authors certify that their work is original and not under consideration elsewhere. The journal adheres to high ethical standards; the content and accuracy of published papers are the sole responsibility of the authors.

In our commitment to global scientific dissemination, JDSC is published exclusively in English. We operate under an Open Access model, authorizing the full or partial reproduction of articles for academic purposes, provided that the original work is properly cited.

Esteban Tlelo Cuautle
Guillermo Huerta Cuellar
October 2026

Contents

1 Convex Hull as a method for Characterizing Chaotic Systems 1

2 A Simple Gaussian Filter can Protect Images of Noise Injection in a Classification Task with Deep Neural Networks 11

3 Experimental Evaluation of a Hartley Oscillator Incorporating a Commercial SDC Memristor 23

4 Convergence Analysis of the Kuramoto Model via Mean-Field Coupling for Micro-Generation Networks 36

5 Physics-Informed Neural Network for Sparse-Sensor Inverse Heat Conduction 50

6 Noise-Induced Dynamics in a Multistable Erbium-Doped Fiber Laser: A Short Review From Extreme Events to Photonic Information Processing 60

Editorial Board 80

Instructions for Authors 83

Journal of Dynamical Systems and Complexity (202X) vol.1(3) 1-10
eISSN: 3122-4326, DOI: 10.66131/JDSC1320261-10

Convex Hull as a Method for Characterizing Chaotic Systems

J.L. Echenuasía-Monroy[1*], G. Huerta-Cuellar[2], H.E. Gilardi-Velázquez[3], J.R. Cuesta-García[1], J. Álvarez[1*]

[1] Applied Physics Division, Department of Electronics and Telecommunications, CICESE, Carr. Ensenada-Tijuana 3918, Zona Playitas, Ensenada, 22860, BC, Mexico.
[2] Centro Universitario de los Lagos, Universidad de Guadalajara, Enrique Díaz de León 1144, Paseos de la Montaña, Lagos de Moreno 47460, Mexico.
[3] Facultad de Ingeniería, Universidad Panamericana, Josemaría Escrivá de Balaguer 101, Aguascalientes 20290, MX, Mexico.

Abstract

This work introduces a geometric-quantitative characterization of chaotic attractors based on the convex hull of their phase-space representation. In contrast to the classical dynamical characterization — based on time-series descriptors such as Lyapunov exponents, Kaplan-Yorke and fractal dimensions, which quantify the temporal signature of chaos — the proposed characterization treats the attractor as a spatial object and quantifies its global extent through the area of its 2D projections and its total volume in phase space. The methodology is applied to two families of chaotic systems: three variants of the Chua oscillator sharing the double-scroll topology, and a piecewise-linear jerk system generating a nine-scroll attractor under integer- and fractional-order dynamics. In every case, the classical descriptors confirm that the systems remain qualitatively equivalent in their chaotic behavior, while the convex-hull descriptors reveal deformations of one to two orders of magnitude that the classical metrics overlook. We formalize this observation as a proposition establishing the independence of the geometric descriptors from the classical dynamical ones. The proposed characterization is complementary rather than alternative to the classical one, and provides a criterion to discriminate between chaotic systems precisely in the regime where topology, Lyapunov spectrum, and fractal dimensions are inconclusive, a regime particularly relevant for engineering applications where amplitude constraints are decisive.

Keywords— Chaotic attractor, chaos, dynamical systems, fractal dimension, convex hull.

1 Introduction

The history of chaos is not a history of mere randomness, but of hidden patterns in complexity, of deterministic systems whose trajectories are so sensitive to initial conditions that their long-term behavior seems profoundly unpredictable. For centuries, this phenomenon has been observed only anecdotally (in unpredictable swirls of smoke, unpredictable drips of a faucet, or grand, unruly movements of celestial bodies) and was dismissed as either too complicated to quantify or too insignificant to study [1, 2, 3].

The search for an understanding of chaos often shifted from the abstract world of mathematics to the tangible world of physics. For decades, strange attractors like those of Lorenz and Rössler were mathematical phantoms, observed in computer simulations of differential equations, but never actually put into practice. They described the weather and chemical reactions– complex, diffuse systems that are difficult to control or isolate. The Chua attractor story is about how chaos was finally tangible, engineered, and clearly manifested in a simple, predictable way via a simple electronic circuit. It is the chronicle of a theoretical prediction that became a physical reality and revolutionized the study of nonlinear dynamics by serving as a perfect laboratory specimen [4].

The story begins not in a laboratory, but at the University of California, Berkeley, in the mind of an electrical engineer named Leon O. Chua. In the early 1980s, Chua was a leading figure in non-linear circuit theory. He had previously formulated a theoretical basis for a new, simpler type of chaotic circuit. Chua's key insight was a conjecture: that a chaotic attractor, the most complex behavior a dynamical system can exhibit, can be generated by an autonomous circuit containing only three simple, standard components: resistors (R), capacitors (C), and inductors (L), combined with a single non-linear element [5, 6, 7, 8]. This nonlinear element was Chua's own invention: the Chua diode. It was not a typical diode but an active circuit element with a precisely designed, piecewise-linear

*Corresponding author: jqalvar@cicese.edu.mx, echenausia@cicese.edu.mx
Received: September 5, 2025, **Published:** October 31, 2026
Editor: J. M. Muñoz-Pacheco

current-voltage characteristic. Its curve resembled a zigzag line with three segments. This deliberate, simplified non-linearity was the decisive factor. Unlike the complex, smooth nonlinearities found in fluid systems or population models, Chua's diode was designed to be mathematically tractable. In a seminal 1986 paper, Chua and his student T. Matsumoto theorized this circuit and proved that it should exhibit chaos. They provided the mathematical equations and the computer-simulated attractor, a double-scroll structure that appeared to orbit around two distinct wells.

Remark 1.0.1. *The anecdote about the first time the Chua circuit was connected says that when they set everything up and turned on the power, the output of the circuit should have shown a periodic oscillation or a static voltage. Instead, the oscilloscope screen showed a persistent, dynamic, and never-repeating pattern-a chaotic signal. They adjusted the knobs on the variable resistor and the pattern changed, going through a series of dynamical behaviors: from stable points to periodic cycles to the characteristic chaotic double-scroll attractor. At that moment, the abstract mathematical phantom of chaos became a physical and electronic reality. The Chua circuit was born and the Chua attractor was revealed to the world.*

The decisive moment of confirmation came not from Chua's own laboratory but from a collaboration on the other side of the globe. In 1984, a young Japanese researcher, Toshimitsu Matsumoto, spent a year in Berkeley working with Chua. On his return to Waseda University in Tokyo, he commissioned his doctoral student, Makoto Komuro, to build the Chua circuit, which he realized and thus the Chua circuit was born [9]. The significance of this achievement cannot be overestimated. The researchers had a robust, affordable, and completely predictable chaotic system on their workbench for the first time. It was autonomous (it required no external signal input) and low-dimensional (only three equations of state governed it), making it mathematically simple to analyze compared to the infinite-dimensional chaos of turbulence. The circuit was so simple that undergraduate students could build it, which is still being built today. It was a milestone of chaos theory; a simple model organism that made endless experiments possible.

This physical prototype provided an unprecedented testing ground for the tools used to characterize chaos. The Chua attractor became the standard object for testing computational methods.

- **Lyapunov exponents** [10, 11]: The circuit equations enabled for the precise calculation of its Lyapunov spectrum. The researchers confirmed that it has the canonical signature of chaos: (+, 0, -). A positive exponent confirms the exponential divergence of the trajectories, a zero exponent corresponds to the direction along the flow, and a negative exponent ensures that the trajectories remain confined on the attractor. This was no longer just an output of a weather model, but a measurable electronic fact.
- **Fractal dimension** [12, 13]: The intricate scroll-like structure of the attractor seen on the oscilloscope was a clear candidate for fractal analysis. Using algorithms such as the box-counting dimension, the researchers calculated the fractal dimension of the data captured by the circuit. It was a fractional value between 2.0 and 2.2 for a standard setup. This confirmed that this physical object, generated by a real electronic circuit, had the complex, self-similar structure of a mathematical strange attractor.
- **Kaplan-Yorke Dimension** [12, 14, 15]: The Chua circuit became a prime example of the deep connection between dynamics and geometry. Using the calculated Lyapunov exponents ($\lambda_1 > 0,\ \lambda_2 = 0,\ \lambda_3 < 0$), it was possible to apply the Kaplan-Yorke formula: $D_{KY} = 2 + (\lambda_1/|\lambda_3|)$. The result agreed consistently with the directly measured fractal dimension. It provided an experimental confirmation of the assumption that a system's dynamic properties (its stretching and folding rates) directly dictate its attractor's geometric structure.

The historical development of chaos theory, from Poincaré's intuitions to the Lorenz computer to Mandelbrot's fractals and the experimental verification of the Chua circuit [11, 16, 17, 18, 19, 20], shows a fundamental path: The field matured through the development of tools to quantify the unquantifiable. The Lyapunov exponent provided the final temporal signature and defined chaos by its evolutionary behavior. Fractal geometry provided the language to describe the complex spatial structure. The Kaplan-Yorke dimension then provided a bridge between these two worlds, showing that dynamics and geometry are two sides of the same chaotic coin.

Traditional metrics for analyzing chaotic dynamical systems focus on time series and are useful to highlight characteristic aspects of chaotic behavior. However, these tools often fail to reveal subtle changes in the overall geometry of the attractor. In many cases, they are very computationally intensive, depend strongly on the quality and length of the available data, and are not always comparable to systems whose attractors have similar topological features, since the extrapolation of information limits itself to confirming the chaotic nature. Convex hull techniques offer an alternative and promising perspective. By constructing the convex hull of the projection of an attractor in phase space, one can capture geometrical changes that reflect differences in the dynamical responses of the system. The area or volume of the convex hull becomes a global quantitative descriptor of the spatial extent of the attractor and provides a complementary view to classical measurements.

This approach based on the convex hull has been shown that fractional-order chaotic systems can undergo remarkable geometric deformations. For example, the convex hull of the Rössler and Álvarez-Curiel attractors shrinks by up to 90%. Such drastic changes go unnoticed if one relies only on indicators such as the Lyapunov exponent or the fractal dimension during characterization [21].

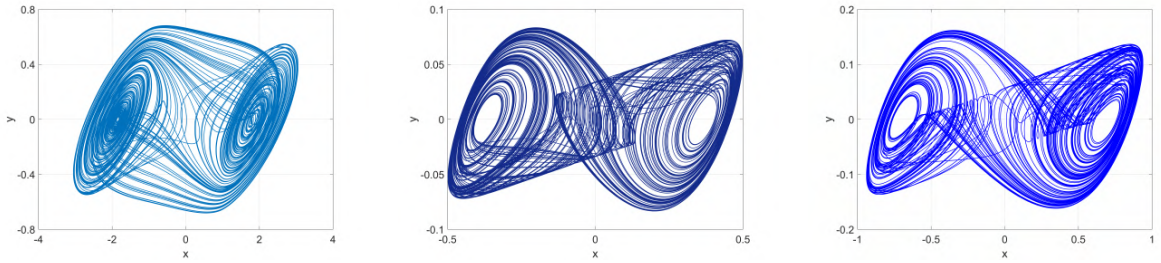
Building on this perspective, we introduce in this work what we call a *geometric-quantitative characterization* of chaotic attractors. The classical characterization of chaos is essentially *dynamical*: it describes the temporal signature of the attractor through descriptors computed from the flow, such as Lyapunov exponents, Kaplan-Yorke and fractal dimensions, and it answers the question of *how* trajectories evolve in time. The characterization proposed here is essentially *spatial*: it treats the attractor as a bounded region of phase space and quantifies *how much* of that space the attractor actually occupies, through the area of its $2D$ projections and its total $3D$ volume, computed via the convex hull. The two characterizations are not competing, they answer different questions. The dynamical one certifies that a system is chaotic and identifies its topological class; the geometric one distinguishes between chaotic systems that belong to the same class but implement it with different amplitudes, different nonlinearities, or different derivative orders. The central hypothesis of this work is that the geometric-quantitative characterization is non-redundant with respect to the classical one: two attractors can match arbitrarily closely in Lyapunov exponents, Kaplan-Yorke and fractal dimensions while differing by orders of magnitude in their convex-hull descriptors. This hypothesis is tested empirically on the Chua family in Section 4.1 and on a piecewise-linear jerk system in Section 4.2, and formalized as Proposition 5.1 in Section 5.

We address the following specific questions: are all the Chua systems, or their variants, geometrically equivalent when they are dynamically indistinguishable? Does the same phenomenon persist under fractional-order dynamics and piecewise-linear switching laws? Can the geometric discrepancies be turned into a quantitative selection criterion for engineering applications where the shape of the attractor, and not only its temporal unpredictability, is a design constraint?

The rest of the article is organized as follows. Section 2 introduces the family of Chua systems that motivate the analysis, and Section 3 formulates the problem. Section 4 develops the convex-hull methodology and applies it to the Chua family (Section 4.1) and to a piecewise-linear fractional-order jerk system (Section 4.2). Section 5 formalizes the findings as Proposition 5.1, discusses their implications, and concludes the article.

2 Preliminaries

The Chua attractor has gained great popularity for many reasons, as it was one of the first physical systems in which chaos was mathematically demonstrated [7, 8]. It is also an example of Shilnikov chaos (homoclinic orbits) [22, 23], and unlike Lorenz or Rössler [24, 25], Chua's attractor uses non-smooth nonlinearity, making it analytically tractable, yet chaotic. Chua's attractor remains a cornerstone of chaos theory due to its simplicity, robustness, and rich dynamics. For this reason, different versions and approximations of the same attractor have been described in the literature. The researchers asked *what if we change the non-linearity?* The original piecewise-linear function $f(x)$ was replaced by smoother alternatives, such as a cubic polynomial term [26, 27], or by more elaborate constructions, including higher-order polynomial expansions, sinusoidal switching laws, and hysteretic operators [28, 29, 30]. This led to the discovery of a whole family of strange attractors within the same circuit frame.



(**a**) (**b**) (**c**)

Figure 1: Projection onto the xy- plane of the characteristic attractor of the Chua's systems described in Table 1; (a) Original Chua system, Eq. (1); (b) Cubic Chua system, Eq. (2); (c) Cubic-7 Chua system, Eq. (3).

Table 1: Different representations of the Chua system.

Chua System	Equations	
Original [6]	$\dot{x} = \sigma(y - x - f(x)),$ $\dot{y} = x - y + z,$ $\dot{z} = -\beta y,$ $f(x) = bx + \frac{1}{2}(a - b)(\lvert x + 1\rvert - \lvert x - 1\rvert).$	(1)
Cubic [26]	$\dot{x} = \sigma y - \sigma x^3 - \sigma c x,$ $\dot{y} = x - y + z,$ $\dot{z} = -\beta y.$	(2)
Cubic-7 [27]	$\dot{x} = \sigma \left[y + \frac{x - 2x^3}{7} \right],$ $\dot{y} = x - y + z,$ $\dot{z} = -\beta y.$	(3)

Table 2: Parameter values for the Chua system described in Table 1, and attractors displayed in Figure 1.

	Original	Cubic	Cubic-7
σ	10	10	9.5
β	14.87	16	100/7
a	-1.27	–	–
b	-0.68	–	–
c	–	-0.143	–

3 Problem Statement

The different systems and attractors described in Table 1 and Figure 1 have a similar shape, while the characteristic double-scroll attractor of the Chua circuit is preserved. In turn, the systems exhibit similar values in the classical metrics for chaotic systems based on the study of the time series: a positive Lyapunov exponent (close to 0.11), a Kaplan-Yorke dimension around 2.2, and a fractal dimension close to 2.1 [7, 8, 26, 27]. The values may vary between the systems if the parameters or resolution methods are changed but are similar, confirming that the different systems exhibit qualitatively similar chaotic behaviors.

However, a look at the axes in Figure 1 reveals considerable variations in the amplitudes of the different attractors. These changes are overlooked by the classical metrics used to study chaotic systems, but are clearly visible when the three attractors are plotted simultaneously. The questions arise: *Are the geometric changes exhibited by chaotic systems negligible in the sense that they can be safely disregarded once the chaotic nature of the attractor has been confirmed by classical metrics? Do classical metrics for studying chaotic dynamics—namely, Lyapunov exponents, Kaplan-Yorke and fractal dimensions—allow meaningful comparisons between systems that share a common topological structure but differ in their nonlinearities or parameters?* Inspired by previous results where the dynamical variations of the attractors are studied [21, 31], this work addresses these questions by studying the geometric variations in the convex hulls of two families of chaotic systems: three representations of the Chua attractor and a piecewise-linear jerk system under integer- and fractional-order dynamics. Under the premise of considering the geometry of the chaotic attractor instead of the temporal behavior, this work aims to visualize the dynamical changes between systems that share a common topological structure but are qualitatively distinguishable only through their geometry — changes that are generally omitted or invisible using classical metrics of chaotic systems, such as the Lyapunov exponent or the fractal dimension.

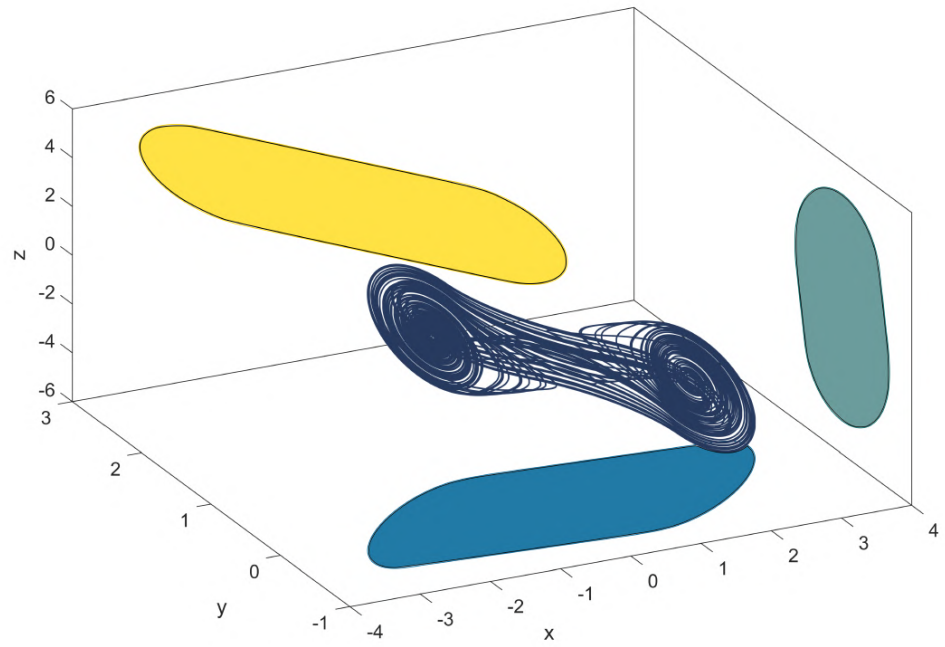


Figure 2: Visualization of the 2D projection surfaces of the Chua attractor obtained with the convex hull for Eq. (1). The areas calculated correspond to the filled regions.

4 Methodology and Results

This study focuses on analyzing geometric variations in chaotic attractors. Using convex hulls, we can enclose the smallest possible convex shape around a $2D$ projection of an attractor or approximate its volume in a $3D$ space. This approach provides a quantitative measure of changes in both the projected area and the total volume of the system.

Definition 4.1. *Let $\mathcal{S} = \{\mathbf{p}_1, \mathbf{p}_2, \ldots, \mathbf{p}_k\}$ be a finite set of k points in the Euclidean space $\mathbb{R}^n$. The convex hull of $\mathcal{S}$, denoted* $\mathrm{conv}(\mathcal{S})$*, is the smallest convex region that encloses all points of $\mathcal{S}$. For a set $\mathcal{S}$ in $\mathbb{R}^n$, its convex hull is given by*

$$\mathrm{conv}(\mathcal{S}) = \left\{ \sum_{i=1}^{k} \phi_i \, \mathbf{p}_i \;\middle|\; \mathbf{p}_i \in \mathcal{S},\ \phi_i \geq 0,\ \sum_{i=1}^{k} \phi_i = 1 \right\}, \tag{4}$$

where the coefficients ϕ_i, for $i = 1, 2, \ldots, k$, satisfy: (i) non-negativity, $\phi_i \geq 0$; and (ii) normalization, $\sum_{i=1}^{k} \phi_i = 1$. Together, these two conditions ensure that the linear convex combination in Eq. (4) *generates the smallest convex set that contains $\mathcal{S}$.*

The convex hull is calculated using integrated software functions that evaluate both the area (for $2D$ projections) and the volume (for $3D$ spaces) [32, 33]. The procedure for determining a convex hull is as follows and the results obtained are shown in (see Figure 2):

- Data structuring: The phase space points of the attractor are organized in a coordinate matrix.
- Hull construction: The convex hull algorithm is applied to extract the geometric properties of the enclosing shape.
- Area calculation: The projected area of the attractor is calculated for each 2D plane. The result is given in arbitrary square units.
- Volume estimation: The total volume occupied by the attractor in the state space is determined. The results are given in arbitrary cubic units.

Remark 4.1.1. *Accurate calculations of the convex hull require careful exclusion of transition states from oscillator dynamics. Including transient states can inflate the area and volume estimates and produce artificially larger values. This work performed all analyses after discarding transient periods to ensure reliable results.*

4.1 The Chua family

Using the attractors shown in Figure 1, the following values are calculated: (a) the Kaplan-Yorke dimension (D_{KY}), (b) the fractal dimension (D_f) by dimensional reduction using the Poincaré map, and (c) both the volume and the areas of the three projections of the attractor using the convex hull method. All results are shown in Table 3, where A_{jk} denotes the areas in the projection jk of the attractor, and V is for the total volume.

Table 3: Characterization of the Chua attractors described in Table 1 and shown in Figure 1.

	D_f	D_{KY}	$A_{xy}u^2$	$A_{xz}u^2$	$A_{yz}u^2$	Vu^3
Original	2.05	2.0603	6.2606	20.2192	10.0966	11.5953
Cubic-7	2.001	2.0345	0.4920	1.4207	0.7105	0.2354
Cubic	2.001	2.0350	0.1366	0.4166	0.1999	0.0515

Remark 4.1.2. Two clarifications are in order regarding the classical descriptors reported in Table 3. First, the fractal dimension D_f was estimated after reducing the system dimension via the Poincaré section, which yields $D_f^* = D_f - 1$ as described in [34]. The values reported in Table 3 already incorporate this summation factor, and are consistent with the Kaplan-Yorke dimension D_{KY} obtained directly from the Lyapunov spectrum. Second, and more importantly, for the aims of this work, it should be emphasized that the Poincaré section and the convex hull address complementary but distinct questions about the attractor. The Poincaré section is a *dimensional-reduction* tool: by intersecting the flow with a transversal hyperplane, it converts the continuous-time dynamics into a discrete map whose invariant set carries the fractal structure of the attractor. It therefore reveals *local, recurrence-based* information about how trajectories fold onto themselves. The convex hull, by contrast, is a *global, spatial-extent* descriptor: it encloses the attractor in the smallest convex region of the phase space, and quantifies how much of that space the attractor actually occupies. The two descriptors are neither redundant nor interchangeable. Two attractors can share essentially identical Poincaré-derived fractal dimensions, as is the case for the three Chua systems in Table 3, while differing by more than two orders of magnitude in convex-hull volume. In this sense, the convex hull provides information that is genuinely independent of, and complementary to, the Poincaré-based characterization.

4.2 Extension to a piecewise-linear fractional-order multi-scroll system

To assess the generality of the proposed methodology beyond the Chua family, we now apply it to a multi-scroll generator based on the jerk equation with a Saturated Non-Linear Function (SNLF), previously reported in [31]. This system was selected for four reasons: (i) it belongs to the jerk class, which is structurally different from the Chua family; (ii) its nonlinearity is a piecewise-linear (PWL); (iii) it admits both integer- and fractional-order integration, allowing us to probe whether the geometric metrics detect the effect of the fractional operator; and (iv) it generates a 9-scroll attractor whose global shape is known to depend on which state variable carries the fractional-order operator. The system is described by:

$$\begin{aligned} D^{q_x} x &= y, \\ D^{q_y} y &= z, \\ D^{q_z} z &= -\alpha[x + y + z - f(x)], \end{aligned} \tag{5}$$

where D^{q_i} denotes the Caputo fractional-order operator applied to state $i \in \{x, y, z\}$, $\alpha \in (0, 1)$ is the control parameter that places the system in the Unstable Dissipative System type I (UDS-I) region, and $f(x)$ is the SNLF that determines the equilibrium points around which the scrolls are organized. The explicit construction of $f(x)$, together with the electronic implementation of the fractance of order $q = 0.96$, is reported in [31] and is not reproduced here. The time series analyzed in this section were obtained from the electronic-circuit simulation of Eq. (5) in the Multisim development platform, following the implementation reported in [31]. Circuit-level simulation captures effects — such as operational amplifier saturation, component tolerances and the frequency response of the physical fractance — that are not present in a direct numerical integration of the fractional-order equations, and therefore provides an intermediate validation between pure numerical solutions and hardware experiments. We fix $\alpha = 0.45$ and analyze the five integration-order scenarios reported in [31]:

- $S_1 = [1, 1, 1]$ — integer-order (reference).
- $S_2 = [0.96, 0.96, 0.96]$ — commensurate fractional order.

- $S_3 = [1, 1, 0.96]$ — fractional order applied only to z.
- $S_4 = [1, 0.96, 1]$ — fractional order applied only to y.
- $S_5 = [0.96, 1, 1]$ — fractional order applied only to x.

Across all five scenarios, the system remains chaotic: the largest Lyapunov exponent retains the canonical signature of chaos, the fractal dimensions vary only within a narrow range. However, as summarized in Table 4, the convex-hull-based metrics reveal deformations of the attractor that the classical descriptors overlook.

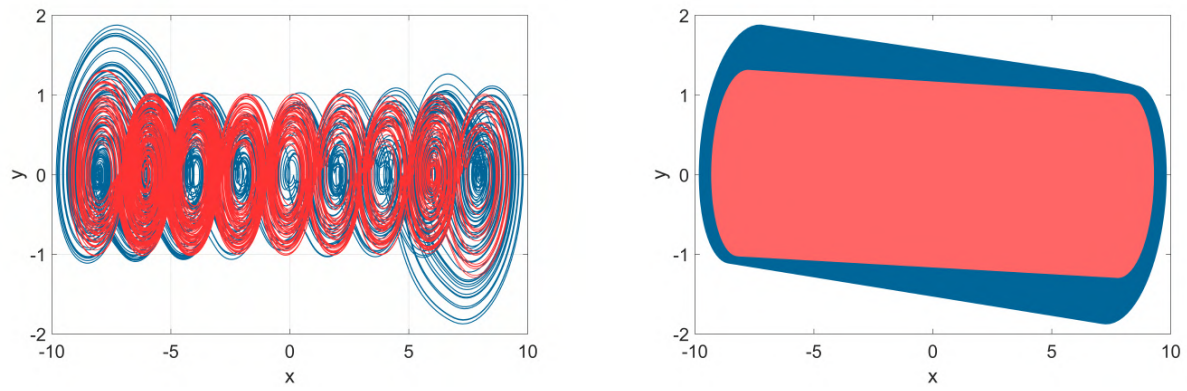


Figure 3: Convex-hull characterization of the SNLF-jerk attractor for scenarios S_1 (integer-order reference) and S_3 (fractional order applied to the z state variable). The two chaotic trajectories are shown in the left panel; the filled regions on the right panel correspond to the convex-hull projections onto the xy plane. Blue: S_1, with $A_{xy} = 57.39$, $A_{xz} = 34.79$, $A_{yz} = 7.01$, and total volume $V = 81.25$. Red: S_3, with $A_{xy} = 41.78$, $A_{xz} = 29.87$, $A_{yz} = 4.27$, and total volume $V = 55.91$. The comparison shows that applying the fractional-order operator to the z state variable alone induces a contraction of approximately 31% in the phase-space volume, while the classical dynamical descriptors remain essentially unchanged.

Table 4: Geometric characterization of the 9-scroll SNLF-jerk attractor described by Eq. (5) for scenarios S_1–S_5 at $\alpha = 0.45$. A_{jk} denotes the convex-hull area in the jk-projection of the attractor, and V is the total convex-hull volume in phase space. All values are given in arbitrary units of A^2 (areas) and V^3 (volume), following the voltage scale of the electronic implementation.

Scenario	$q^\top$	A_{xy}	A_{xz}	A_{yz}	V
S_1	$[1, 1, 1]$	57.39	34.79	7.01	81.25
S_2	$[0.96, 0.96, 0.96]$	51.24	32.71	5.21	67.53
S_3	$[1, 1, 0.96]$	41.78	29.87	4.27	55.91
S_4	$[1, 0.96, 1]$	59.49	30.79	5.80	73.81
S_5	$[0.96, 1, 1]$	51.75	32.85	6.36	66.17

Two observations follow. First, the choice of which state variable carries the fractional-order operator has a directional, non-monotonic effect on the geometry of the attractor: applying $q < 1$ to z (scenario S_3) contracts the attractor volume by 31% relative to the integer-order reference (S_1), whereas applying $q < 1$ to y (scenario S_4) contracts it by only 9%, and applying $q < 1$ to x (scenario S_5) contracts it by 19%. The commensurate case (S_2) yields an intermediate contraction of 17%. This directional effect is not resolved by the classical descriptors, the fractal dimensions across the five scenarios remain within a narrow range, and the Lyapunov exponent analysis retains the canonical chaotic signature, but is cleanly captured by the convex-hull descriptors.

Second, the geometric changes induced by the fractional operator are illustrated in Figure 3, which compares S_1 and S_3: the projection on the xy plane shrinks visibly, and Table 4 confirms that the same effect is present in the other two coordinate planes.

The result is significant in two additional respects. First, because $f(x)$ is a PWL switching function, the analysis confirms that the convex-hull methodology remains informative for attractors generated by non-smooth vector fields, and not only for the smooth (or partially smooth) variants of the Chua system considered in Section 4.1. Second, because scenarios S_2–S_5 involve fractional-order dynamics, the analysis shows that the methodology captures geometric deformations induced by the memory of the fractional operator, a class of variations that is otherwise difficult to quantify using time-series-based descriptors alone. A broader validation of the geometric perspective across additional attractor families, including the Rössler oscillator, its PWL variant, and additional multi-scroll generators, analyzed under a topological refinement of the convex hull based on the α-shape, is reported in [21, 35].

5 Discussion and Conclusions

Two families of chaotic systems have been examined through the convex-hull methodology in Sections 4.1 and 4.2: three variants of the Chua oscillator sharing the double-scroll topology, and five integration-order scenarios of a piecewise-linear jerk system generating a nine-scroll attractor. In every case, the classical descriptors — Lyapunov spectrum, Kaplan-Yorke and fractal dimensions — confirmed that the systems remain qualitatively equivalent in their chaotic behavior, while the convex-hull descriptors revealed differences of one to two orders of magnitude in projected areas and total volume. This consistent gap between the two families of descriptors motivates the following formal statement.

Proposition 5.1 (Geometric independence from classical chaotic characterization)**.** *Let $\mathcal{S}_1$ and $\mathcal{S}_2$ be two dissipative continuous-time dynamical systems in $\mathbb{R}^n$, each admitting a bounded strange attractor $\mathcal{A}_i$, and assume that both systems satisfy:*

(a) Topological equivalence: *$\mathcal{A}_1$ and $\mathcal{A}_2$ share the same qualitative structure (e.g., double-scroll, spiral, or multi-scroll of the same order).*

(b) ε-similarity in classical chaos metrics: *there exists $\varepsilon > 0$ such that*

$$|\lambda_1^{(1)} - \lambda_1^{(2)}| < \varepsilon, \qquad |D_{KY}^{(1)} - D_{KY}^{(2)}| < \varepsilon, \qquad |D_f^{(1)} - D_f^{(2)}| < \varepsilon, \tag{6}$$

where $\lambda_1^{(i)}$, $D_{KY}^{(i)}$, and $D_f^{(i)}$ denote the largest Lyapunov exponent, the Kaplan-Yorke dimension, and the fractal dimension of $\mathcal{A}_i$.

Then the geometric descriptors $V\big(\mathrm{conv}(\mathcal{A}_i)\big)$ and $A_{jk}\big(\mathrm{conv}(\pi_{jk}\mathcal{A}_i)\big)$, where π_{jk} denotes the projection onto the x_j–x_k plane, need not satisfy any analogous ε-bound. In particular, the ratio

$$\rho := \frac{V\big(\mathrm{conv}(\mathcal{A}_1)\big)}{V\big(\mathrm{conv}(\mathcal{A}_2)\big)} \tag{7}$$

can differ from unity by arbitrary orders of magnitude.

Justification. The claim admits a direct argument based on the different invariance properties of the two families of descriptors. The classical metrics — Lyapunov exponents, Kaplan-Yorke and fractal dimensions — are invariant under smooth invertible changes of coordinates, and depend on the local expansion and contraction rates of the flow rather than on the absolute amplitudes of the state variables. The convex-hull descriptors, in contrast, are amplitude-dependent by construction: the linear rescaling $x \mapsto \sigma x$, with $\sigma > 0$, leaves λ_i, D_{KY} and D_f unchanged while scaling every projected area by σ^2 and the total volume by σ^3. Hence, two systems whose vector fields differ only in an effective amplitude scale exhibit the property claimed above, and the ratio ρ can be made arbitrarily large or small.

Explicit verifications are provided by Table 3 for the Chua family, where the original and cubic versions share D_{KY} and D_f to within $\varepsilon \approx 0.03$ while exhibiting a volume ratio $\rho \approx 225$, and by Table 4 for the SNLF-jerk family, where scenarios S_1–S_5 share the same qualitative dynamics but their convex-hull volumes span a range of $\rho \approx 1.45$, with the smallest attractor (S_3, fractional order applied to z) contracting by roughly 31% in volume relative to the integer-order reference (S_1). The comparatively modest value of ρ in this family reflects a structural difference with respect to the Chua case: the SNLF-jerk scenarios share a common electronic implementation whose amplitude scale is fixed by the plateaus of the saturated non-linear function, so the geometric variability is intrinsically bounded. Even under this constraint, the fractional-order operator induces a volumetric change that is not detected by the classical descriptors. Further evidence covering the Rössler system, its PWL variant, and additional multi-scroll systems is reported in [21, 35]. □

Proposition 5.1 makes explicit that the geometric characterization introduced in this work is not a proxy for the dynamical characterization: it captures a distinct and independent property of the attractor. The convex-hull descriptors are therefore best interpreted as *complementary* rather than *alternative* metrics — they discriminate between chaotic systems precisely in the regime where classical descriptors are inconclusive. This directly answers the two questions posed in the Problem Statement of this work. *Are the geometric changes exhibited by chaotic systems negligible once the chaotic nature has been confirmed?* They are not: the Chua family alone exhibits a volume variation of more than two orders of magnitude while its Kaplan-Yorke and fractal dimensions vary by less than 0.03, and the SNLF-jerk family reproduces the same pattern under fractional-order variations. *Do classical metrics allow meaningful comparisons between systems that share a common topological structure but differ in their nonlinearities or parameters?* They allow us to

confirm that the systems are chaotic and topologically equivalent, but they do not resolve the geometric differences that distinguish one implementation from another.

The complementary use of the convex hull as a fundamental metric to study chaotic systems is proposed to allow a quantitative comparison of different systems. The significant differences observed from the geometry of the systems can be decisive in the choice of one model over another for a particular application, e.g., in the implementation of mechanical systems or in the development of integrated circuits, where amplitude limitations are decisive factors [36, 37]. The addition of studies of chaotic systems from the geometric perspective, as we have done, provides an opportunity to establish criteria for choosing one chaotic system over another when the chaotic behavior is a constant.

Acknowledgments

J.L.E.M. thanks J.L.E.L. for all his support, his teachings, and his enriching conversations over all these years. J.L.E.M. thanks SECIHTI for support (CVU: 706850). This work was supported by the Secretaría de Ciencia, Humanidades, Tecnología e Innovación (SECIHTI), Mexico, through the Ciencia Básica y de Frontera 2026 project CBF-2026-2581, "Inteligencia artificial como herramienta para el desarrollo de sistemas complejos: generación y validación de nuevos sistemas con comportamiento caótico con aplicaciones en matemáticas, física, ingeniería y comunicaciones seguras." Proyecto apoyado por la Secihti en el año 2026.

Conflicts of interest

The authors declare that they have no conflicts of interest with respect to this article.

References

[1] H.G. Schuster and W. Just. *Deterministic chaos: an introduction*. Vol. 2. Wiley Online Library, 1988.

[2] G. Ambika. "Ed Lorenz: father of the 'butterfly effect'". In: *Resonance* 20.3 (2015), pp. 198–205.

[3] J.L. Echenausía-Monroy, J.R. Cuesta-García, and J. Pena Ramirez. "The wonder world of complex systems". In: *Chaos Theory and Applications* 4.4 (2022), pp. 267–273.

[4] R.N. Madan. *Chua's circuit: a paradigm for chaos*. Vol. 1. World Scientific, 1993.

[5] L. Chua and R. Ying. "Canonical piecewise-linear analysis". In: *IEEE Transactions on Circuits and Systems* 30.3 (1983), pp. 125–140.

[6] T. Matsumoto, L.O. Chua, and K. Kobayashi. "Hyper chaos: laboratory experiment and numerical confirmation". In: *IEEE Transactions on Circuits and Systems* 33.11 (1986), pp. 1143–1147.

[7] L.O. Chua. *The Genesis of Chua's Circuit*. Memorandum (University of California, Berkeley, Electronics Research Laboratory). Electronics Research Laboratory, College of Engineering, University of California, 1992. URL: https://books.google.co.in/books?id=rs5fGwAACAAJ.

[8] L.O. Chua. "Chua's circuit 10 years later". In: *International Journal of Circuit Theory and Applications* 22.4 (1994), pp. 279–305.

[9] T. Matsumoto. "A chaotic attractor from Chua's circuit". In: *IEEE transactions on circuits and systems* 31.12 (2003), pp. 1055–1058.

[10] A. Wolf et al. "Determining Lyapunov exponents from a time series". In: *Physica D: nonlinear phenomena* 16.3 (1985), pp. 285–317.

[11] A. Politi. "Lyapunov exponent". In: *Scholarpedia* 8.3 (2013), p. 2722.

[12] J.D. Farmer. "Dimension, fractal measures, and chaotic dynamics". In: *Evolution of Order and Chaos: in Physics, Chemistry, and Biology Proceedings of the International Symposium on Synergetics at Schloß Elmau, Bavaria, April 26–May 1, 1982*. Springer. 1982, pp. 228–246.

[13] F. Freistetter. "Fractal dimensions as chaos indicators". In: *Celestial Mechanics and Dynamical Astronomy* 78 (2000), pp. 211–225.

[14] J.L. Kaplan and J.A. Yorke. "Preturbulence: a regime observed in a fluid flow model of Lorenz". In: *Communications in Mathematical Physics* 67 (1979), pp. 93–108.

[15] J.D. Farmer, E. Ott, and J.A. Yorke. "The dimension of chaotic attractors". In: *Physica D: Nonlinear Phenomena* 7.1-3 (1983), pp. 153–180.

[16] H. Poincaré. "Sur le problème des trois corps et les équations de la dynamique". In: *Acta mathematica* 13.1 (1890), A3–A270.

[17] J. Barrow-Green. *Poincaré and the three body problem*. Vol. 11. American Mathematical Soc., 1997.

[18] P. Grassberger. "Grassberger-Procaccia algorithm". In: *Scholarpedia* 2.5 (2007), p. 3043.

[19] E.N. Lorenz. "Deterministic nonperiodic flow". In: *Universality in Chaos, 2nd edition*. Routledge, 2017, pp. 367–378.

[20] C.M.M. Casado. "Edward Lorenz (1917-2008): ¿Padre de la teoría del caos?." In: *Revista española de física* 22.3 (2011).

[21] J.L. Echenausía-Monroy et al. "Beyond chaos in fractional-order systems: Keen insight in the dynamic effects". In: *Fractal and Fractional* 9.1 (2024), p. 22.

[22] L.O. Chua et al. *Methods of Qualitative Theory in Nonlinear Dynamics (Part II)*. Vol. 5. World Scientific, 2001.

[23] M.S. Baptista, I.L Caldas, et al. "Shilnikov homoclinic orbit bifurcations in the Chua's circuit". In: *Chaos: An Interdisciplinary Journal of Nonlinear Science* 16.4 (2006).

[24] E. Lorenz. "The butterfly effect". In: *The chaos avant-garde: Memories of the early days of chaos theory*. World Scientific, 2000, pp. 91–94.

[25] O.E. Rössler. "The chaotic hierarchy". In: *Zeitschrift für Naturforschung A* 38.7 (1983), pp. 788–801.

[26] C. Sarasola et al. "Energy balance in feedback synchronization of chaotic systems". In: *Physical Review E* 69.1 (2004), p. 011606.

[27] F. Ozkaynak. "A novel random number generator based on fractional order chaotic Chua system". In: *Elektronika ir Elektrotechnika* 26.1 (2020), pp. 52–57.

[28] E. Campos-Cantón et al. "A multivibrator circuit based on chaos generation". In: *International Journal of Bifurcation and Chaos* 22.01 (2012), p. 1250011.

[29] C.H. Lamarque, O. Janin, and J. Awrejcewicz. "Chua systems with discontinuities". In: *International Journal of Bifurcation and Chaos* 9.04 (1999), pp. 591–616.

[30] N. Tsafack and J. Kengne. "Complex dynamics of the Chua's circuit system with adjustable symmetry and nonlinearity: Multistability and simple circuit realization". In: *World J. Appl. Phys* 4.2 (2019), p. 24.

[31] J.L. Echenausía-Monroy et al. "A physical interpretation of fractional-order-derivatives in a jerk system: Electronic approach". In: *Communications in Nonlinear Science and Numerical Simulation* 90 (2020), p. 105413.

[32] P.S. Theme. *Spatial algorithms and data structures (scipy.spatial)*. Accessed on May 01, 2025. 2025. URL: `https://docs.scipy.org/doc/scipy/reference/generated/scipy.spatial.ConvexHull.html`.

[33] I. The MathWorks. *convexHull*. Accessed on May 01, 2025. 2025. URL: `https://la.mathworks.com/help/matlab/ref/convhull.html`.

[34] G.L. Baker and J.P. Gollub. *Chaotic dynamics: an introduction*. Cambridge university press, 1996.

[35] J.L. Echenausía-Monroy et al. "The shape of chaos: A geometric perspective on characterizing chaos". In: *Mathematics* 14.1 (2025), p. 15.

[36] R. Trejo-Guerra et al. "Integrated circuit generating 3-and 5-scroll attractors". In: *Communications in Nonlinear Science and Numerical Simulation* 17.11 (2012), pp. 4328–4335.

[37] R. Trejo-Guerra et al. "A survey on the integrated design of chaotic oscillators". In: *Applied Mathematics and Computation* 219.10 (2013), pp. 5113–5122.

Journal of Dynamical Systems and Complexity (2026) vol.1(3): 11-22
eISSN: 3122-4326, DOI: 10.66131/JDSC12202611-23

Simple Gaussian Filter can Protect Images of Noise Injection in a Classification Task with Deep Neural Networks

Luis Gerardo de la Fraga, Christian Ruiz Hernández*

Cinvestav, Computer Science Department, Av. IPN 07460 Mexico City, Mexico

Abstract

We study the classification of a set of images under additive Gaussian noise and additive colored Pink noise. We observe that the very simple denoising Gaussian filter obtain the best results for a classification problem using a Deep Convolutional Network. We were able to generate an attack of noise injection to change the class of two images, and the correct class can be obtained applying also the very simple Gaussian filter.

Keywords— Convolutional Neural Networks, Deep Neural Networks, Noise Attack, Denoising

1 Introduction

When discussing Neural Networks or Convolutional Neural Networks (CNNs), it is often assumed that "all networks can tolerate some degree of noise," yet the specific amount or type of tolerable noise is rarely quantified. In this work, we explore this topic within the context of CNNs applied to classification problems. Specifically, we propose adding additive Gaussian noise to images to establish a reference point. We utilized a pretrained EfficientNet model, originally trained to classify eight shapes as described in the thesis [1].

The main motivation for researching this area is the cost of maintaining large convolutional neural network architectures. The big models for classification or detection use a minimal input size of 224 x 224. The industry tries to save computational power by using reduced architectures. We can see a clear reduction in the number of layers, number of neurons, or the use of small input sizes, resizing the input sizes to adapt in any situation. The use of limited neural networks for mass use in different fields is the reason why different weaknesses were found in convolutional neural networks on classification problems.

Currently, numerous CNN architectures exist, predominantly used for classification and detection. These models are widely deployed in critical applications, such as autonomous driving systems and medical diagnostics (e.g., detecting ailments via X-rays or magnetic resonance imaging). Given these high-stakes contexts, it is important to know their real weaknesses. One such vulnerability is noise tolerance, which raises the question of how effectively image noise can be mitigated using various preprocessing techniques.

It is important to note that our experiments employed a reduced version of the pretrained EfficientNet model, rather than the original complete architecture. This model was reduced in both image input size and the number of filters [1].

It is fundamental to identify the noise and the level of noise to create effective methods to increase the accuracy in models with different environmental noise. We work to find the most efficient method to mitigate the negative effect of noise over the images.

Here is the importance of this work. We want to find the levels of noise that the convolutional neural networks can support. Because if we want to make a solution of misclassification, we need to start identifying the noise. After that, we test the most simple methods to fix them, showing that it is not necessary to use more complex solutions like Generative Adversarial Networks or Autoencoders.

*Corresponding author: christian.ruiz@cinvestav.mx
Received: December 20, 2025, **Published:** October 30, 2026
Editor: J.M. Muñoz-Pacheco

This work was inspired by the article [2], they basically use a targeted noise using differential evolution (DE) to find the best noise to change the class where an image belongs. They coded the solution with two values (x, y) for the position of the pixel, and three values RGB to specify the color for each infected pixel, then each solution given by the DE heuristic contains $5n$ values, for n pixels of noise. This is a very important point because this implementation increases the complexity too fast if the number of pixels is high. We tested over models with an input size 64×64 while the article [2] uses an input models 32×32. In our test, we did not find solutions from 1 to 30 pixel attacks over images of 64×64 pixels, and this noise was not enough to change the class. We were able to attack images of size 16×16 pixels.

In the article [2], authors mention that on datasets like ImageNet where the images size is 227×227, then they resize the images to the input size of the convolutional neural network architecture, using the nearest pixel algorithm to resize the images. This is the simplest algorithm to assign the pixel value in an image resize operation. This idea was an interesting method to attack any model as a black box, like in a real scenario. Then the community continues investigating the attack. The article [3] made a comparison between the performance on methods the one-pixel attack, and brute force, using differential evolution, and genetic algorithms as search methods. They observe that the differential evolution is not the most efficient way and open the problem to use other search methods.

In the same way, we use Gaussian noise to contaminate the image models because it is another of the most commonly studied noises. For example, in the article [4], a CNN with Gaussian noise over chest X-ray images was trained as a binary classifier. They discover that this kind of trained model can increase the specificity while the general accuracy is maintained. Then, with this method to train with noised samples, a CNN is powerful, but they did not try to clean the samples during the test.

Another recent example is in the article [5], they use an anisotropic Gaussian filter to train a CNN that helps to denoise images that contain different levels of noise. Their work demonstrates that it is possible to use a preprocessed filter on combinations with CNN to learn to denoise images and reduce the weakness of the CNN.

There are many ways to solve this problem on different publications. In the article [6], the authors mention the advantages to use genetic programming to solve classification problems, they showed a good result using a tree with different known descriptors like Gabor filter, Sobel, HOG and poolings (average, minimum and maximum). They modeled the classification problem like combinatorial optimization problem. Using a combination of these descriptors and another simple classifiers well known like random forest, Support Vector Machine and logistic regression. They fixed the classifiers in the architectures and evolve the combinations of descriptors.

Another study [7] suggests that feature extraction can be divided into regions of interest (ROIs), not that similar features frequently appear in specific areas within the same dataset. The authors utilize two geometric configurations for these regions: rectangles and squares. For rectangular regions, it is necessary to define the position as well as the height and width dimensions. In contrast, for square regions, only the position and a single side length are required to determine the dimensions. They modeled the problem of searching for the optimal combination of descriptors as a classification task, similar to the approach in [6]. In this work, they employ k-means as the sole classifier to evaluate and evolve various permutations of coordinates and sizes. The objective is twofold: to identify the best descriptor combinations and to discover the most common regions that yield superior features using both geometric shapes.

In the book [8], chapter 8, the author mentions that it is possible to use genetic programming as a feature extractor in classification problems by searching in parallel the regions of the most common places over the images to get the maximum number of features.

One objective on this work is the exploration of the most simple black box attack named one pixel attack [2]. Mention that it is possible to find some noised images modeling the problem as an optimization problem. Where the CNN is a black box function, and the problem is maximize the confidence of the different label class than the original. The authors use differential evolution to solve the optimization problem.

Another way to see the misclassify problem is like a white box or gray box. Where we know partial information about the CNN, or we can have full access to CNN model. This is the case explored in the article [9], the algorithm attack the images adding noise over all the image starting with a small perturbation to big perturbation, and stops the search when the image classification changes. Using information about the gradients of the models as a compass. The two differences are the way to search the noise and how it is applied over all the pixels.

This article is organized as follows. In Section 2, it is explained how the Gaussian noise and the one pixel attack noise are used. In Section 3, the results of our experiments are shown. In Section 4, some discussions about this work are given. Finally, in Section 5, some conclusions of this work are described.

2 Method

2.1 Gaussian additive noise

The Gaussian noise is the most common and well-studied noise. This kind of noise is very simple to generate and add to images because we only need to generate pseudorandom numbers with a normal distribution and only use two parameters, the mean and the standard deviation, to increase and decrease the level of noise.

For experiments, the pixel values of the grayscale input image are normalized to values from 0 to 1, and we propose 16 combinations of Gaussian noise with four means [0.2, 0.4, 0.6, 0.8] and four standard deviations [0.06, 0.12, 0.18, 0.24].

We create an image with these generated numbers and add it to the original image, using the clip function to limit the range of values to [0, 1]. The clip function sets values smaller than 0 to 0 and values greater than 1 to 1. In Figure 1, we visualize this process.

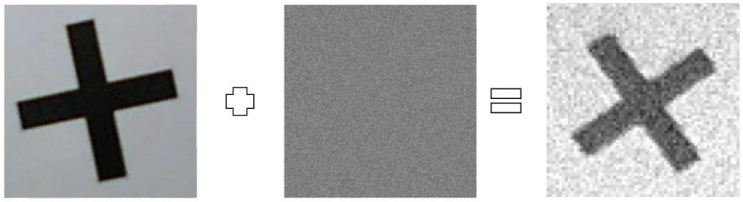


Figure 1: Illustration about how is added the Gaussian noise.

The main idea of this attack is to get a sample from the dataset and test by adding sixteen noise combinations. After that, we identify the noise combination that changes the classification label of the noisy image.

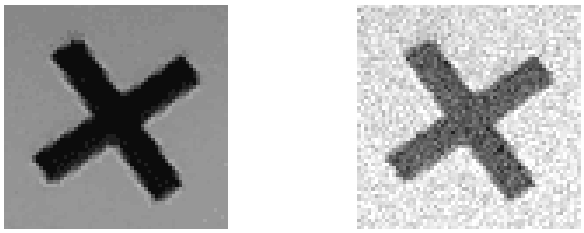


Figure 2: On the left cross figure clean and on the right noisy image with Gaussian noise using 0.2 as mean and 0.06 as standard deviation.

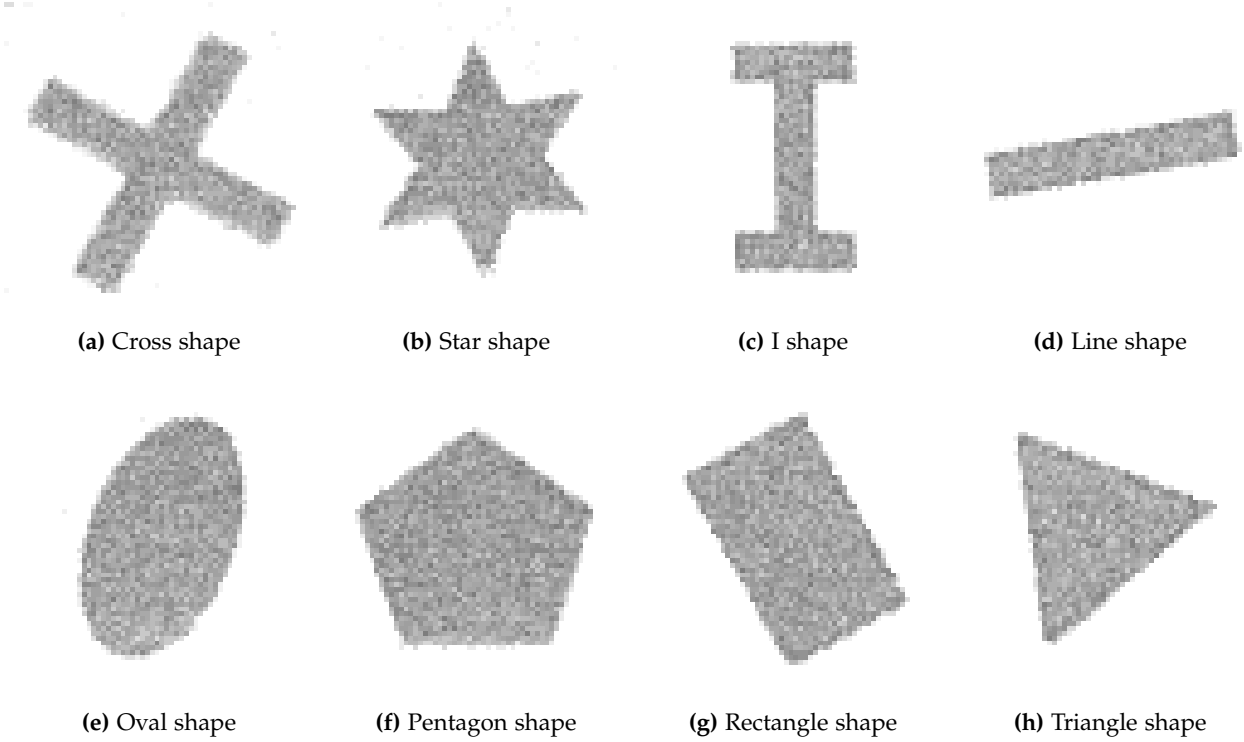
$$\mathbf{A}+\mathbf{B}=\begin{bmatrix} a_{11} & a_{12} & \cdots & a_{1n} \\ a_{21} & a_{22} & \cdots & a_{2n} \\ \vdots & \vdots & \ddots & \vdots \\ a_{m1} & a_{m2} & \cdots & a_{mn} \end{bmatrix}+\begin{bmatrix} b_{11} & b_{12} & \cdots & b_{1n} \\ b_{21} & b_{22} & \cdots & b_{2n} \\ \vdots & \vdots & \ddots & \vdots \\ b_{m1} & b_{m2} & \cdots & b_{mn} \end{bmatrix}=\begin{bmatrix} a_{11}+b_{11} & a_{12}+b_{12} & \cdots & a_{1n}+b_{1n} \\ a_{21}+b_{21} & a_{22}+b_{22} & \cdots & a_{2n}+b_{2n} \\ \vdots & \vdots & \ddots & \vdots \\ a_{m1}+b_{m1} & a_{m2}+b_{m2} & \cdots & a_{mn}+b_{mn} \end{bmatrix} \tag{1}$$

Equation (1) shows the operation to add the original image to the noise. The matrix A represents the original image, and the matrix B represents the noise matrix. Each element of matrix A is added to the corresponding element of matrix B at the same position to generate the output matrix, which is the noisy image.

With these different types of noise, we test the pretrained EfficientNet model and obtain the results shown in Table 1. We evaluate the combination with the level of noise with mean 0.6 and standard deviation 0.06 with an accuracy around 0.25; example images with this noise are shown in Figure 3.

Table 1: EfficientNet All noises

Different levels of noise		
Mean μ	Standard deviation σ	Accuracy
0.2	0.06	1.000
0.2	0.12	0.864
0.2	0.18	0.160
0.2	0.24	0.125
0.4	0.06	1.000
0.4	0.12	0.160
0.4	0.18	0.133
0.4	0.24	0.131
0.6	**0.06**	**0.254**



(a) Cross shape **(b)** Star shape **(c)** I shape **(d)** Line shape

(e) Oval shape **(f)** Pentagon shape **(g)** Rectangle shape **(h)** Triangle shape

Figure 3: Example of shapes with Gaussian noise (mean 0.6, std. dev. 0.06).

2.2 One pixel attack

The main idea of this attack is to assume that there exists a trained and unknown convolutional neural network (CNN) architecture, used as a black box, to classify images. The original authors modeled this problem as an optimization problem where the classification error is the target value to maximize. We then evaluate the CNN output as an indicator. We use only the case of a non-targeted attack, then in this variant is only necessary to minimize the confidence of the original class.

As we mentioned in the introduction, we test a one-pixel attack on our pretrained EfficientNet model. First, we test with original images of size 64×64 for the one-pixel non-targeted attack, which means we search for the best solution where the classification changes without searching for a specific target class. We adapted the attack to our pretrained EfficientNet model because it uses only one channel; therefore, we can reduce the search space by encoding the solution as [x,y,intensity] instead of [x,y,R,G,B].

With the original input size, we did not find a solution with this technique. Then, we resized the input image from 64×64 to 16×16 using the same nearest-neighbor filter mentioned in the article [2]. We tested with 30 and 40 pixels on rescaled images, and we found a satisfactory solution where the original pentagon shape was misclassified as a cross.

The optimization problem is described in (2). The classification function is f. The element $\mathbf{x}$ is the input image and the e function describes the noise process. The e function returns a vector with the same size of the input image. There is a constraint where the norm L_0 of e needs to be below or equals d, where d is the number of pixels attacked. That means the vector will contain 0 values where the values of pixels were not attacked to keep the same size of the image. Then the noise is a simple additive process. The scheme attack sees the f function as a black box and the e function is defined by the evolution process. It is assumed the classifier always return a vector with the confidences for each class. The objective is t maximize the class target confidence value.

$$\begin{aligned} \max_{e(\mathbf{x})^*} \quad & f_{adv}(\mathbf{x} + e(\mathbf{x})) \\ \text{subject to} \quad & \|e(\mathbf{x})\|_0 \leq d, \end{aligned} \tag{2}$$

The flowchart describing how the one-pixel attack works is shown in Fig. 4. The attack requires a method to encode each attacked pixel in a linear fashion. For each pixel, we must specify the x and y coordinates and the intensity value. Consequently, for grayscale images, it is necessary to optimize three values per pixel, whereas for RGB images, it is necessary to optimize five values per pixel.

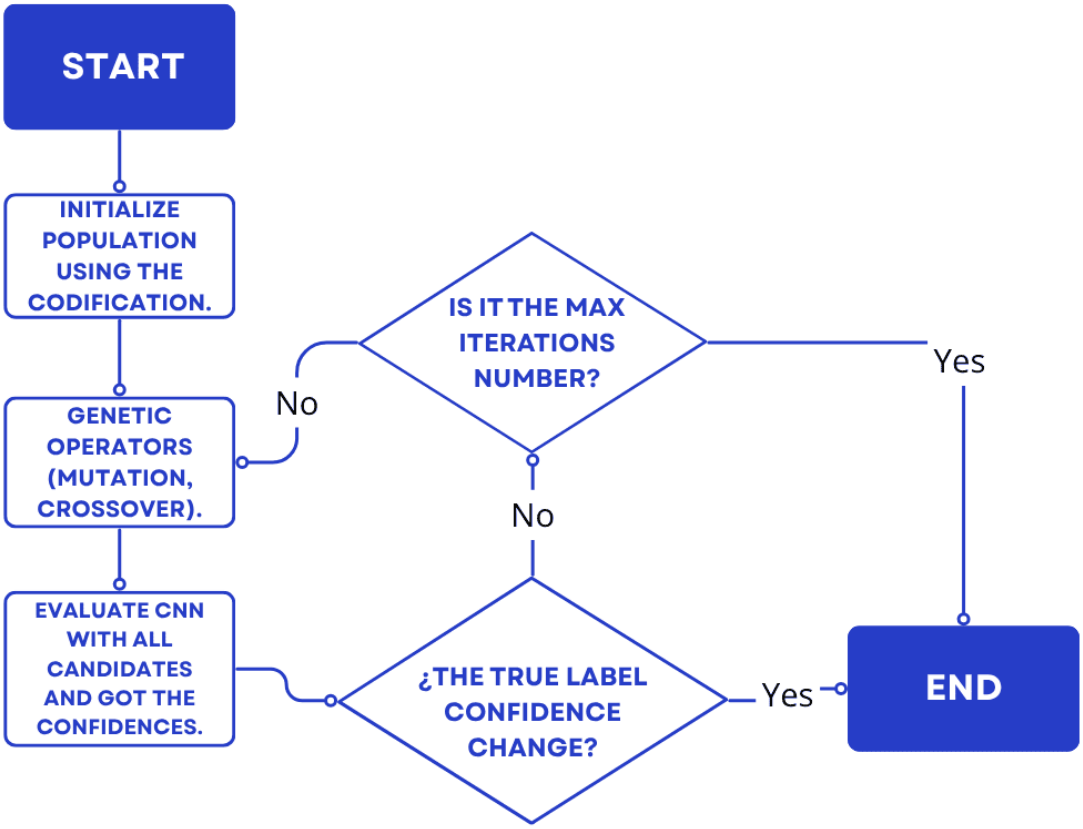


Figure 4: One pixel attack flowchart

3 Results

3.1 Testing additive Gaussian noise

We trained the EfficientNet model with 60,000 noisy images during 100 epochs with a batch size of 128. We then test the model on 480 random noisy images (60 per class) to validate it. Then we obtain the results shown in Tab. 2.

Table 2: EfficientNet retrained with noisy images with μ=0.6 and σ=0.06

Different levels of noise		
Mean μ	Standard deviation σ	Accuracy
0.2	0.06	0.795
0.2	0.12	0.691
0.2	0.18	0.370
0.2	0.24	0.150
0.4	0.06	0.968
0.4	0.12	0.870
0.4	0.18	0.800
0.4	0.24	0.325
0.6	**0.06**	**0.985**
0.6	0.12	0.547
0.6	0.18	0.337
0.6	0.24	0.314

The results indicate that the model learns about the noise very well but with less noise, with mean value less than 0.6, the model did not keep the accuracy.

3.2 Retraining classification model with Gaussian filter

This method consists of training the EfficientNet model with the same dataset of 60,000 noisy images, but using the Gaussian filter to denoise the image. In this case, we retrained that model to learn how to correctly classify images with that filter applied over noisy images. We obtained the results shown in Table 3, we can see that obtained accuracy is 1.0.

Table 3: Efficientnet using Gaussian filter to denoise summary results

Different levels of noise		
Mean μ	Standard deviation σ	Accuracy
0.2	0.06	1.000
0.2	0.12	1.000
0.2	0.18	1.000
0.2	0.24	0.950
0.6	**0.06**	**1.000**
0.6	0.12	0.981
0.6	0.18	0.502
0.6	0.24	0.268

3.3 Pink noise

We tested with another kind of noise named pink noise. This noise is one of the noises called colored noise. This kind of noise basically takes a random noise, applies the Fourier transform to change over the frequency domain, and applies a filter using Equation (3). Where f is the frequency. Different color noise changes the exponent, sometimes named alpha or beta in the literature, but in this case we try with pink noise, and this value is fixed in 1. After we calculate Equation (3) multiply with the noise values to generate the filtered. Finally, it is necessary to apply the inverse Fourier transform to obtain the noise that will be added over the input signal.

$$S(f) \propto \frac{1}{f^{\alpha}}, \tag{3}$$

in Equation (3), S is the power spectral density. If it is considered a 2D signal, 't' becomes to the x and y coordinates. Then, when the fast Fourier transform is applied, it will work with the magnitude of the frequency.

Algorithm 1 Pink Noise

Require: A is a matrix of $n \times n$ size with random values and a uniform distribution.
Ensure: Pink noise on pixel values context, in range [0, 1]

$F \leftarrow \text{fftshift}(\text{fft2}(A))$ ▷ Apply fast Fourier transform 2D and move the zero frequency to the center
for each pixel (i, j) with the same size $n \times n$ **do**
  $f \leftarrow \sqrt{u_i^2 + v_j^2}$ ▷ Calculate the frequency
  $G(i, j) \leftarrow \frac{1}{\max(f,1)}$ ▷ Calculate the filter
end for
$F_{\text{filtered}} \leftarrow F \odot G$ ▷ Multiply the values of the filter with the original signal to obtain the filtered signal on the frequency domain.
$I_{\text{imaginary}} \leftarrow \text{ifft2}(\text{ifftshift}(F_{\text{filtered}}))$
$I_{\text{real}} \leftarrow \text{Real}(I_{\text{imaginary}})$ ▷ Only uses the real component
$I_{\text{pink}} \leftarrow \frac{I_{\text{real}} - \min(I_{\text{real}})}{\max(I_{\text{real}}) - \min(I_{\text{real}})}$ ▷ Apply a normalization a $[0, 1]$
return I_{pink}

This implementation was based on GitHub https://github.com/felixpatzelt/colorednoise and fallow the instructions written by Paul Bourke on his blog https://paulbourke.net/fractals/noise/ to adapt in two dimensions the pink noise. The implementation in Algorithm 1, uses the *numpy* library and its functions FFT2 and IFFT to calculate the fast Fourier transform and its inverse. It is visible in Algorithm 1, that the pink noise is a filter applied over the random noise in the frequency domain. Then pink noise is added over the images to obtain images as shown in Figure 5.

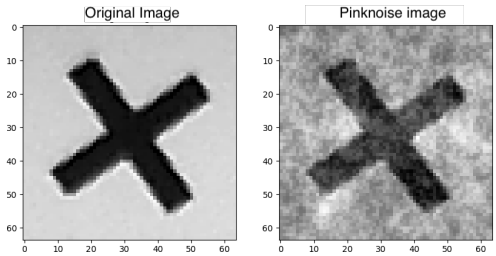


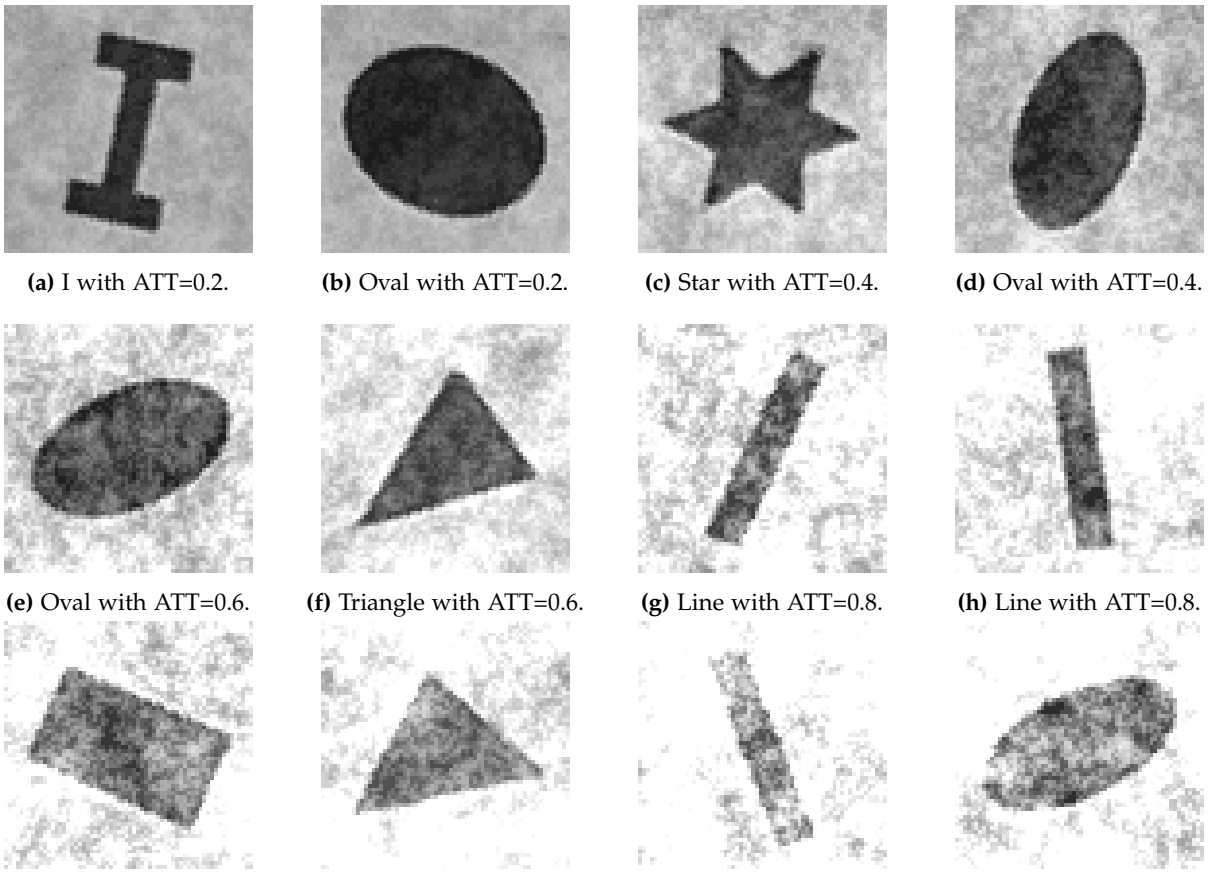
Figure 5: Sample Pink Noise

For using similar parameters, we test with 5 different attenuation levels of noise, [0.2, 0.4, 0.6, 0.8, 1.0]. Where each number of attenuation in Table 4 represents the percentage of intensity for each pixel that will be added. For example, if the pixel intensity of the pink noise is 0.4 and the attenuation factor 0.4, then we only added 0.16 as intensity over the original image.

Table 4: Results using pink noise, tested over EfficientNet retrained and preprocessed with Gaussian filter.

Different levels of noise	
Attenuation	Accuracy
0.2	1.0
0.4	1.0
0.6	**0.9**
0.8	0.5
1.0	0.2

If you consider the Gaussian noise generated values near the mean, then it is equivalent to attenuate the signal. Extrapolating this concept to pink noise we consider test with the same mean as attenuate noise. With this method is possible to see a consistent behavior between the Gaussian noise and the pink noise where using the same attenuation of 0.6 as it is shown on Table 4, we obtain better with the same attenuation values employing our model retrained with the Gaussian noise and Gaussian filter as a preprocessing. It is interesting to observe that, despite not being trained specifically on pink noise at the same noise levels, the model exhibited a similar behavior when using this re-training and pre-processing approach with a Gaussian filter.



(a) I with ATT=0.2. **(b)** Oval with ATT=0.2. **(c)** Star with ATT=0.4. **(d)** Oval with ATT=0.4.

(e) Oval with ATT=0.6. **(f)** Triangle with ATT=0.6. **(g)** Line with ATT=0.8. **(h)** Line with ATT=0.8.

(i) Rectangle with ATT=0.8. **(j)** Triangle with ATT=0.4. **(k)** Line with ATT=1.0. **(l)** Oval with ATT=1.0.

Figure 6: Example of shapes with pink noise with different attenuation levels.

In Figure 6 is shown how the pink noise in two dimensions generate noise similar to clouds. In high levels the distortion is worst than the Gaussian noise because the pink noise generate biggest regions with similar values. This similar regions deform the original figure.

3.4 Testing one pixel attack

We tested with different population sizes: the initial population size was 15 (the default for the differential evolution heuristic in the SciPy library). Subsequently, we increased the population size to 100, and finally to 1000. We performed these increments to investigate whether the number of function evaluations was a bottleneck affecting the trade-off between solution quality and execution time. All tests were conducted on a server with 20 cores. We run the test on a server with 20 cores and 20 threads, then we did these evaluations using all the power with 40 threads.

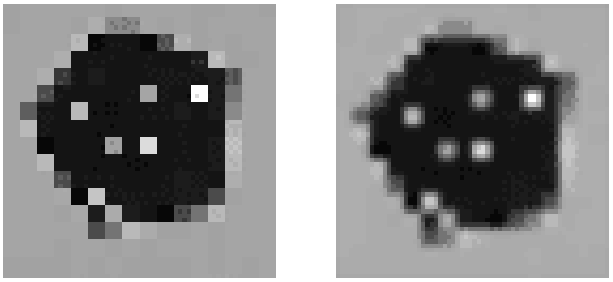


Figure 7: On the right is the noisy image solution of 30 Pixel Attack and on left pentagon shape with Gaussian filter .

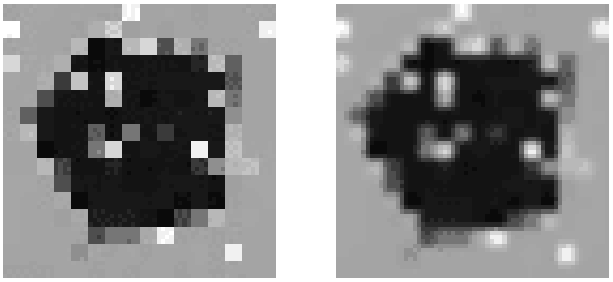


Figure 8: On the right is the noisy image solution of 40 Pixel Attack, and on the left is the pentagon shape with a Gaussian filter .

We found the solution using 100 population size, and for the 40-pixel attack, it took around 8 hours using one thread, evaluating entirely on the CPU, and 2 hours using 20 threads to find the solution for the 30-pixel attack with the same evaluation on the CPU.

Both solutions shown in Figures 7 and 8 change the original class from pentagon to cross. After we see that the solution change the original class to another one. We test the use of the Gaussian filter to clean the image, we obtain two results of the noise attack shown in Figures 7 and 8, and the filtered images are shown on the right of both Figures. The shapes are classified correctly after the application of the Gaussian filter. In this case, using the Gaussian filter on the input image, we can obtain the original class pentagon.

We repeated this experiment with different attack sizes using the same population size (400) as reported in the original article [2]. The results are shown in Table 5. For the single-pixel attack, we obtained an attack success rate of 0.54. After applying Gaussian filtering, this rate was reduced to 0.45. However, with a 20-pixel attack, Gaussian filtering proved ineffective at reducing the attack success rate. We attribute this behavior to the fact that 20 attacked pixels may exceed the filter's ability to recover the original signal.

3.5 One-pixel attack solved using simulated annealing

During testing of this attack, we evaluated different optimization algorithms as alternatives to differential evolution. We found that simulated annealing seek solutions faster than differential evolution. We got better performance using simulated annealing, from minutes per image to seconds per image. In the worst case, the maximum execution time was only 94 minutes.

The Figure 9 shows examples of adversarial images generated using differential evolution and simulated annealing. Both examples were attacked with 20 pixels. Given this significant performance difference, we expanded the test to 40 images with varying numbers of pixels and two different input sizes. The results are presented in Table 6.

Table 5: Results using one pixel attack with different number of pixels.

One pixel attack				
Num of Pixels	pop Size	Time Per Image	Success	Success after Gaussian filter
1	400	97 minutes	0.54	0.45
3	400	18 minutes	0.26	0.19
5	400	48 minutes	0.41	0.33
10	400	98 minutes	0.71	0.58
20	400	512 minutes	1.0	1.0

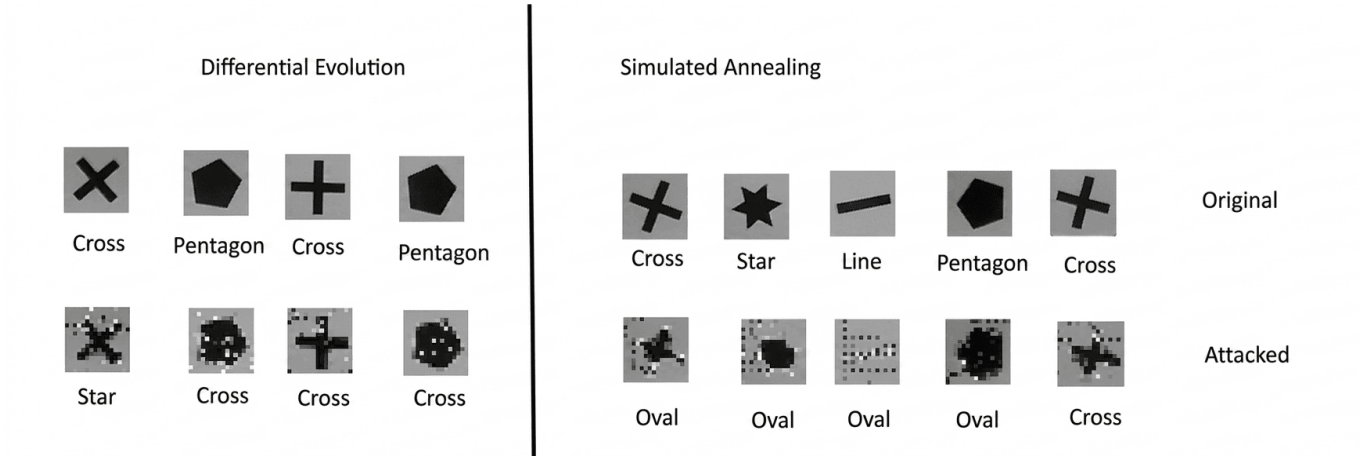


Figure 9: Examples of attacked images. On the left, the original implementation using differential evolution as an optimizer. On the right side are examples using simulated annealing as an optimizer.

Table 6: Results using one pixel attack with different number of pixels.

One pixel attack using simulated annealing as an optimizer.						
	64 × 64 rescaled to 16 × 16			32 × 32 rescaled to 16 × 16		
No.pixeles	Time	Attack Success	Gaussian filter	Time	Attack Success	Gaussian filter
20	94.04	0.70	**1.0**	84.74	0.84	**0.82**
10	46.19	0.63	**0.97**	41.63	0.76	**0.86**
5	22.95	0.43	**0.98**	20.64	0.67	**0.85**
1	4.52	0.08	**1.0**	4.09	0.21	**0.83**

4 Discussion

Perhaps our implementation needs to use a GPU to accelerate the evaluations, but the computational cost to search each solution is too high in comparison to solving using only a Gaussian filter to denoise the input images. In the case of one pixel attack noise, it is important to say that lot of details are loss when the original images are resized. The resizing algorithm is the nearest pixel value. We did not find any solution using a one pixel attack with images with the original size of 64×64 pixels.

Table 7 presents a comparison of our work with the original and the most recent work. Three key differences are that we test with a different input size, we use a dataset of well-formed shapes, and we employ a modern, well-established CNN architecture, EfficientNet.

Table 7: Comparison with related works

One pixel attack					
Work	Search method	Denoise Method	Better success rate	Better denoise rate	Image Size
Our work	Gaussian noise and one pixel attack (DE, SA)	Gaussian filter	0.54	0.86	32×32 and 64×64
[3]Most recent	GA,Random and DE	-	0.42	-	32×32
[2] First	DE	-	0.56	-	32×32

5 Conclusion

In conclusion, after we saw three methods to add noise in the images, the additive Gaussian noise, additive pink noise, and the one pixel attack, we found that the best way to denoise images is using simple filters like the Gaussian filter to enhance the classification model. One pixel attack is very effective, attacking architectures where the input size is too small, around 24×24 pixels, where the search field is small, but if the input size is too big it is necessary to resize the images to reduce the complexity of the search problem.

The Gaussian filter is a powerful and simple tool for denoising images when used as a preprocessing step with convolutional neural networks.

We observed that the usual attacks always use models with a reduced input image size. In this experiment, we test whether the problem is in the convolutional neural networks or in the images. That is why we tested a convolutional neural network that was trained with simple shapes in a reduced input size. Although the papers always test their attacks with original models with limited input sizes and resized inputs, we think the resize operation on the image produces information loss that helps enhance the attack. The problem is not the weakness of the convolutional neural networks; the problem is the use of reduced input size models trying to classify upscaled images. If the attack is added, it is probable that the model misclassifies. That was shown in the experiments, because we did not find any solution if we did not use a resized input image. The original implementations of the attacks used resized images and models with small input size images. In the same way, the problem increases where the search space is larger and the shapes are closer to the original size; the time to find a solution increases.

It is interesting that a simple Gaussian filter can be used as a preprocessing step to enhance accuracy. This suggests exploring the application of this filter to other types of noise. Additionally, it would be valuable to test these black-box attacks on more widely used CNN architectures, such as YOLO, and to investigate whether real-time black-box attacks are feasible.

For denoising images, trying alternative image preprocessing methods while keeping the processing lightweight for other kinds of noise would be valuable, because the methods explored in the references use complex methods to clean images.

References

[1] B. García-Morgado. "Análisis comparativo de algoritmos de clasificación de imágenes basados en aprendizaje automático tradicional y aprendizaje profundo". MA thesis. Cinvestav, 2024.

[2] J. Su, D.V. Vargas, and K. Sakurai. "One pixel attack for fooling deep neural networks". In: IEEE Transactions on Evolutionary C 23.5 (2019), pp. 828–841.

[3] Luana Clare, Alexandra Marques, and João Correia. "A Comparative Analysis of Evolutionary Adversarial One-Pixel Attacks". In: Applications of Evolutionary Computation. Ed. by Stephen Smith, João Correia, and Christian Cintrano. Cham: Springer Nature Switzerland, 2024, pp. 147–162. ISBN: 978-3-031-56855-8.

[4] M.W. Kusk and S. Lysdahlgaard. "The effect of Gaussian noise on pneumonia detection on chest radiographs, using convolutional neural networks". In: Radiography 29.1 (2023), pp. 38–43. DOI: 10.1016/j.radi.2022.09.011. URL: https://doi.org/10.1016/j.radi.2022.09.011.

[5] Teresa Kwamboka Abuya, Richard Maina Rimiru, and George Onyango Okeyo. "An Image Denoising Technique Using Wavelet-Anisotropic Gaussian Filter-Based Denoising Convolutional Neural Network for CT Images". In: Applied Sciences 13.21 (2023). ISSN: 2076-3417. DOI: 10.3390/app132112069. URL: https://www.mdpi.com/2076-3417/13/21/12069.

[6] Y. Bi, B. Xue, and M. Zhang. "Genetic Programming-Based Evolutionary Deep Learning for Data-Efficient Image Classification". In: IEEE Transactions on Evolutionary Computation 28.2 (2024), pp. 307–322. DOI: 10.1109/TEVC.2022.3214503.

[7] Y. Bi, M. Zhang, and B. Xue. "Genetic Programming for Automatic Global and Local Feature Extraction to Image Classification". In: 2018 IEEE Congress on Evolutionary Computation (CEC). 2018, pp. 1–8. DOI: 10.1109/CEC.2018.8477911.

[8] G. Olague. Evolutionary Computer Vision. Springer Science+Business Media, Jan. 2016. DOI: 10.1007/978-3-662-43693-6. (Visited on 11/12/2024).

[9] S.M. Moosavi-Dezfooli, A. Fawzi, and P. Frossard. "DeepFool: A Simple and Accurate Method to Fool Deep Neural Networks". In: Proceedings of the IEEE Conference on Computer Vision and Pattern Recognition (CVPR). June 2016, pp. 2574–2582.

Journal of Dynamical Systems and Complexity (2026) vol.1(3): 23-35
eISSN: 3122-4326, DOI: 10.66131/JDSC12202623-35

Experimental Evaluation of a Hartley Oscillator Incorporating a Commercial SDC Memristor

Luis Manuel Jimenez Lopez*, Alejandro Diaz Sánchez, Esteban Tlelo Cuautle

Department of Electronics, Instituto Nacional de Astrofísica, Óptica y Electrónica (INAOE), Luis Enrique Erro No. 1, Santa María Tonantzintla, San Andrés Cholula 72840, Puebla, Mexico.

Abstract

This paper experimentally investigates the integration of a commercial Self-Directed Channel (SDC) memristor into a Hartley oscillator. While most existing literature relies on theoretical models or emulators, this work utilizes a physical W-type (tungsten-based) memristor to analyze its direct impact on the oscillator's periodic steady-state response. The experimental setup, implemented with a TL081CD operational amplifier and an Analog Discovery Studio platform, demonstrates that the memristor acts as a dynamic feedback element. Comparative results show that including the memristive device increases the peak-to-peak amplitude by 34% (from 2.724 V to 3.65 V) and shifts the frequency down from 14.530 kHz to 14.213 kHz. Furthermore, the memristor-based oscillator showed an additional startup interval of about 2 s, with an estimated relative variation of ±27% across repeated experiments. This behavior suggests a modified oscillator transient response, potentially linked to the SDC device's history-dependent electrical characteristics. The results indicate that the memristor-augmented Hartley oscillator maintains a stable sinusoidal waveform, suggesting that the device's state-dependent resistance can effectively modulate the system's gain and resonance conditions in analog circuit architectures.

Keywords— memristor, Hartley oscillator, frequency, amplitude

1 Introduction

Electronic oscillators are fundamental building blocks in modern engineering, generating periodic signals without external excitation. These circuits are widely used in communication systems, instrumentation, and signal processing, and serve as timing references in electronics. Among these topologies, LC-resonant oscillators are particularly important for producing stable, high-frequency waveforms.

A prominent member of this family is the Hartley oscillator, which uses a resonant tank circuit with a capacitor in parallel with a tapped inductor to set its oscillation frequency. The inductive

*Corresponding author: luismanuel1975@outlook.es
Received: Jun 24, 2026, **Published:** October 30, 2026
Editor: E. Campos-Cantón

element is typically implemented as two series-connected coils or a single coil with a tap, providing the feedback needed to sustain oscillations. This configuration satisfies the Barkhausen criterion: the total phase shift around the loop is zero, and the loop gain is greater than or equal to unity.

A key advantage of the Hartley topology is its simplicity: it requires fewer components than other LC oscillators while still providing stable sinusoidal outputs over a wide frequency range. Its inductive feedback also makes it suitable for high-frequency and radio-frequency signal-generation and communication applications.

The memristor has emerged as the fourth fundamental passive element, complementing the resistor, capacitor, and inductor [1]. Chua predicted that, apart from resistors, capacitors, and inductors, a fourth fundamental passive circuit element should exist: the memristor, defined by the constitutive relationship between electric charge and magnetic flux [2]. It has a nonlinear voltage-current relationship and state-dependent resistance (memristance), offering unique properties for neuromorphic computing, non-volatile memory, and adaptive electronic systems [3, 4].

In 2008, researchers at Hewlett-Packard Labs announced one of the first physical solid-state memristors. Since then, interest in exploiting this emerging circuit element has grown, especially in analog circuitry and non-volatile memory applications [2].

In 2015, the American company Knowm Inc. designed and produced the world's first Knowm memristor packaged as a chip. Unlike the oxygen-vacancy migration technology used in HP memristors, Knowm memristors use metal-ion migration for electrical switching [4]. Knowm memristors provide researchers with a commercially available, effective device for related application studies [5].

While recent studies have explored integrating memristors into oscillator circuits to modulate their dynamics, much of this research remains grounded in theoretical models or emulators [6, 7, 8, 9, 10]. Experimental implementations of physical, discrete memristive devices remain relatively scarce. Unlike idealized models, physical memristors exhibit non-ideal dynamics that depend on excitation frequency, polarity, and prior stimulus history, which may critically influence the operation of resonant oscillators [4, 11].

This work investigates a Hartley oscillator incorporating a commercial memristor (Knowm Inc.) in its feedback network. The study moves from circuit simulations to experimental validation, examining the memristor's impact on critical parameters, including oscillation frequency, amplitude stability, and waveform symmetry.

2 Hartley Oscillator

Figure 1 shows the Hartley oscillator. It is a widely used LC oscillator topology that generates periodic signals through a resonant network of inductors and capacitors, combined with an amplifying stage that provides the feedback needed to sustain oscillations. Ralph V. L. Hartley originally proposed the circuit in the early twentieth century, and it has since been widely used in radio-frequency systems for its relatively simple configuration and ease of frequency tuning.

The equivalent inductance of the inductive network and the resonant-tank capacitance determine the Hartley oscillator's oscillation frequency. Under ideal conditions, the oscillation frequency can be approximated by:

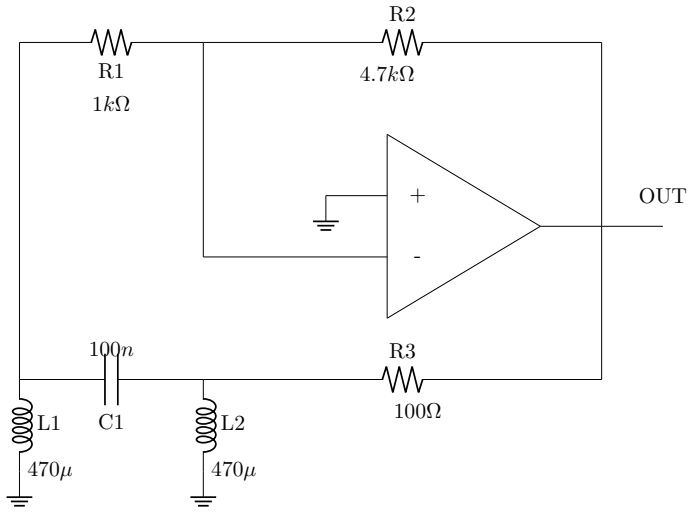


Figure 1: Hartley oscillator circuit.

$$f = \frac{1}{2\pi\sqrt{C(L_1 + L_2)}} \tag{1}$$

where L_1 and L_2 are the inductances of the series inductors, and C is the resonant capacitor's capacitance. By adjusting either the inductance or the capacitance, it is possible to tune the circuit's oscillation frequency.

One of the Hartley oscillator's main advantages is its simple design and frequency tunability. However, practical implementations may deviate from the ideal sinusoidal waveform due to component tolerances, nonlinearities in the active device, and parasitic effects in the circuit.

From a system-level perspective, incorporating a memristive device into the Hartley oscillator introduces a dynamic, state-dependent element into the feedback network. In the conventional topology, a fixed relationship between the inductive feedback ratio and the amplifier gain governs the oscillation condition, ensuring the Barkhausen criteria are satisfied under steady-state conditions. However, replacing or augmenting part of the feedback path with a memristor makes the effective resistance time-varying and history-dependent.

This modification directly affects the loop gain and the impedance seen by the resonant tank, allowing the memristor to modulate oscillation conditions in real time. As a result, key parameters such as amplitude stabilization, startup dynamics, and even the steady-state frequency may deviate from predictions of classical linear models. Unlike conventional resistive elements, the memristor exhibits nonlinear, adaptive behavior that can produce transient phenomena tied to internal-state evolution, such as delayed stabilization or gradual amplitude adjustment.

Therefore, integrating a physical memristor into the Hartley oscillator not only alters its electrical characteristics but also provides a platform for experimentally observing how state-dependent devices influence resonant systems beyond idealized assumptions.

3 Knowm W-type Memristor

The memristive device integrated into the Hartley oscillator is a commercial Self-Directed Channel (SDC) memristor from Knowm, Inc. The implementation uses a W-type (tungsten-based) memristor, whose hysteretic behavior is experimentally characterized using the Analog Discovery 2 Kit, as shown in Fig. 2. This hysteresis loop, observed in the current–voltage (I–V) relationship, is a defining feature of memristive systems and reflects the device's state-dependent resistance.

Unlike transition-metal oxide memristors that rely primarily on oxygen vacancy migration, the SDC memristor operates through the controlled movement of metal ions, typically silver (Ag^+), within a chalcogenide layer. This process forms and dissolves conductive filaments, dynamically modulating device resistance. As a result, the memristor exhibits a nonlinear, history-dependent response, making it particularly suitable for applications involving adaptive or time-varying behavior.

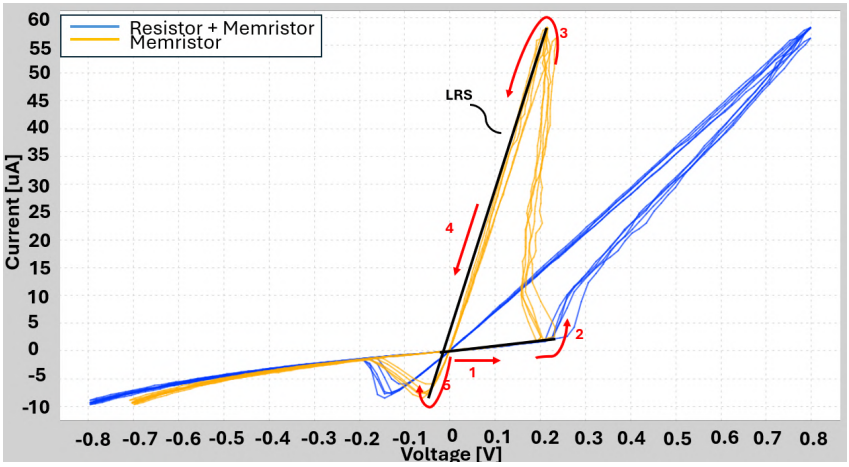


Figure 2: I–V characteristic of the Knowm memristor.

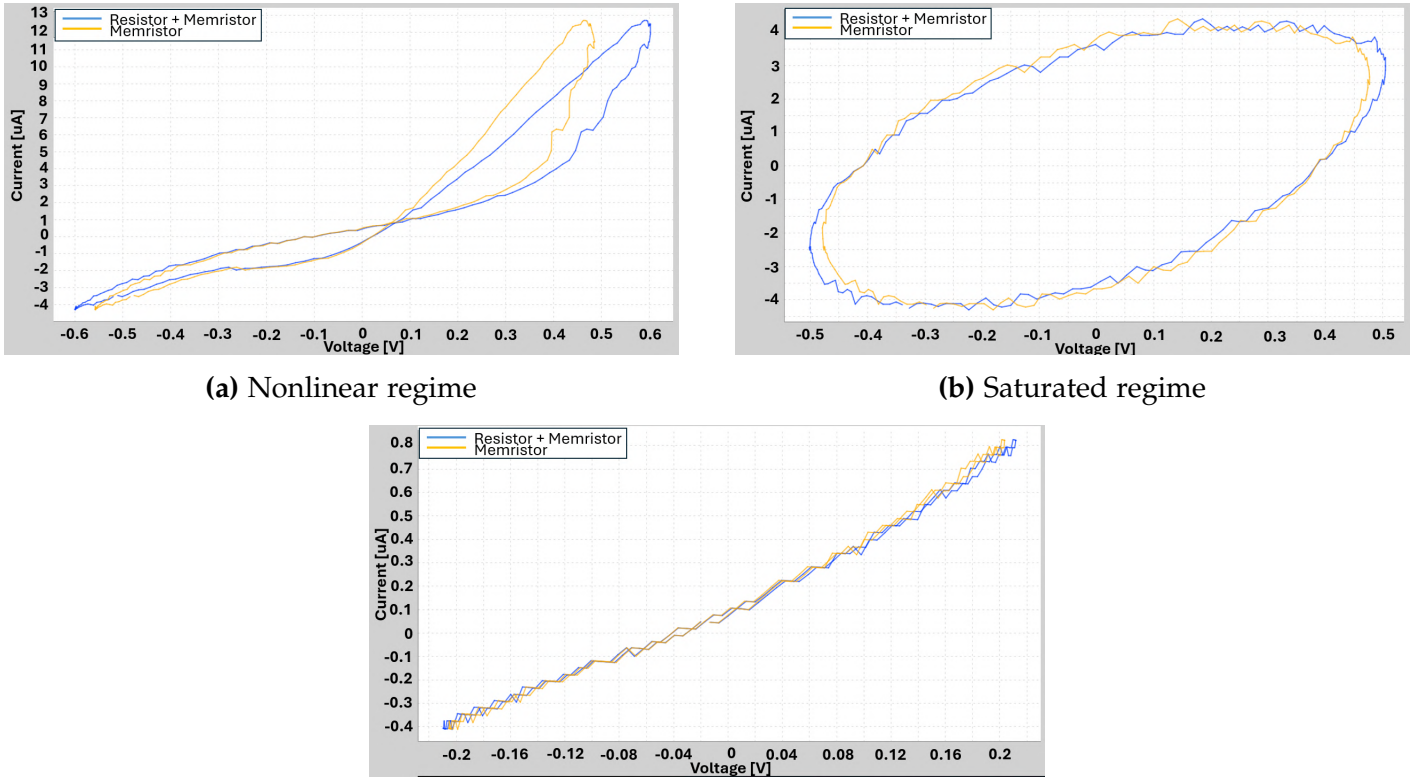
For this study, we estimated the memristor's effective resistance from the quasi-linear region of the measured I–V characteristic curve (Fig. 2) using Ohm's law, $R = V/I$. This characterization establishes an initial low-resistance state (Rinitial) of approximately $4\,\mathrm{k\Omega}$. This approximation provides a practical representation of the device within the operating region of interest, enabling its integration into the oscillator circuit analysis while preserving its dominant electrical behavior.

To ensure experimental consistency and mitigate the stochastic nature of filament formation, we applied a controlled state-reset protocol before measurements. The device recovers using a 10 Hz sinusoidal signal with an amplitude of 1 V. Additionally, a $-2\,\mathrm{V}$ is applied for 2 s, driving Ag^+ ions toward the anode and dissolving previously formed conductive filaments to restore the device to a reproducible baseline state.

This initialization process is critical to the Hartley oscillator's reliability, as it ensures the memristor starts from a well-defined resistance state before the dynamic feedback loop begins to influence its conductance. Because the oscillator's behavior is highly sensitive to variations in loop gain and impedance, uncertainty in the initial memristive state could significantly degrade frequency stability and amplitude response. This controlled initialization enables a more accurate evaluation of the memristor's impact on the oscillation dynamics.

To further assess the operational stability of the memristor-based oscillator, we evaluated continuous operation for up to 2 h. During these intervals, the oscillator maintained sustained oscillations without noticeable deviations in output behavior or operational failures and required no additional memristor resetting or retuning. We performed the reset and characterization procedures between experimental trials to establish comparable initial conditions, rather than in response to a loss of stability during operation. These observations suggest that, under the tested conditions, the commercial SDC memristor can remain functional within the oscillator for extended operating intervals without frequent readjustment. Nevertheless, the experiments do not establish their long-term stability beyond the evaluated duration.

3.1 Memristor Operating Window



(a) Nonlinear regime

(b) Saturated regime

(c) Quasi-linear regime

Figure 3: Initial experimental I–V characterization of the commercial Knowm W-type SDC memristor under sinusoidal excitation at different frequencies: (a) 10 kHz, exhibiting a nonlinear operating region; (b) 1 MHz, showing a saturated O-shaped response; and (c) 10 Hz, presenting a quasi-linear regime in which the device behaves predominantly as a resistance.

Before using it as a circuit element, we evaluated the Knowm W-type memristor under various excitation conditions to identify its practical operating window. This step is important because the device response depends not only on its intrinsic memristive properties but also on the applied voltage amplitude, excitation frequency, offset voltage, and initial resistive state. Therefore, a

memristor inserted into an oscillator should not be assumed to operate in a useful nonlinear regime without prior characterization.

Figure 3 shows representative I-V responses obtained during the initial characterization. Under suitable excitation conditions, the device exhibits a nonlinear hysteretic response, indicating active, observable memristive dynamics. However, outside this operating region, two limiting cases may appear. At low excitation levels, the hysteresis loop can collapse to a quasi-linear characteristic, causing the device to behave primarily as an equivalent resistor. In contrast, under other excitation conditions, the response can evolve into a closed O-shaped curve, associated with a saturated or strongly limited regime. In both cases, the dynamic memristive contribution becomes less distinguishable, which can lead to incorrect interpretations when the device is later integrated into an oscillator.

For this reason, we used the initial I-V characterization to select operating conditions where the memristor maintained a measurable nonlinear response before replacing individual resistors in the oscillator.

3.2 Mathematical Description of the Memristive Device

The Mean Metastable Switch (M-MSS) model developed by Knowm [12, 13] describes memristive behavior by representing resistance modulation through voltage-dependent transitions between metastable states. The model introduces an internal state variable x, ranging from 0 to 1, whose temporal evolution is expressed as

$$\frac{dx}{dt} = (1-x)P_{\mathrm{OFF}\to\mathrm{ON}} - xP_{\mathrm{ON}\to\mathrm{OFF}}, \tag{2}$$

where the transition rates are defined as

$$P_{\mathrm{OFF}\to\mathrm{ON}} = \frac{1}{\tau}\frac{1}{1+\exp\left[-\frac{V-V_{\mathrm{ON}}}{V_T}\right]}, \tag{3}$$

$$P_{\mathrm{ON}\to\mathrm{OFF}} = \frac{1}{\tau}\frac{1}{1+\exp\left[\frac{V+V_{\mathrm{OFF}}}{V_T}\right]}. \tag{4}$$

Here, V is the applied voltage, τ is the characteristic time constant, V_{ON} and V_{OFF} are switching parameters, and V_T is the thermal voltage.

The state-dependent conductance is given by

$$G(x) = \frac{x}{R_{\mathrm{ON}}} + \frac{1-x}{R_{\mathrm{OFF}}}, \tag{5}$$

where R_{ON} and R_{OFF} represent the limiting resistance states. Accordingly, the memristive current can be expressed as

$$I_M(V,x) = VG(x). \tag{6}$$

The M-MSS formulation also permits an additional nonlinear Schottky contribution to the total current. In this work, we introduce these relationships as a phenomenological description of

memristive behavior rather than a quantitatively calibrated representation of the specific Knowm W-type SDC device. We obtain the results presented here through direct experimental measurements on the physical memristor, without relying on numerical predictions from the mathematical model.

4 Experimental Implementation

This study used a discrete Knowm M+SDC device (W-type, tungsten-based) packaged in a 16-DIP configuration as the memristive element. Before integrating it into the oscillator, we characterized the device to verify its I–V hysteresis behavior and establish a reproducible initial low-resistance state (LRS), as described in the previous section. This preconditioning step is essential because filament formation in SDC memristors is stochastic.

For the memristor-augmented configuration, we inserted the device into the feedback path with a defined polarity, as shown in Fig. 4. This placement ensures that the oscillating voltage directly influences the internal ionic dynamics, allowing the memristance to evolve in response to circuit operation. Consequently, the memristor acts as a dynamic element within the feedback loop, modifying the effective gain and impedance during oscillation.

The Digilent Analog Discovery Studio powered and monitored the circuit, providing a stable, symmetrical $\pm 12\,\mathrm{V}$ supply to the active elements. The platform's integrated digital oscilloscope and waveform generator enabled real-time data acquisition and signal analysis, allowing precise characterization of the output waveforms in both the standard and memristor-augmented configurations.

To reduce instrumental errors and improve measurement accuracy, the Analog Discovery 2 was calibrated using WaveForms software and an external digital multimeter. The calibration procedure covered the waveform generators, acquisition channels, and power supplies. The resulting calibration parameters were stored by the device and applied to correct generated and acquired signals. This procedure helps mitigate systematic measurement errors.

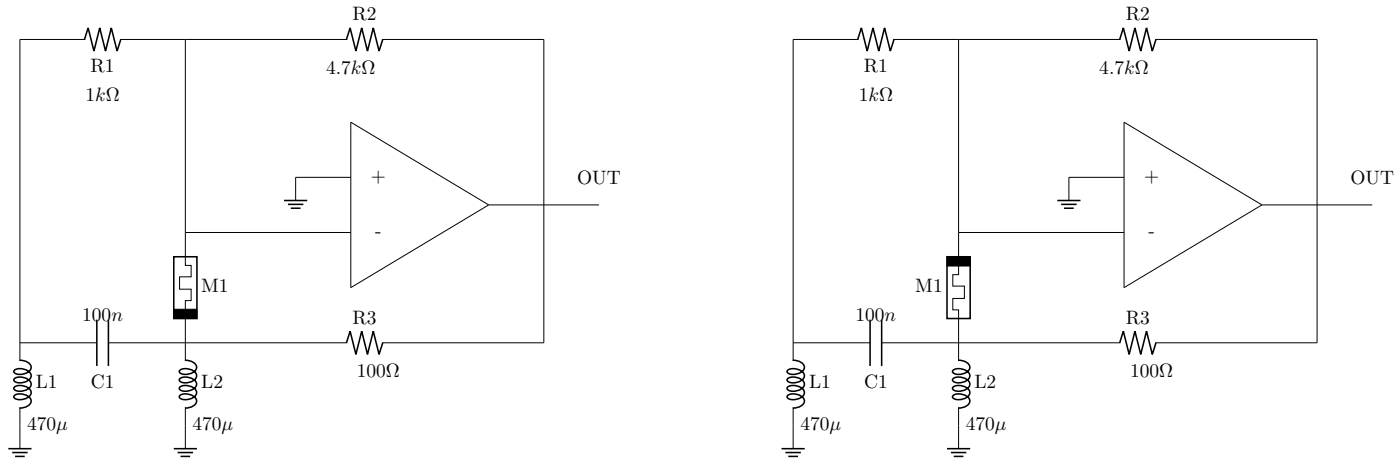
To ensure a fair comparison, we evaluated three configurations: the conventional Hartley oscillator and two memristor-based configurations that differed only in the polarity of the physical device. All other circuit components and connections remained unchanged, allowing us to examine how memristor orientation affects the oscillatory response experimentally.

For the Hartley oscillator, we evaluated two memristor-based configurations to analyze how device placement affects the output response. Figure 4 shows the corresponding circuits. In the first configuration, the oscillator maintained a frequency close to the standard circuit, changing from 14.530 kHz to 14.213 kHz.

In the second memristor-based configuration, the oscillator response changed more strongly. The output frequency increased to 18.11 kHz, while the maximum and minimum voltages reached 4.32 V and -4.315 V, respectively, resulting in a peak-to-peak voltage of 8.635 V.

Both circuits employ identical components and connection points, with the memristor occupying the same position within the oscillator. The only difference between the configurations is the device's orientation: in Case 1, the memristor is connected to its original polarity, whereas in Case 2, its polarity is reversed. This arrangement lets us evaluate the memristor orientation's influence on the oscillator response without changing the circuit topology or component values.

The oscillator's active core consists of a TL081CD operational amplifier. We selected this JFET-



(a) Memristor case 1

(b) Memristor case 2

Figure 4: Hartley oscillator circuits incorporating the memristor under two different configurations used in this work.

input device for its high input impedance and 13 V/μs slew rate, which prevent significant phase distortion or amplitude clipping at the target operating frequency of 14 kHz. As seen in Fig. 1, the resonant network was constructed using nominal values for all components, featuring two 470 μH inductors (L_1, L_2) and a 100 nF ceramic capacitor (C_1); the feedback and bias network was completed with a 1kΩ resistor (R_1), a 4.7kΩ resistor (R_2), and a 100Ω shunt resistor (R_3), the latter serving to stabilize the current path through the feedback loop. We conducted all measurements under steady environmental conditions and performed multiple trials to verify repeatability. We recorded and analyzed the output waveforms for frequency, amplitude, duty cycle, and transient response, enabling a comprehensive comparison between the conventional and memristive oscillator configurations.

5 Results and Discussion

The experimental evaluation of the Hartley oscillator revealed that integrating the W-type Knowm memristor produces configuration-dependent changes in the output response. As summarized in Table 1, we compared two memristor-based configurations with the standard LC oscillator to assess how device placement affects oscillation frequency, voltage swing, and temporal symmetry.

Repeatability was evaluated across eight experimental trials for each memristor configuration. The frequency coefficient of variation (CV) decreased from 1.67% in Case 1 to 1.26% in Case 2, indicating lower relative variability in frequency for the latter configuration. For the voltage measurements, the CVs of V_{max}, V_{min}, and V_{PP} were 6.52%, 8.27%, and 6.395% for Case 1, respectively, compared with 7.62%, 10.95%, and 9.257% for Case 2. These results indicate that, although Case 2 exhibited lower relative variability in frequency, its voltage-related measurements showed greater relative dispersion than those of Case 1. The results therefore reveal parameter-dependent repeatability across the two configurations.

In the first memristor configuration, the output amplitude changed most significantly. The

standard Hartley oscillator produced a peak-to-peak voltage of 2.724 V, whereas Memristor Case 1 increased this value to 3.65 V. This represents an approximately 34% increase in the voltage swing. Similarly, the amplitude increased from 1.36 V to 1.825 V. This behavior suggests that, in this configuration, the memristor modifies the oscillator's effective feedback conditions, increasing the output signal's steady-state energy level without forcing the waveform into supply-rail saturation.

Table 1: Performance comparison between the standard oscillator and two memristor-based oscillator cases.

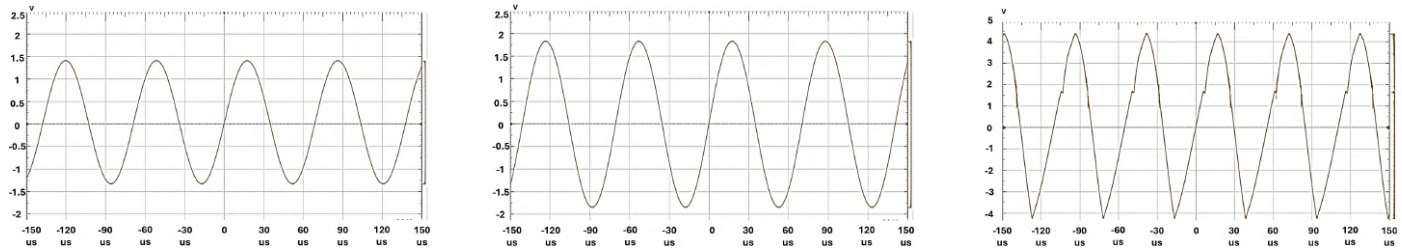
Parameter	Standard Oscillator	Memristor Case 1	Memristor Case 2
Frequency	14.530 kHz	14.213 kHz	18.11 kHz
Amplitude	1.36 V	1.825 V	4.318 V
V Max	1.415 V	1.8 V	4.32 V
V Min	-1.31 V	-1.85 V	-4.315 V
Vpp	2.724 V	3.65 V	8.635 V
PosDuty	50.04%	50.05%	51.33%
NegDuty	49.97%	49.95%	48.67%
PosWidth	34.435 μs	35.214 μs	29.015 μs
NegWidth	34.386 μs	35.146 μs	27.509 μs

Based on the nominal values of the resonant components ($L_1 = L_2 = 470$ μH and C1 = 100 nF), the conventional Hartley oscillator's theoretical oscillation frequency is approximately 16.42 kHz, assuming negligible mutual inductance between the inductors. The experimentally measured frequency was 14.530 kHz, representing a deviation of approximately -11.5% from the theoretical prediction. This discrepancy may result from non-ideal circuit characteristics, including component tolerances, parasitic impedances, and the operational amplifier's frequency-dependent response. These factors should be considered when comparing the ideal resonant frequency with the physical oscillator's measured behavior.

Memristor Case 1 showed a slight frequency reduction from 14.530 kHz to 14.213 kHz (2.18%), indicating that the Hartley oscillator's resonant behavior was largely preserved. This variation may reflect the SDC device's non-ideal electrical characteristics and its interaction with the feedback network. Waveform symmetry remained practically unchanged, with positive and negative duty cycles of 50.05% and 49.95%, respectively.

In contrast, Memristor Case 2 increased the oscillation frequency to 18.11 kHz (24.6% above the standard configuration) and the peak-to-peak voltage to 8.635 V, approximately 3.17 times the reference value. The corresponding amplitude reached 4.318 V. The waveform also showed moderate asymmetry, with positive and negative duty cycles of 51.33% and 48.67%, and pulse widths of 29.015 μs and 27.509 μs, respectively.

The two memristor-based configurations differ only in the device's polarity, while its position within the Hartley oscillator remains unchanged. Reversing the memristor polarity increased the frequency from 14.213 kHz to 18.110 kHz (approximately 27.4%) and the amplitude from 1.825 V to 4.318 V (approximately 136.6%). This polarity-dependent response is consistent with the asymmetric conductance-switching behavior of Knowm SDC memristors, where the applied voltage direction influences the evolution of the internal conductive state. Under alternating excitation,



(a) Standard Hartley oscillator waveform.

(b) Hartley oscillator including memristor (Case 1).

(c) Hartley oscillator including memristor (Case 2).

Figure 5: Experimental waveform comparison between the standard Hartley oscillator and two configurations incorporating the physical memristor, obtained using the Digilent Analog Discovery measurement system.

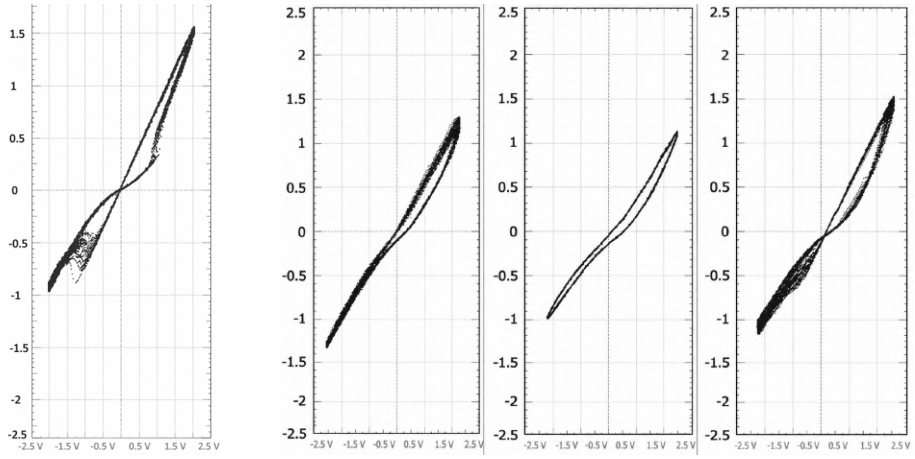
reversing the device orientation changes the relationship between the oscillator voltage and the memristor's conductance evolution, potentially modifying the circuit's effective impedance and feedback conditions.

These results show that the memristor does not behave as a simple passive replacement for a fixed resistor. Instead, its effect depends strongly on its position within the oscillator structure and on its interaction with the resonant and feedback paths. In Memristor Case 1, the device mainly increased the output amplitude while preserving the frequency and duty-cycle symmetry. In contrast, Memristor Case 2 produced a higher-frequency, higher-amplitude response but also introduced slight waveform asymmetry. Therefore, the Hartley oscillator confirms that integrating physical memristive devices can enable adaptive tuning. However, the resulting behavior must be interpreted in light of the specific circuit configuration and the memristor's operating region.

The memristor-based Hartley oscillator consistently showed an additional startup interval of approximately 2 s before reaching a stable oscillatory regime. We evaluated this behavior using two complementary methods: direct observation of the output waveform and subsequent analysis of the recorded numerical data. Across repeated experiments, the observed delay varied by approximately ±27% around the nominal 2 s value, corresponding to an estimated range of 1.46–2.54 s. Before each experiment, we reset and characterized the memristor to establish comparable initial operating conditions. This delay provides experimental evidence of the memristor's state evolution; the initial cycles of the oscillating voltage must provide sufficient charge flow to "train" or stabilize the silver filaments within the SDC layer. Once the memristance reaches its operational equilibrium, the waveform stabilizes into a remarkably pure sine wave, as shown in the oscilloscope captures given in Fig. 5. The absence of significant harmonic distortion, despite the increased amplitude, further confirms that the tungsten-based (W-type) memristor provides stable, reliable nonlinear regulation, making it a viable component for adaptive signal generation in LC topologies.

As an additional control, we replaced the physical memristor with a fixed resistor matching its initial resistance (4 kΩ), while keeping the remaining circuit components unchanged. Under these conditions, the Hartley oscillator operated at 15.737 kHz with a peak-to-peak voltage of 2.950 V. In comparison, the memristor-based configurations operated at 14.213 kHz and 18.110 kHz, with peak-to-peak voltages of 3.650 V and 8.635 V, respectively. These differences indicate that the initial resistance value alone is insufficient to reproduce the memristor-based oscillator's measured response.

During operation within the Hartley oscillator, the memristor exhibited a dynamic response near the boundary between the nonlinear and saturated regimes. The measured I–V trajectories showed variations between these two behaviors rather than remaining confined to a single stationary regime. This observation indicates that the operating conditions imposed by the oscillator do not necessarily correspond to a fixed memristive state.



(a) Case 1 **(b)** Case 2

Figure 6: I-V plot of the memristor during oscillator operation

6 Conclusions

We evaluated two memristor-based configurations that differ only in the device's polarity within the circuit. The results show that the memristor's physical orientation directly influences the oscillator dynamics, affecting not only the output amplitude but also the oscillation frequency and waveform symmetry.

In Memristor Case 1, the circuit preserved a frequency close to that of the standard Hartley oscillator. The frequency changed from 14.530 kHz to 14.213 kHz, a reduction of about 2.18%. However, the peak-to-peak voltage increased from 2.724 V to 3.65 V, representing an amplitude enhancement of approximately 34%. This indicates that, under this polarity, the memristor mainly modifies the effective feedback conditions and increases the steady-state voltage swing without significantly disturbing the waveform's temporal symmetry.

In contrast, Memristor Case 2 produced a stronger modification of the oscillator response. Reversing the memristor polarity increased the oscillation frequency to 18.11 kHz. It raised the peak-to-peak voltage to 8.635 V, corresponding to a frequency increase of approximately 24.6% and a voltage swing more than three times larger than that of the standard oscillator. In addition, the duty cycle changed from an almost symmetric condition to 51.33% positive duty and 48.67% negative duty, indicating that the reversed polarity introduces a moderate asymmetry in the oscillatory response.

A relevant observation was a startup transient before the system reached a stable oscillatory regime. This behavior suggests that the SDC memristor's internal state evolves during the first excitation cycles before reaching an operational equilibrium. Once it stabilizes, the oscillator can

maintain a stable sinusoidal output, showing that a physical memristive device can integrate into an LC oscillator while preserving sustained oscillation, provided it operates within an appropriate electrical regime.

Overall, these findings show that commercial memristors can serve as polarity- and state-dependent elements for tuning analog oscillator circuits. The comparison between the two memristor orientations confirms that the device does not behave as a simple fixed-resistance replacement; instead, its nonlinear, directional response interacts with the oscillator's feedback and resonant paths. Therefore, prior device characterization and careful consideration of memristor polarity are essential for correctly interpreting and designing memristor-based oscillator systems.

References

[1] Leon O. Chua. "Memristor—The Missing Circuit Element". In: *IEEE Transactions on Circuit Theory* 18.5 (1971), pp. 507–519. DOI: 10.1109/TCT.1971.1083337.

[2] Olufemi A. Olumodeji and Massimo Gottardi. "A pulse-based memristor programming circuit". In: *2017 IEEE International Symposium on Circuits and Systems (ISCAS)*. 2017, pp. 1–4. DOI: 10.1109/ISCAS.2017.8050793.

[3] Luis M. Lopez-Jimenez, Fabiola Muños Vera, and Alejandro Diaz Sanchez. "Impact of Individual Memristor Replacements on Frequency and Amplitude in RC Phase-Shift Oscillators". In: *Complex Systems and Their Applications*. Ed. by Ulises Uriostegui-Legorreta et al. Cham: Springer Nature Switzerland, 2026, pp. 49–64. ISBN: 978-3-032-25152-7. DOI: https://doi.org/10.1007/978-3-032-25152-7_4.

[4] L. M. Lopez-Jimenez et al. "Experimental Evaluation of Memristor-Enhanced Analog Oscillators: Relaxation and Wien-Bridge Cases". In: *Dynamics* 5.4 (2025), p. 43. DOI: 10.3390/dynamics5040043.

[5] Leixin Zhang and Xuefang Xiao. "Twin-T Network Oscillator Based on Knowm Memristors". In: *2024 6th International Conference on Electronics and Communication, Network and Computer Technology (ECNCT)*. 2024, pp. 459–462. DOI: 10.1109/ECNCT63103.2024.10704244.

[6] A. Karthikeyan et al. "A Simple Chaotic Wien Bridge Oscillator with a Fractional-Order Memristor and Its Combination Synchronization for Efficient Antiattack Capability". In: *Complexity* 2021 (2021). DOI: 10.1155/2021/8857075.

[7] V. Rakitin, S. Rusakov, and S. Ulyanov. "The Coupled Reactance-Less Memristor-Based Relaxation Oscillators for Binary Oscillator Networks". In: *Micromachines* 14.2 (2023), p. 365. DOI: 10.3390/mi14020365.

[8] R. Dutta, A. Karmakar, and S. Kundu. "A Review on Memristor-Based Reactance-Less Relaxation Oscillator". In: *Lecture Notes in Electrical Engineering*. Vol. 1046. Springer, 2023. DOI: 10.1007/978-981-99-1695-3_44.

[9] F. Setoudeh and M. M. Dezhdar. "An Overview of Sinusoidal Oscillators Based on Memristive Devices". In: *IntechOpen*. IntechOpen, 2024. DOI: 10.5772/intechopen.113403.

[10] E. Solovyeva, A. Serdyuk, and Y. Inshakov. “Tunable Active Wien Filters Based on Memristors”. In: *Micromachines* 16.7 (2025), p. 769. DOI: 10.3390/mi16070769.

[11] Adam Nugent. *Knowm Memristor Discovery Manual*. Knowm Inc., 2020.

[12] Timothy W. Molter and M. Alexander Nugent. “The Generalized Metastable Switch Memristor Model”. In: *2016 15th International Workshop on Cellular Nanoscale Networks and Their Applications (CNNA)*. Dresden, Germany, 2016, pp. 1–2.

[13] Tim Molter and Alex Nugent. *The Mean Metastable Switch Memristor Model in Xyce*. Knowm Inc. 2017. URL: https://knowm.org/the-mean-metastable-switch-memristor-model-in-xyce/.

Journal of Dynamical Systems and Complexity (2026) vol.1(3): 36-49
eISSN: 3122-4326, DOI: 10.66131/JDSC12202636-49

Convergence Analysis of the Kuramoto Model via Mean-Field Coupling for Micro-Generation Networks

A. Rincón-Silva*, R. R. Rivera-Durón , J. O. Orozco-López

Departamento de Ciencias Exactas y Tecnología, Centro Universitario de los Lagos, Universidad de Guadalajara.
Av. Enrique Díaz de León 1144, Col. Paseos de la Montaña, C.P. 47460, Lagos de Moreno, Jalisco, México.
* Corresponding author email: adan.rincon@alumnos.udg.mx
Emails: roberto.rivera@lagos.udg.mx, juan.onofre@academicos.udg.mx

Abstract

This work investigates the convergence and stability of a decentralized synchronization architecture for networks of Permanent Magnet Synchronous Generators (PMSGs) based on mean-field coupling within the Kuramoto framework. The proposed approach replaces explicit pairwise phase interactions with a collective order parameter, enabling each generator to adjust its dynamics relative to the network centroid. Local phase and frequency estimation is performed through a Synchronous Reference Frame Phase-Locked Loop (SRF-dqPLL), while an adaptive-gain control law regulates the synchronization process. The convergence properties are examined through analytical stability considerations and continuous-time simulations of a four-node PMSG network implemented in Simulink. Under heterogeneous initial frequencies, the numerical results demonstrate convergence toward a common operating frequency, followed by a progressive reduction of phase mismatch without sustained oscillations. Furthermore, the mean-field formulation enables a reduction in the computational complexity of the coupling interactions from $O(N^2)$ to $O(N)$, supporting the scalability of the proposed architecture. These findings support the feasibility of the proposed approach for decentralized micro-generation synchronization and provide a basis for future implementation in resource-constrained embedded systems.

Keywords— Kuramoto model, mean-field coupling, Decentralized synchronization

1 Introduction

The synchronization of coupled oscillators has been extensively investigated through the Kuramoto model, which provides a mathematical framework for understanding the emergence of collective behavior in interacting dynamical systems. In particular, Benedetto et al. [1] studied complete phase synchronization in the mean-field limit, establishing theoretical results on the collective evolution of oscillator populations under specific conditions. These developments highlight the relevance of mean-field descriptions for analyzing synchronization phenomena and motivate their application to finite networks of interacting dynamical units. However, extending these theoretical concepts to electromechanical systems requires considering additional factors, including heterogeneous operating conditions, state estimation, and control dynamics.

The increasing integration of distributed energy resources has motivated the development of decentralized control architectures capable of coordinating multiple generation units while reducing their dependence on centralized supervisory systems [2]. In micro-generation networks operating under islanded conditions, maintaining consistent electrical frequency and phase relationships among individual generators is essential for coordinated operation and eventual interconnection. This challenge becomes particularly relevant for Permanent Magnet Synchronous Generators (PMSGs), whose operating frequencies may differ due to variations in mechanical input conditions. Consequently, synchronization strategies must accommodate heterogeneous initial states while providing stable transient responses and remaining suitable for implementation in resource-constrained embedded systems.

The theoretical foundations of oscillator synchronization have been extensively reviewed by Acebrón et al. [3], while Rodrigues et al. [4] examined the Kuramoto model in complex networks, emphasizing the influence of coupling structures on collective dynamics. In conventional pairwise formulations, the synchronization interaction is determined by the phase differences between connected oscillators. For fully connected networks, the direct evaluation of these interactions requires a computational effort that grows quadratically with the number of nodes. Mean-field coupling provides an alternative representation by describing the collective state through a complex

*Corresponding author: adan.rincon@alumnos.udg.mx
Received: September 15, 2026, **Published:** October 31, 2026
Editor: J.L. Echenausía-Monroy

order parameter that characterizes network coherence. This formulation allows the synchronization interaction to be evaluated relative to a common reference phase, avoiding the explicit calculation of every pairwise phase difference and reducing the associated computational effort.

Beyond the coupling formulation, practical synchronization depends on the availability of reliable phase and frequency estimates. Phase-Locked Loop (PLL) techniques are widely employed in renewable energy systems to extract synchronization variables from electrical measurements. Ali et al. [5] reviewed three-phase PLL algorithms and examined their performance under different operating conditions, highlighting the importance of estimation accuracy and transient response. In this context, the Synchronous Reference Frame PLL (SRF-dqPLL) provides a suitable mechanism for estimating local electrical states without requiring direct mechanical position measurements. Combining such estimators with distributed synchronization algorithms offers a pathway toward sensorless coordination of micro-generation units.

Recent work by Rincón-Silva et al. [6] explored a low-cost embedded architecture for PMSG micro-generator synchronization based on the Kuramoto model, demonstrating the relevance of oscillator-based coordination strategies for practical micro-generation applications. Building on this application context, the present study focuses on the convergence and stability properties of a mean-field synchronization architecture incorporating local state estimation and adaptive coupling. Particular attention is given to the relationship between frequency convergence, phase cohesion, and transient behavior, as well as to the computational implications of replacing explicit pairwise interactions with a collective order parameter.

Accordingly, this work presents a framework for decentralized synchronization in PMSG micro-generator networks. The proposed architecture combines SRF-dqPLL state estimation, mean-field Kuramoto coupling, and an adaptive-gain control law. Its convergence properties are examined through closed-loop stability analysis and continuous-time simulations of a four-node digital twin under heterogeneous initial frequencies. The main contribution is the integrated assessment of synchronization dynamics, phase-cohesive consensus, and computational scalability within a common control framework. The remainder of the paper presents the mathematical formulation and control methodology in Section 2, the numerical results in Section 3, their interpretation and comparison with previous studies in Section 4, and the main conclusions in Section 5.

2 Methodology

2.1 Analytical Dynamics of the Network Nodes

The proposed micro-generation network consists of N interconnected nodes, each representing an individual Permanent Magnet Synchronous Generator (PMSG) equipped with a local phase and frequency estimation unit and an adaptive synchronization controller. In this study, a four-node configuration ($N = 4$) is considered, where each generator operates under different initial frequency conditions. As illustrated in Fig.1, the SRF-dqPLL estimates the electrical phase and frequency of each generator from local voltage measurements, while the estimated states are exchanged through a shared communication medium. This information allows each node to independently compute the mean-field reference and adjust its dynamics through the adaptive control law, without requiring a centralized controller.

The proposed architecture employs a reduced-order analytical model for the electromechanical dynamics of a PMSG. Assuming a uniform air gap and neglecting magnetic saturation, Faraday's law dictates that the induced voltages (v_a, v_b, v_c) at the stator terminals are equal to the time variation of the stator magnetic flux linkage. Consequently, the induced voltage amplitude is directly proportional to the permanent-magnet flux linkage amplitude λ_m and to the electrical angular velocity $\omega_i(t)$ [5, 7]. The continuous-time voltage dynamics for phase a are defined by Eq. (1):

$$v_{a,i}(t) = \omega_i(t)\lambda_m \sin(\theta_i(t)) \tag{1}$$

where $\theta_i(t) = \int_0^t \omega_i(\tau)d\tau$ represents the instantaneous electrical angular position. To ensure dimensional consistency in Eq. (1), where $\omega_i(t)$ is expressed in rad/s and $v_{a,i}(t)$ in V, a permanent-magnet flux linkage constant of $\lambda_m = 0.0876$ Wb is established for the digital-twin parameterization, which proportionally determines the amplitude of the generated voltages as a function of the angular velocity of each node.

Figure 2 presents the electromechanical and single-line representation of the i-th PMSG unit (Node i), defining the physical and electrical framework of the multi-generator network. The mechanical subsystem represents the rotor dynamics described by Eq.14, where the prime mover supplies the mechanical torque $T_m(t)$, counteracted by the electromagnetic torque $T_e(t)$ acting on a shaft characterized by inertia J, damping D, speed $\omega_m(t)$, and position

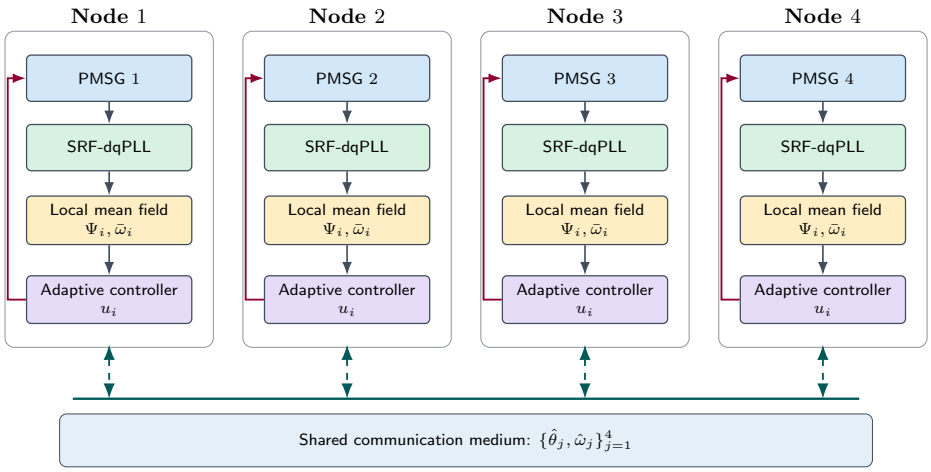


Figure 1: General architecture of the proposed four-node PMSG micro-generation network, illustrating local state estimation, adaptive synchronization control, and information exchange for decentralized mean-field coupling.

$\theta_m(t)$. On the electrical side, the PMSG is represented by a three-phase single-line model, connected in series with the stator resistance R_s and inductance L_s. The terminal voltages $v_{abc,i}(t)$, measured before the grid-connection switch, are fed to the Local Controller & State Estimator. Within this block, the SRF-dqPLL and adaptive controller estimate the electrical frequency $\hat{\omega}_i(t)$ and phase angle $\hat{\theta}_i(t)$.

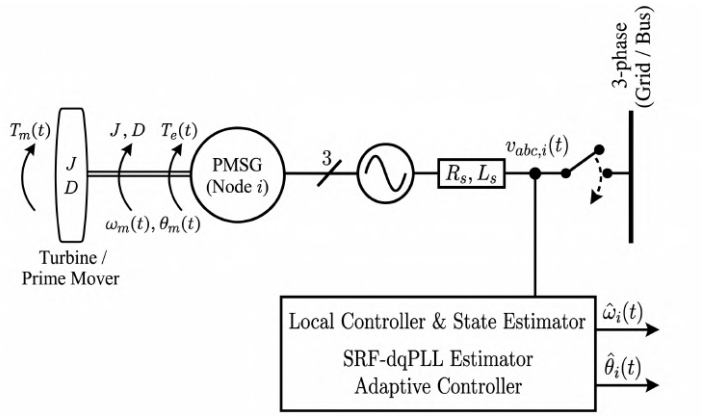


Figure 2: Electromechanical circuit model of the i-th PMSG node connected to the grid, including the local controller and state estimator.

2.2 State Estimation (SRF-dqPLL) in Continuous Time

To operate under a decentralized scheme without mechanical sensors, each node must estimate its instantaneous frequency and phase exclusively from voltage measurements. Throughout this manuscript, the accent ($\hat{}$) is employed to denote state variables that are estimated or reconstructed by the control algorithm, thereby distinguishing them from the actual physical states of the system.

For the network to operate under a decentralized scheme and, in practice, without mechanical sensors, each node must estimate its instantaneous frequency and phase exclusively from voltage measurements. The implemented algorithm is a Synchronous Reference Frame Phase-Locked Loop (SRF-dqPLL) [6]. The continuous three-phase signals (v_a, v_b, v_c) are first projected onto a stationary orthogonal $(\alpha\beta)$ frame through the Clarke transformation, incorporating a scaling factor of $2/3$ to guarantee amplitude invariance, and are subsequently projected onto a rotating (dq) frame through the Park transformation [5], as expressed in Eq. (2):

$$\begin{bmatrix} v_d(t) \\ v_q(t) \end{bmatrix} = \begin{bmatrix} \cos(\hat{\theta}_i(t)) & \sin(\hat{\theta}_i(t)) \\ -\sin(\hat{\theta}_i(t)) & \cos(\hat{\theta}_i(t)) \end{bmatrix} \begin{bmatrix} v_\alpha(t) \\ v_\beta(t) \end{bmatrix} \tag{2}$$

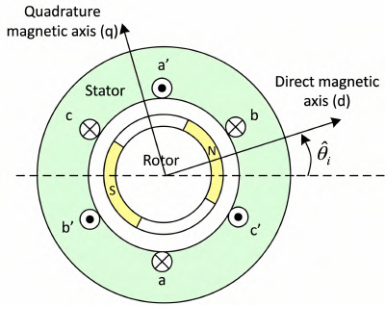


Figure 3: Cross-section of the Permanent Magnet Synchronous Machine (PMSG) illustrating the direct (d) and quadrature (q) rotating reference frames [8].

As illustrated in the phasor diagram of Fig.3, the d (direct) and q (quadrature) axes constitute a rotating reference frame synchronous with the estimated electrical position $\hat{\theta}_i(t)$. The objective of the control loop is to align the system's voltage vector strictly with the direct axis (d-axis). By doing so, the feedback loop forces the orthogonal quadrature component, $v_q(t)$, to approach zero. For small angular deviations between the actual physical phase and the estimated phase, the linearization $v_q(t) \approx V_m(\theta_i(t) - \hat{\theta}_i(t))$ is assumed, where V_m denotes the nominal peak amplitude of the phase voltage. The estimated electrical frequency $\hat{\omega}_i(t)$ is obtained by processing the error $v_q(t)$ through a continuous Proportional-Integral (PI) controller, as expressed in Eq. (3):

$$\hat{\omega}_i(t) = \omega_{nom} + K_p v_q(t) + K_i \int_0^t v_q(\tau)\, d\tau \tag{3}$$

where ω_{nom} represents the nominal angular frequency of the network, and K_p and K_i are the proportional and integral gains of the tracking loop, respectively. Finally, a virtual Voltage-Controlled Oscillator (VCO) integrates this frequency to obtain the instantaneous estimated phase $\hat{\theta}_i(t)$, thereby closing the feedback loop.

The signal flow described above, from the projection of the measured three-phase voltages to phase estimation through the PI controller and the VCO, is summarized in Fig. 4. This scheme illustrates the feedback of the estimated phase $\hat{\theta}_i(t)$ to the Park transformation, which is essential to guarantee that the error $v_q(t)$ approaches zero.

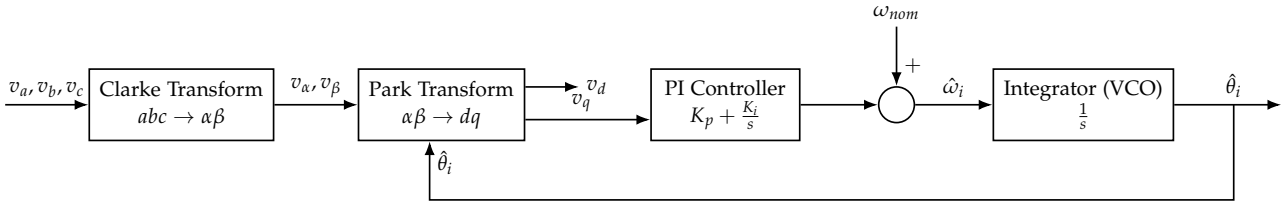


Figure 4: Block diagram of the Synchronous Reference Frame Phase-Locked Loop (SRF-dqPLL).

2.3 Mean-Field Coupling

In the classical Kuramoto model, the computational effort required to synchronize the network grows quadratically because it depends on the sum of pairwise angular differences $\sum \sin(\theta_j - \theta_i)$. To mitigate this algorithmic burden, the model is reformulated using mean-field coupling [9].

The system summarizes the network state through a complex order parameter $Z(t)$, given in Eq. (4), which represents the centroid of a set of M active micro-generators [1], :

$$Z(t) = R(t)e^{i\Psi(t)} = \frac{1}{M}\sum_{j=1}^{M} e^{i\hat{\theta}_j(t)} \tag{4}$$

The parameter $R(t)$ denotes the network coherence ($0 \leq R \leq 1$), serving as a metric of convergence. The phase of the network centroid, $\Psi(t)$, is defined by Eq. (5):

$$\Psi(t) = \text{atan2}\left(\sum_{j=1}^{M}\sin(\hat{\theta}_j(t)), \sum_{j=1}^{M}\cos(\hat{\theta}_j(t))\right) \tag{5}$$

In Eq. (5), although the atan2 function restricts the centroid phase $\Psi(t)$ to the principal interval $[-\pi, \pi]$ rad, the locally estimated phases $\hat{\theta}_j(t)$ can grow continuously beyond these bounds as time progresses. Because these local angles are evaluated through periodic sine and cosine functions, any phase value falling outside $[-\pi, \pi]$ is naturally mapped without loss of information. Furthermore, computing an unwrapped phase is unnecessary because the subsequent synchronization control law also evaluates the phase difference through a sinusoidal function. Owing to the 2π-periodicity of the sine operator, the periodic resets of $\Psi(t)$ at the $\pm\pi$ boundaries do not introduce discontinuities into the control signal, and operating directly with bounded phases prevents numerical overflow during long-term operation.

Through this transformation, the individual control error $e_{\theta,i}(t)$ of each node is decoupled from individual pairwise interactions and is defined solely by its distance from the unified centroid given in Eq. (6):

$$e_{\theta,i}(t) = \Psi(t) - \hat{\theta}_i(t) \tag{6}$$

This topological abstraction is illustrated in Fig.5. Panel (a) represents the pairwise model, in which computing the synchronization forces requires evaluating each individual link, resulting in quadratic growth $\mathcal{O}(N^2)$. In contrast, panel (b) demonstrates the efficiency of the mean-field architecture: by directing the attraction toward the global parameter Ψ, the interaction becomes linear, $\mathcal{O}(N)$, eliminating bottlenecks and freeing computational resources for continuous control of the micro-generators.

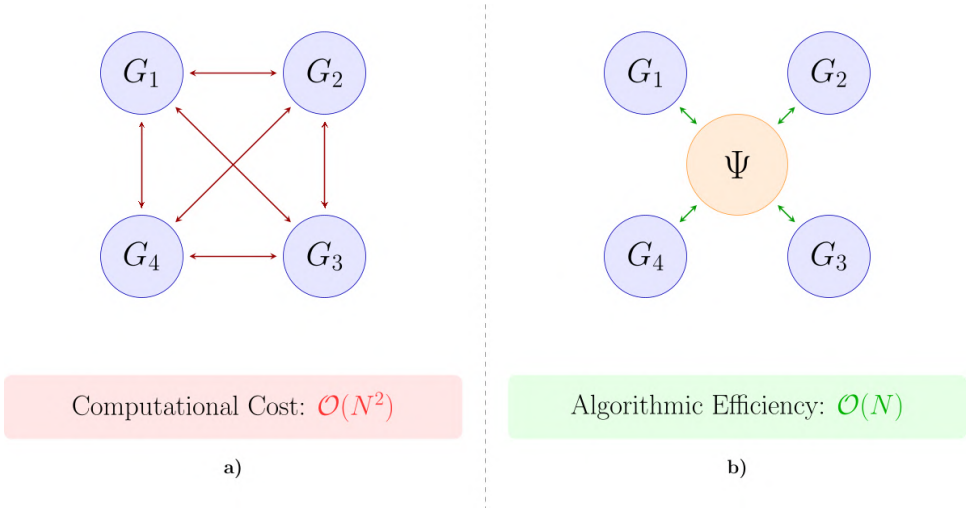


Figure 5: Algorithmic comparison: (a) pairwise interaction, $\mathcal{O}(N^2)$, versus (b) the proposed mean-field coupling, $\mathcal{O}(N)$.

To clarify the operational efficiency and scalability of the proposed decentralized mean-field architecture, it is necessary to distinguish between communication and computational complexities. To avoid relying on a centralized master controller, the architecture assumes a shared local communication medium. Under this scheme, each active node independently transmits its locally estimated phase $\hat{\theta}_i(t)$ exclusively once per synchronization cycle, yielding a linear network-wide communication overhead of $\mathcal{O}(N)$ messages. From a computational perspective, each local node reads the common bus and independently aggregates the M active states to calculate the centroid $\Psi(t)$ using Eq. (5). Consequently, the individual computational burden associated with this arithmetic aggregation scales as $\mathcal{O}(N)$ additions per node. Since the N nodes each perform $\mathcal{O}(N)$ arithmetic additions to estimate the centroid, the total arithmetic complexity across the network scales as $\mathcal{O}(N^2)$. However, the primary advantage of the proposed mean-field formulation lies in the execution of transcendental non-linear operations. Unlike classical pairwise Kuramoto formulations, which require the explicit evaluation of $N(N-1)$ non-linear sine functions and therefore exhibit a global non-linear computational bottleneck of $\mathcal{O}(N^2)$, the mean-field approach evaluates trigonometric interactions linearly. Specifically, each node computes only a single trigonometric deviation with respect to the centroid, $\sin(\Psi - \hat{\theta}_i)$, within the control law. As a result, the total network complexity associated with computationally expensive non-linear operations is reduced to $\mathcal{O}(N)$. This distinction minimizes processing bottlenecks and makes the architecture highly advantageous for resource-constrained embedded applications.

2.4 Adaptive Control Law and Phase-Cohesive Consensus

The synchronization dynamics require the micro-generators to adjust their frequencies in order to reach network consensus. Unlike classical formulations that employ a constant coupling strength, this architecture proposes a control law with an adaptive gain $K_{KUR,i}(t)$ driven by the frequency error relative to the mean field.

First, the instantaneous average of the estimated network frequencies, $\bar{\omega}(t)$, is calculated. The frequency error of each node relative to this average is processed through a saturated Proportional-Integral (PI) controller, defining the dynamic coupling strength, as defined in Eq. (7):

$$K_{KUR,i}(t) = \text{sat}\left(K_p|\bar{\omega}(t) - \hat{\omega}_i(t)| + K_i \int |\bar{\omega}(\tau) - \hat{\omega}_i(\tau)|\, d\tau\right) \tag{7}$$

This dynamic gain multiplies the nonlinear phase error, generating the final correction signal, as expressed in Eq. (8):

$$u_i(t) = K_{KUR,i}(t) \sin(\Psi(t) - \hat{\theta}_i(t)) \tag{8}$$

The implementation of this adaptive scheme guarantees smooth asymptotic convergence. Because it depends on the integral of the frequency error, the gain acts as a soft-start mechanism.

To show that convergence of the local phase error implies consensus ($R(t) \to 1$), the local phase is written as $\hat{\theta}_i(t) = \Psi(t) - e_{\theta,i}(t)$ and substituted into the definition of the order parameter, yielding Eq. (9):

$$R(t)e^{i\Psi(t)} = e^{i\Psi(t)}\left(\frac{1}{M}\sum_{j=1}^{M} e^{-ie_{\theta,j}(t)}\right) \tag{9}$$

Factoring out the term $e^{i\Psi(t)}$ isolates the scalar magnitude $R(t)$, which represents network coherence given in Eq. (10):

$$R(t) = \left(\frac{1}{M}\sum_{j=1}^{M} e^{-ie_{\theta,j}(t)}\right) \tag{10}$$

Applying Euler's identity to expand the complex exponential, the equation can be decomposed into its real and imaginary components using Eq. (11):

$$R(t) = \frac{1}{M}\sum_{j=1}^{M} \cos(e_{\theta,j}(t)) - i\frac{1}{M}\sum_{j=1}^{M} \sin(e_{\theta,j}(t)) \tag{11}$$

The imaginary component vanishes because $R(t)$ is defined as a real scalar magnitude. Therefore, the magnitude of the network coherence reduces to the sum of its real components, as shown in Eq. (12):

$$R(t) = \frac{1}{M}\sum_{j=1}^{M} \cos(e_{\theta,j}(t)) \tag{12}$$

This equation analytically demonstrates the main objective of the adaptive-gain control law. When the tracking algorithm acts and the system reaches steady state, the phase error at each individual node is driven toward zero ($e_{\theta,i}(t) \to 0$).

Under this condition, the trigonometric limit satisfies $\lim_{e_{\theta,j}\to 0} \cos(e_{\theta,j}(t)) = 1$. Substituting this value yields the final state of the system observed in Eq. (13):

$$R(t) \to \frac{1}{M}\sum_{j=1}^{M}(1) = \frac{M}{M} = 1 \tag{13}$$

This derivation shows that eliminating the local angular deviations through the controller is a sufficient condition for achieving electromagnetic coherence of the network and, consequently, a state of phase consensus.

While the proposed adaptive gain control law drives the phase error to zero ($e_{\theta,i}(t) \to 0$), it is necessary to clarify the range of attraction for this consensus. Due to the 2π periodicity of the sinusoidal coupling function (Eq. (8)), the dynamical system evolves in such a way that the phases of the oscillators can be separated by exactly π radians. Consequently, the synchronization achieved is not strictly global for all arbitrary initial conditions over $(-\pi, \pi]$. Instead, the consensus is formally restricted to a cohesive phase region, defined by a maximum initial phase spread strictly less than π radians ($\max|\hat{\theta}_i(0) - \hat{\theta}_j(0)| < \pi$).

2.5 Rotor-Dynamics Modeling and Closed-Loop Stability

The rotational dynamics of each PMSG rotor are governed by Newton's second law for rotation, which balances the inertial acceleration and viscous rotational damping against the net torque acting on the shaft [10]:, as expressed in Eq. (14)

$$J\frac{d^2\theta_m(t)}{dt^2} + D\frac{d\theta_m(t)}{dt} = T_m(t) - T_e(t) \tag{14}$$

where J is the total moment of inertia of the generator rotor, D denotes the viscous friction, $\theta_m(t)$ and $\frac{d\theta_m(t)}{dt}$ represent the mechanical angular position and mechanical angular velocity , respectively, $T_m(t)$ is the mechanical driving torque, and $T_e(t)$ is the opposing electromagnetic torque.

Applying the Laplace transform, we obtain the Eq. (15):

$$(Js + D)\Omega(s) = T_m(s) - T_e(s) \tag{15}$$

and therefore the transfer function between the torque difference and angular velocity is given in Eq. (16):

$$\frac{\Omega(s)}{T_m(s) - T_e(s)} = \frac{1}{Js + D} \tag{16}$$

This result shows how the inclusion of the damping term D transforms the original differential equation into a more stable first-order model consistent with the dynamics observed in real electrical systems.

If the synchronization dynamics of a generator are modeled as a first-order system with inertia (J) and natural damping (D), its transfer function $G(s)$ is given by Eq. 16.

The Proportional-Integral (PI) controller in the Laplace domain [11] as expressed in Eq. (17):

$$C(s) = K_p + \frac{K_i}{s} = \frac{K_p s + K_i}{s} \tag{17}$$

The closed-loop stability condition is obtained by setting the denominator of the overall transfer function equal to zero [11], using Eq. (18):

$$1 + C(s)G(s) = 0 \tag{18}$$

Substituting $C(s)$ and $G(s)$ gives the Eq. (19):

$$1 + \left(\frac{K_p s + K_i}{s}\right)\left(\frac{1}{Js + D}\right) = 0 \tag{19}$$

Multiplying by $s(Js + D)$ to eliminate the denominators and collecting terms yields Eq. (20):

$$Js^2 + (D + K_p)s + K_i = 0 \tag{20}$$

This quadratic polynomial constitutes the characteristic equation of the closed-loop system and shows how the PI controller modifies the coefficients associated with inertia, damping, and integral gain.

The Proportional-Integral controller for the adaptive gain was tuned through an analysis of the transient behavior. To validate the closed-loop stability of the system, the characteristic equation is analyzed using the Routh-Hurwitz stability criterion [11]. By constructing the Routh array for the polynomial $Js^2 + (D + K_p)s + K_i = 0$, the terms in the first column result in J for the s^2 row, $(D + K_p)$ for the s^1 row, and K_i for the s^0 row. The criterion establishes that stability is guaranteed if there are no sign changes in this first column. Given that the physical parameters of rotor inertia (J) and damping (D) are intrinsically positive constants, the controller design with strictly positive PI gains ($K_p > 0, K_i > 0$) ensures that $J > 0$, $D + K_p > 0$, and $K_i > 0$. Consequently, with no sign changes present, no root of the characteristic equation lies in the right half of the complex s-plane, confirming the stability of the system.

Furthermore, to theoretically validate the transient response dynamics, the denominator of the closed-loop transfer function is equated to the standard normalized second-order form: $s^2 + 2\zeta\omega_n s + \omega_n^2 = 0$ [11]. By dividing the characteristic equation (Eq. (20)) by J, the natural frequency of the system is analytically defined as $\omega_n = \sqrt{K_i/J}$, and the damping ratio as $\zeta = (D + K_p)/(2\sqrt{JK_i})$. As demonstrated by the unit-step response curves for second-order systems, damping ratios less than unity ($\zeta < 1$) induce an underdamped behavior characterized by overshoots and oscillations [11]. Therefore, to prevent destructive circulating currents caused by such oscillations in the stators, it is imperative to impose a critically damped ($\zeta = 1.0$) or overdamped response. To achieve this, the proportional gain

must satisfy the theoretical boundary condition: $K_p \geq 2\sqrt{JK_i} - D$. The selected parameters ($K_p = 0.035, K_i = 0.02$) were tuned to intrinsically satisfy this analytical constraint against the nominal parameters of the micro-generators, thereby guaranteeing the smooth, oscillation-free exponential convergence observed in the simulation results.

Likewise, the output of this controller is bounded by a saturation block that acts as a physical limiter, preventing excessive control effort during the maximum divergence of the initial transient regime.

To guarantee the nonlinear stability of the closed-loop mean-field synchronization, a Lyapunov-based analysis is applied. Following literature on phase-coupled oscillator networks and the Kuramoto potential [12], we define a continuous, positive-definite Lyapunov candidate function $V(\boldsymbol{\theta})$ representing the cohesion energy of the network's phase errors. Let $e_{\theta,i} = \Psi - \hat{\theta}_i$ be the local phase error. The potential function is defined by Eq. (21):

$$V = \sum_{i=1}^{M} (1 - \cos(e_{\theta,i})) \tag{21}$$

This function satisfies $V > 0$ for $e_{\theta,i} \in (-\pi, \pi)$ excluding the origin, and equals zero at the consensus state ($e_{\theta,i} = 0$). Taking the time derivative yields the exact gradient-descent dynamics of the network, as expressed in Eq. (22):

$$\dot{V} = \sum_{i=1}^{M} \sin(e_{\theta,i}) \dot{e}_{\theta,i} \tag{22}$$

To evaluate Eq. (22), the system is analyzed within a synchronous reference frame rotating at the centroid's velocity ($\omega_{sync} = \Psi$). In this frame, the centroid is stationary ($\Psi_{sync} = 0$), simplifying the error dynamics to $\dot{e}_{\theta,i} = -\dot{\hat{\theta}}_{i,sync}$. Furthermore, assuming a timescale separation where the inner mechanical dynamics are heavily damped, the phase kinematics are directly governed by the control effort from Eq. (8), yielding $\dot{\hat{\theta}}_{i,sync} \approx u_i(t) = K_{KUR,i}(t) \sin(e_{\theta,i})$. Substituting the resulting relationship, $\dot{e}_{\theta,i} = -K_{KUR,i}(t) \sin(e_{\theta,i})$, into Eq. (22) directly yields Eq. (23):

$$\dot{V} = -\sum_{i=1}^{M} K_{KUR,i}(t) \sin^2(e_{\theta,i}) \tag{23}$$

Since the adaptive PI controller guarantees positive dynamic gain ($K_{KUR,i}(t) > 0$), it follows from Eq. (23) that $\dot{V} \leq 0$. While this establishes Lyapunov stability, it does not strictly guarantee asymptotic convergence because $\dot{V}$ is negative semi-definite. To prove asymptotic convergence, LaSalle's Invariance Principle is applied [13]. According to this principle, the system trajectories converge to the largest invariant set contained within the region where $\dot{V} = 0$. From Eq. (23), the condition $\dot{V} = 0$ requires $\sin(e_{\theta,i}) = 0$ for all nodes. Because the network operates within the phase-cohesive region $e_{\theta,i} \in (-\pi, \pi)$, the unique valid solution within this domain is the consensus origin $e_{\theta,i} = 0$. Thus, LaSalle's principle formally guarantees that the micro-generators asymptotically converge to the synchronized state. To numerically corroborate this theoretical stability. As illustrated in Fig. 6, prior to synchronization ($t < 1$ s), the network exhibits high, oscillatory potential energy due to decoupled frequencies. Upon activation of the mean-field control law, the energy dissipates ($\dot{V} \leq 0$) and converges to zero. This real-time transient behavior validates the analytical proof, confirming that the adaptive gain strategy drives the multi-generator system toward a stable, cohesive phase consensus.

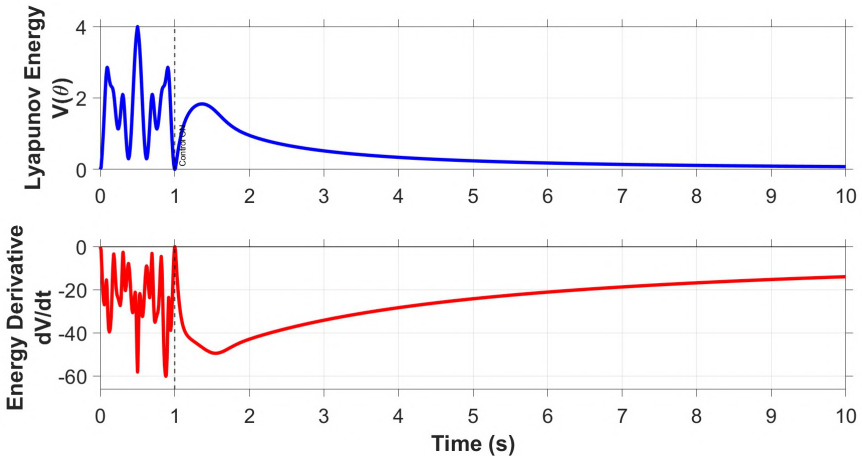


Figure 6: Lyapunov stability analysis. The top panel displays the evolution of the potential energy $V(\theta)$ converging to zero, while the bottom panel confirms that the energy derivative $\dot{V}$ remains negative ($\dot{V} \leq 0$) after the control activation at $t = 1$ s.

2.6 Digital-Twin Configuration and Simulation Conditions

To evaluate the performance of the proposed architecture, the network was implemented in the Simulink environment using a topology composed of $N = 4$ PMSG micro-generator nodes. To test system robustness under initial mismatches, heterogeneous natural oscillation frequencies were assigned to the generators: $f_1 = 17$ Hz, $f_2 = 25$ Hz, $f_3 = 20$ Hz, and $f_4 = 22$ Hz.

The simulation is divided into two temporal stages using a step function. During the first second ($0 \leq t < 1$ s), the network operates in open loop ($K_{KUR,i} = 0$), allowing each SRF-dqPLL algorithm to correctly estimate the natural phase and frequency of its respective node from voltage measurements. At $t = 1$ s, the mean-field control law is activated, closing the synchronization loop.

3 Results

To validate the proposed control architecture and evaluate the stability of mean-field consensus, a continuous digital twin of the system was developed on the Simulink platform. The simulations analyze the transient and steady-state response of a micro-generator network under initial frequency mismatches.

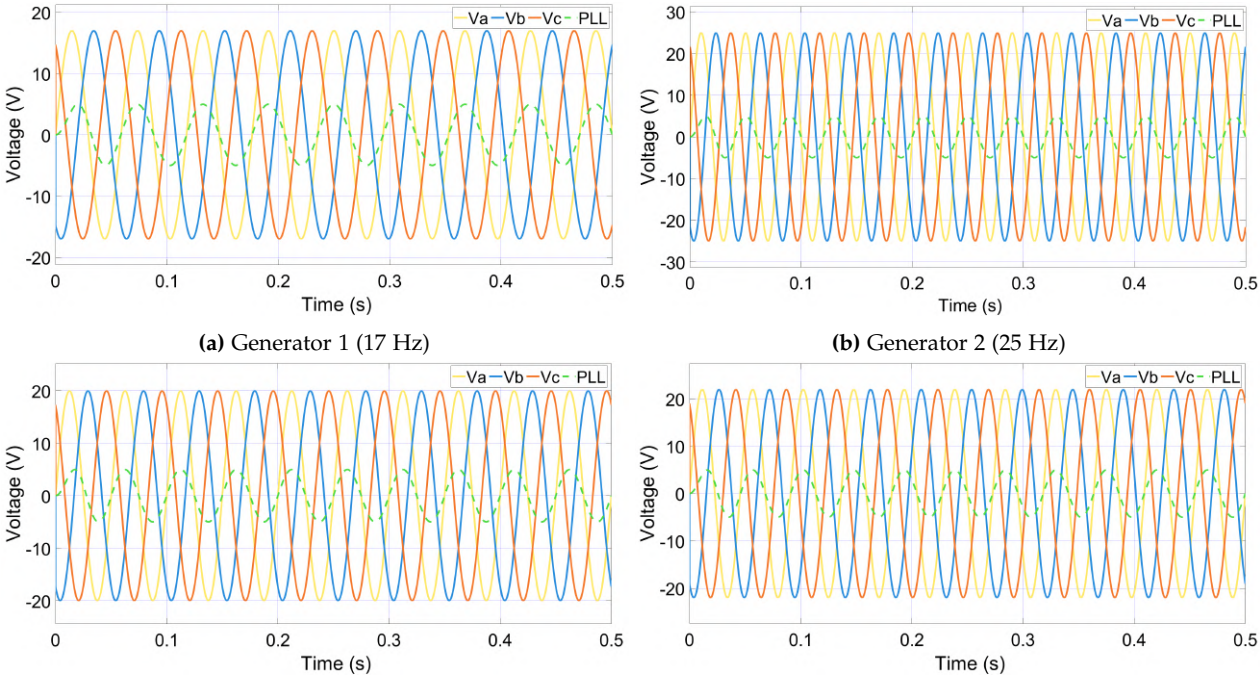
3.1 Validation of the State Estimator (SRF-dqPLL)

A fundamental prerequisite for the mean-field scheme is the correct extraction of the local phase and frequency at each node. During the open-loop interval, the ability of the continuous tracking loop to drive the quadrature error $v_q(t)$ to zero and lock onto the natural dynamics of each micro-generator was evaluated.

Fig.7 illustrates the standalone performance of the decentralized SRF-dqPLL estimator for each of the four nodes during the asynchronous startup phase. Two key behaviors validate the mathematical modeling. First, the peak amplitudes of the measured three-phase terminal voltages (solid lines) vary proportionally with their respective initial mechanical frequencies which strictly complies with the physical relationship established by the permanent-magnet flux linkage λ_m in Eq. (1). Second, the control effectiveness is visually confirmed by the dashed green line, which represents a normalized sinusoidal projection of the estimated phase $\hat{\theta}_i(t)$. Across all four subplots, the zero-crossings and peaks of this estimated signal perfectly align with the phase-a voltage (V_a). This superimposition demonstrates that the controller forces the quadrature component $v_q(t)$ to zero, achieving d-axis alignment for each node. The absence of a steady-state phase offset confirms that the SRF-dqPLL algorithm provides a stable angular reference $\hat{\theta}_i(t)$, which is required to compute the centroid $\Psi(t)$.

3.2 Frequency Convergence Analysis

Once the local measurements of each generator had been validated, the network response to activation of the coupling was evaluated. Fig. 8 presents the time evolution of the electrical frequencies of the four micro-generators.



(a) Generator 1 (17 Hz)

(b) Generator 2 (25 Hz)

(c) Generator 3 (20 Hz)

(d) Generator 4 (22 Hz)

Figure 7: Response of the SRF-dqPLL tracking loop during startup of the four nodes.

Before $t = 1$ s, the system exhibits a dispersed state due to the different natural angular velocities (ω_m). Once the loop is closed and the mean-field coupling is activated, the frequencies converge cooperatively toward a consensus value of approximately 21 Hz, demonstrating that the adaptive gain $K_{KUR,i}(t)$ mitigates the initial frequency divergence.

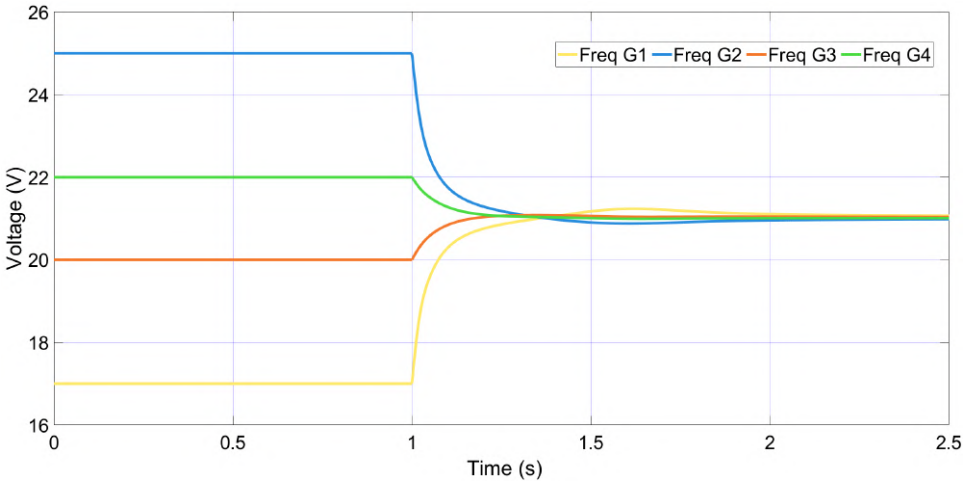


Figure 8: Convergence of the frequencies toward consensus through mean-field coupling.

3.3 Phase Synchronization and Network Consensus

In addition to frequency synchronization, phase consensus is necessary to enable electrical interconnection. Fig.9 shows the decay of the global phase error. After activation at $t = 1$ s, the error exhibits exponential decay without underdamped oscillations. By $t = 8$ s, the error is practically zero, ensuring that the coherence parameter reaches its maximum value.

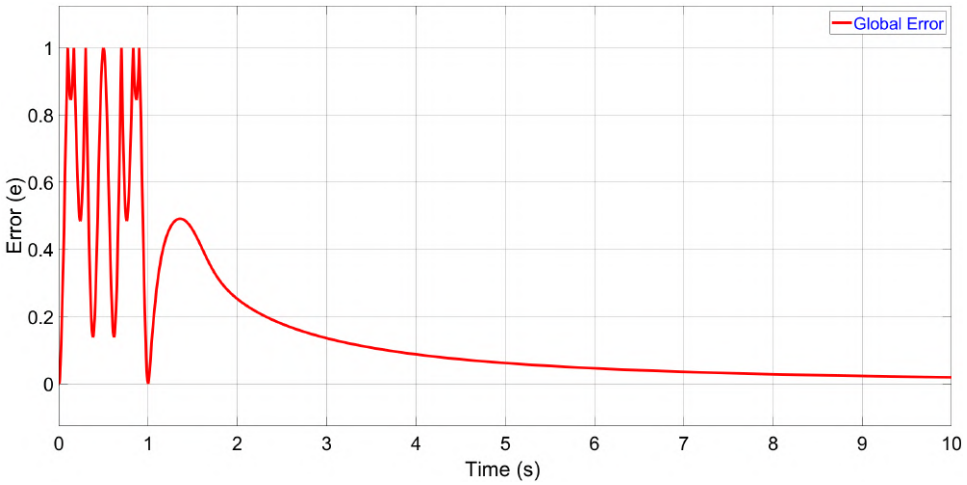


Figure 9: Time evolution of the global phase error.

The electromagnetic impact of this mathematical consensus becomes evident when the voltages of the four network nodes are compared. Fig. 10 shows the superimposed three-phase voltages before synchronization, illustrating an out-of-phase condition that would prevent interconnection to a common bus.

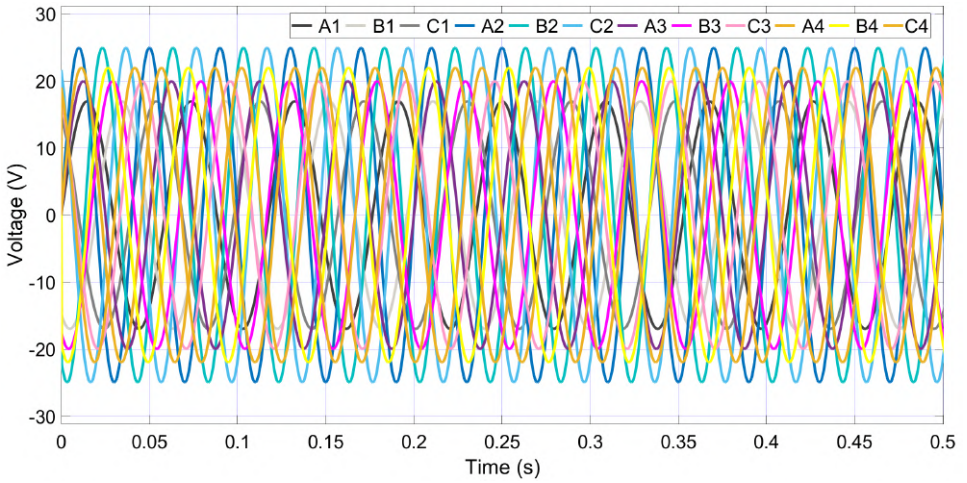


Figure 10: Network voltages in the dispersed state before synchronization.

In contrast, Fig.11 presents the system state after steady state has been reached. The mean-field centroid $\Psi(t)$ aligns the sinusoidal waveforms, resulting in a synchronized three-phase electrical system.

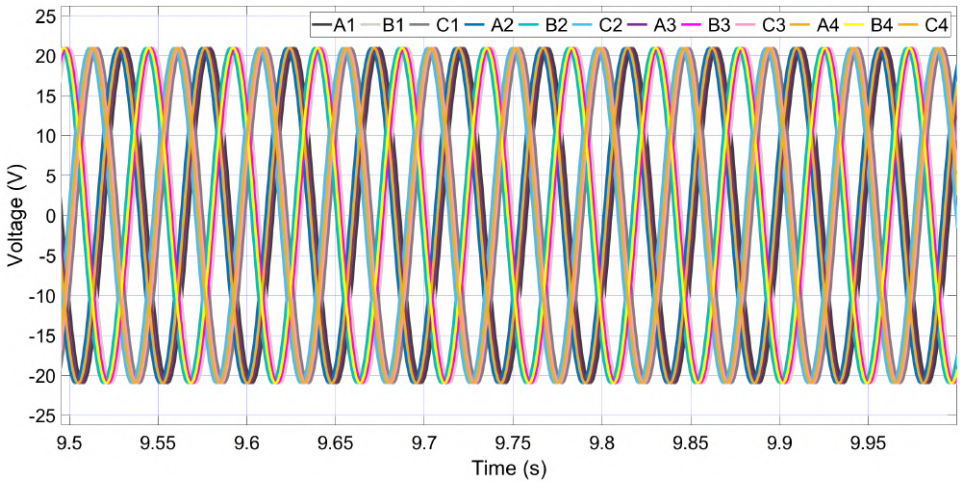


Figure 11: Consensus of the network three-phase voltages after the action of the mean-field controller.

4 Discussion

The numerical results demonstrate the effectiveness of the proposed mean-field coupling architecture in achieving frequency and phase synchronization among PMSG micro-generators with heterogeneous initial operating conditions. These findings are consistent with the theoretical framework of Benedetto et al. [1], who investigated complete phase synchronization in the mean-field limit of the Kuramoto model. While their analysis addresses the collective behavior of oscillator populations in the continuum limit, the present study examines a finite network of four micro-generators incorporating electromechanical dynamics, local state estimation, and adaptive control. The observed convergence toward a common frequency, followed by the progressive reduction of phase error, provides numerical evidence of synchronization under the operating conditions considered.

From an algorithmic perspective, the proposed formulation can be interpreted within the broader framework of Kuramoto synchronization in complex networks reviewed by Rodrigues et al. [4]. By expressing the coupling interaction through a common order parameter, the synchronization algorithm avoids the explicit evaluation of individual pairwise phase differences. For the all-to-all coupling formulation considered, this representation reduces the computational effort associated with evaluating the network interactions from $O(N^2)$ to $O(N)$. However, this reduction concerns the mathematical evaluation of the coupling terms and does not, by itself, establish equivalent improvements in communication latency or execution time on embedded hardware.

The present investigation also extends the application-oriented perspective of Rincón-Silva et al. [6], who addressed PMSG micro-generator synchronization using a low-cost embedded system based on the Kuramoto model. In contrast, the emphasis here is placed on the convergence properties of a mean-field formulation, including the relationship between phase cohesion, adaptive coupling, and closed-loop stability. The integration of SRF-dqPLL estimators enables each generator to obtain its phase and frequency information from local voltage measurements, while the shared mean-field reference coordinates the synchronization process. This distinction highlights the analytical contribution of the present work without implying that its numerical results constitute an experimental validation of the proposed architecture.

Regarding transient behavior, the adaptive-gain strategy produced a smooth convergence response without sustained oscillations in the simulated conditions. This observation is relevant to the stability concerns addressed by Ma and Shi [10], who investigated parameter-adaptive control for virtual synchronous generators under resistive-inductive grid-connected conditions. Although the two approaches involve different generator representations and control objectives, both emphasize the importance of transient stability in electrically coupled generation systems. In the present study, the gradual reduction of phase mismatch suggests favorable conditions for subsequent electrical interconnection; nevertheless, the suppression of circulating currents cannot be established without explicitly modeling and evaluating the corresponding electrical transients.

Despite these results, the analysis remains limited to a continuous-time digital twin of four PMSG units. Because the primary objective of this work is to establish the foundational continuous-time convergence of the mean-field architecture coupled with local SRF-dqPLL estimators, the present robustness evaluation focuses strictly on initial frequency mismatches. Consequently, the generator model neglects magnetic saturation, and the computation of the

mean-field centroid assumes reliable, instantaneous exchange of the estimated states among active nodes ($\tau = 0$). In practical implementations, measurement noise, communication delays, and inverter switching harmonics may affect the accuracy of the estimated phases and the resulting synchronization performance. However, a formal delay-robustness analysis lies beyond the scope of the present continuous-time study. Furthermore, although the mean-field formulation offers favorable computational scaling, its effectiveness in larger networks, under dynamic changes in network membership, and through systematic bounded-delay evaluations and hardware experiments remains to be established in future work.

5 Conclusions

This study presented analytical and numerical evaluations of a mean-field Kuramoto architecture for decentralized synchronization in PMSG micro-generation networks. The four-node digital-twin simulations demonstrated convergence from heterogeneous initial frequencies toward a common operating frequency, followed by a progressive reduction of phase error. These results support the proposed combination of local SRF-dqPLL estimation and adaptive-gain control within the phase-cohesive operating conditions considered.

The principal contribution lies in integrating a computationally efficient mean-field formulation with sensorless state estimation and adaptive synchronization control. Although the analytical (Routh-Hurwitz and Lyapunov) and numerical results establish the feasibility of the proposed approach within a phase-cohesive region under the simulated conditions, its performance in physical systems remains to be verified. Future work will therefore address embedded implementation and experimental assessment under measurement uncertainties, communication delays, and hardware-related disturbances.

Declarations

Conflicts of Interest: The authors declare that they have no known competing financial interests or personal relationships that could have appeared to influence the work reported in this paper.

Data Availability: The simulation models and data that support the findings of this study are available from the corresponding author upon request.

References

[1] Dario Benedetto, Emanuele Caglioti, and Umberto Montemagno. “On the Complete Phase Synchronization for the Kuramoto Model in the Mean-Field Limit”. In: *Communications in Mathematical Sciences* 13.7 (2015), pp. 1775–1786. DOI: 10.4310/CMS.2015.v13.n7.a6. URL: https://doi.org/10.4310/CMS.2015.v13.n7.a6.

[2] Alysha Helmrich et al. “Centralization and decentralization for resilient infrastructure and complexity”. In: *Environmental Research: Infrastructure and Sustainability* 1.2 (2021), p. 021001.

[3] Juan A Acebrón et al. “The Kuramoto model: A simple paradigm for synchronization phenomena”. In: *Reviews of modern physics* 77.1 (2005), pp. 137–185.

[4] Francisco A Rodrigues et al. “The Kuramoto model in complex networks”. In: *Physics Reports* 610 (2016), pp. 1–98.

[5] Z. Ali et al. “Three-phase phase-locked loop synchronization algorithms for grid-connected renewable energy systems: A review”. In: *Renewable and Sustainable Energy Reviews* 90 (2018), pp. 434–452.

[6] Adan Rincón-Silva et al. “Low-Cost Embedded System for PMSG Micro-Generator Synchronization Based on the Kuramoto Model”. In: *2026 12th International Conference on Control, Decision and Information Technologies (CoDIT)*. IEEE. Bari, Italy, 2026, pp. 2784–2789.

[7] José Omar Cuzco Alao and Jonnathan Ruben Lalvay Heras. “Modelado y simulación de un generador síncrono de imanes permanentes para un sistema de picogeneración hidroeléctrica”. Bachelor’s thesis. Universidad Politécnica Salesiana, Cuenca, Ecuador, 2022. URL: https://dspace.ups.edu.ec/handle/123456789/22922.

[8] MathWorks. *Synchronous reluctance machine with sinusoidal flux distribution*. MATLAB Help Center. Accessed on February 1, 2026. 2026. URL: https://la.mathworks.com/help/sps/ref/synchronousreluctancemachine.html.

[9] Giovanni Filatrella, Arne Hejde Nielsen, and Niels Falsig Pedersen. "Analysis of a power grid using a Kuramoto-like model". In: *The European Physical Journal B* 61.4 (2008), pp. 485–491. DOI: 10.1140/epjb/e2008-00098-8.

[10] Haoran Ma and Libao Shi. "Parameter-Adaptive Control Strategy for Stability Enhancement of Virtual Synchronous Generator Under Resistive-Inductive Grid-Connected Conditions". In: *Results in Engineering* (2026), p. 112687.

[11] Katsuhiko Ogata. *Ingeniería de control moderna [Modern control engineering]*. 5ta. Madrid, España: Pearson Educación, 2010.

[12] Dinuka Sahabandu et al. "Submodular Input Selection for Synchronization in Kuramoto Networks". In: *2020 59th IEEE Conference on Decision and Control (CDC)*. IEEE. 2020, pp. 5840–5847.

[13] Hassan K Khalil. *Nonlinear Systems*. 3rd. Upper Saddle River, NJ, USA: Prentice Hall, 2002.

Journal of Dynamical Systems and Complexity (2026) vol.1(3): 50-59
eISSN: 3122-4326, DOI: 10.66131/JDSC12202650-59

Physics-Informed Neural Network for Sparse-Sensor Inverse Heat Conduction

Cesar Ulises Solís Cervantes, Leonardo Gabriel Vega Macotela, Jorge de Jesús Morales Mercado *

Escuela Superior de Ingeniería Mecánica y Eléctrica, Instituto Politécnico Nacional, Mexico City.
Emails: csolisc@ipn.mx, lvegam@ipn.mx, jomoralesme@ipn.mx

Abstract

This study develops a sparse-sensor physics-informed neural network (PINN) to reconstruct a transient two-dimensional thermal field and identify thermal diffusivity, volumetric heat loss, and source amplitude from noisy point measurements. Sixteen interior sensors provide 5424 observations for a moving-source benchmark. The nominal model achieves a mean root-mean-square error (RMSE) of 3.52×10^{-3} *normalized temperature units and a global relative* L_2 *error of* 2.87×10^{-2}*. The corresponding relative errors in the three identified coefficients are 5.04%, 24.54%, and 7.90%. Under matched data, architecture, initialization, and iteration budget, the physics-informed model reduces mean RMSE by 96.03% relative to a conventional data-only neural network and by 95.56% relative to spatiotemporal interpolation. One-factor-at-a-time tests indicate that spatial sensor scarcity and loss weighting are more influential than temporal subsampling over the ranges examined. The results show that governing-equation constraints provide strong regularization for sparse thermal reconstruction; however, the sensitivity results are diagnostic rather than statistical, and experimental validation remains necessary before deployment.*

Keywords— Physics-informed neural network, Inverse heat conduction, Sparse sensors, Thermal field reconstruction, Parameter identification, Sensitivity analysis

1 Introduction

Inverse heat-conduction problems arise in thermal monitoring, digital twins, advanced manufacturing, electronics cooling, and energy systems. In these applications, complete internal temperature fields and effective material properties are seldom measured directly. Classical inverse workflows couple a numerical solver with explicit regularization and an outer optimization loop, but their computational cost and ill-conditioning grow when measurements are sparse, noisy, or confined to a small part of the domain. Scientific machine learning offers a complementary strategy in which observations and governing equations are incorporated into one trainable model [1, 2, 3, 4]. Related data-driven studies have also demonstrated neural-network-based system identification under complex dynamics and noisy observations, including approaches that incorporate probabilistic information to improve modeling accuracy [5].

A physics-informed neural network (PINN) is trained not only from data, but also by penalizing violations of a partial differential equation (PDE), its boundary conditions, and its initial condition [2]. This approach builds on residual and variational neural solvers such as the Deep Ritz method and the Deep Galerkin method (DGM) [6, 7]. Later work has addressed DeepXDE (deep learning for differential equations) and the Scientific Artificial Neural Networks (SciANN) interface [8, 9], gradient imbalance in composite objectives [10], adaptive activations [11], *hp*-variational physics-informed neural networks (*hp*-VPINNs), in which h and p denote subdomain scale and polynomial degree, for domain decomposition [12], Bayesian physics-informed neural networks (B-PINNs) [13], and deep operator networks (DeepONets) [14]. Together, these studies show that PINNs are flexible inverse solvers, while also identifying optimization, loss scaling, and uncertainty as persistent limitations [3, 15].

Thermal applications include direct heat-equation solutions, inverse coefficient or heat-flux estimation, manufacturing surrogates, and virtual thermal sensing [4, 16, 17, 18, 19, 20, 21]. Zobeiry and Humfeld studied one- and two-dimensional conduction models with physics-based feature engineering. Oommen and Srinivasan considered data-sparse inverse heat transfer without a conventional surrogate, while He *et al.* and Billah *et al.* examined direct and inverse conduction in materials. Go *et al.* developed a PINN-based virtual thermal sensor. More recent studies

*Corresponding author: jomoralesme@ipn.mx
Received: September 21, 2026, **Published:** October 31, 2026
Editor: Y. Lozano-Hernández

have investigated improved PINN formulations for transient nonlinear and inhomogeneous heat conduction [22], uncertainty quantification and enhanced formulations for inverse heat-conduction problems [23, 24], and transient thermal problems involving moving heat sources [25]. These studies establish the feasibility of physics-informed learning for inverse and transient thermal problems, but their domains, measurements, unknowns, and error normalizations differ. A direct ranking of their reported errors would therefore be misleading.

A controlled comparison on a single benchmark helps isolate the contribution of physics constraints. In particular, neural identification studies show that model architecture and probabilistic treatment can affect performance under noisy, complex data [5], while recent sequence-based neural models have used learned representations to identify nonlinear robotic systems from heterogeneous measurements [26]. These results motivate careful control of model capacity, available observations, and training conditions when assessing a physics-informed model. They also reinforce the importance of distinguishing improvements associated with the learning architecture from those attributable to the incorporation of physical knowledge.

Another distinction matters for inverse thermal problems: field reconstruction and parameter identification are not necessarily equivalent objectives. A model may reconstruct the temperature field accurately while still exhibiting comparatively large errors in one or more physical coefficients. This is particularly relevant for sparse-sensor problems, where different parameters can produce partially correlated effects on the thermal dynamics. The present study therefore evaluates field reconstruction and parameter recovery separately.

The present study focuses on a controlled sparse-sensor benchmark for transient two-dimensional inverse heat conduction. It reconstructs the thermal field while simultaneously identifying three positive physical coefficients from sixteen noisy interior sensors. The proposed PINN is compared with a data-only neural network using the same architecture and observations, as well as with noniterative spatiotemporal interpolation. The study also examines sensor count, temporal sampling, measurement noise, and individual loss weights through controlled sensitivity runs.

The comparison with existing literature is summarized in Table 1. These studies differ in their physical settings, estimated quantities, measurement configurations, and reported accuracy. Their error normalizations are not directly comparable, so a ranking of their reported errors would be misleading, and a controlled comparison on one benchmark is still needed to isolate the contribution of the physics constraints. The closest prior work, Bidou *et al.* [21], addresses two-dimensional transient inverse conduction with a Gaussian internal source and PINN-guided sensor placement, but treats orthotropic property identification and source identification as separate tasks. None of the cited studies simultaneously recovers the thermal diffusivity, a volumetric heat-loss coefficient, and the source amplitude in a two-dimensional transient problem with a composite moving and stationary source from a small set of noisy interior sensors. That combination is the focus of the present work, and the sparse-sensor setting is precisely where physics-informed constraints matter most: sixteen sensors cannot determine a 192×192 field from data alone, so the governing equation and the boundary and initial conditions must carry the spatial information that the measurements do not.

Table 1: Positioning of the present work with respect to recent physics-informed neural-network heat-conduction studies.

Study	Task and setting	Estimated unknowns	Sensors / data	Reported accuracy
Cai *et al.* [4]	Forward/inverse; 2-D convection, cylinder	Temperature, velocity, and pressure fields; boundary conditions; Nusselt number	As few as six sparse sensors	Relative L_2 temperature errors, 1.25–15.09%
Zobeiry and Humfeld [16]	Forward; 1-D and 2-D conduction, convective boundaries	Temperature field only	No sensor data	Agrees with finite-element results
Oommen and Srinivasan [17]	Inverse; four data-sparse heat-transfer cases	Unknowns of the four cases	Sparse measurements	Better than conventional machine learning
He *et al.* [18]	Forward/inverse; 1-D conduction, wood and steel	Constant material parameters	Measured data	High accuracy against exact solutions
Billah *et al.* [19]	Inverse; 1-D unsteady aluminum wall	Thermal diffusivity; boundary heat flux	Small interior observation subset	Robust to noisy observations
Go *et al.* [20]	Forward surrogate; plate of varying thickness	Real-time field surrogate	Transfer learning across scenarios	Agrees with finite-element results
Bidou *et al.* [21]	Inverse; 2-D transient plate, Gaussian source	Property tensor, or source amplitude, position, and dispersion (separate tasks)	Sensitivity-guided sensor set; noise up to 0.5 K	High accuracy, reported qualitatively
This work	Inverse; 2-D transient; moving plus stationary source; heat-loss term	Diffusivity, heat loss, and source amplitude simultaneously	16 random sensors; 5424 observations; 10^{-3} noise	$E_{L_2} = 2.87 \times 10^{-2}$; parameter errors 5.04, 24.54, and 7.90%

This study makes five contributions. First, it reconstructs a transient two-dimensional field while identifying three positive thermal coefficients from sixteen noisy interior sensors. Second, it compares the physics-informed model with a neural network of identical architecture but without physics-based losses, as well as with noniterative spatiotemporal interpolation. Third, it examines sensor count, temporal sampling, measurement noise, and every loss weight through controlled sensitivity runs. Fourth, it provides a workflow that details the hardware, accuracy, initialization, random seeds, number of parameters, batch sizes, and stopping rule (see the program available at the link at the end of this paper). Fifth, it situates the configuration against the closest published studies, including Bidou *et al.* [21], in Table 1. The analysis treats field reconstruction and parameter observability as distinct objectives and discusses the requirements for transfer to experimental measurements.

2 Physics-informed formulation

Let $x \in [0, L_x]$ and $y \in [0, L_y]$ denote the spatial coordinates, let $t \in [0, T]$ denote time, and let $u(x, y, t)$ be the temperature field. The rectangular spatial domain is $\Omega = (0, L_x) \times (0, L_y)$, its boundary is $\partial\Omega$, and T is the final time. A feedforward network $u_\theta(x, y, t)$ approximates u, where θ collects all trainable neural weights and biases. The unknown positive coefficients are the thermal diffusivity α, the linear heat-loss coefficient γ, and the source-amplitude coefficient β. The strong-form residual is

$$\mathcal{R}_\theta(x, y, t) = \frac{\partial u_\theta}{\partial t} - \alpha \left(\frac{\partial^2 u_\theta}{\partial x^2} + \frac{\partial^2 u_\theta}{\partial y^2} \right) + \gamma u_\theta - \beta S(x, y, t), \tag{1}$$

where $\mathcal{R}_\theta$ measures the local heat-balance error and $S(x, y, t)$ is the prescribed, dimensionless source shape.

Suppose that N_s scalar observations are recorded. The sensor data set is

$$\mathcal{D}_s = \{(x_m, y_m, t_m, \widetilde{u}_m)\}_{m=1}^{N_s}, \qquad \widetilde{u}_m = u(x_m, y_m, t_m) + \varepsilon_m, \quad \varepsilon_m \sim \mathcal{N}(0, \sigma_n^2). \tag{2}$$

Here, m indexes an observation; (x_m, y_m, t_m) is its space-time coordinate; $\widetilde{u}_m$ is the measured temperature; ε_m is zero-mean Gaussian noise; σ_n is its standard deviation; and $\mathcal{N}(0, \sigma_n^2)$ denotes a normal distribution with variance σ_n^2.

Training minimizes the composite objective

$$\mathcal{L} = w_d \mathcal{L}_{\text{data}} + w_f \mathcal{L}_{\text{PDE}} + w_b \mathcal{L}_{\text{BC}} + w_0 \mathcal{L}_{\text{IC}} + w_p \mathcal{L}_{\text{prior}}, \tag{3}$$

where $\mathcal{L}$ is the total loss and w_d, w_f, w_b, w_0, and w_p are nonnegative weights for the data, governing-equation, boundary-condition, initial-condition, and parameter-prior terms. The abbreviations PDE, BC, and IC denote partial differential equation, boundary condition, and initial condition, respectively. The component losses are

$$\mathcal{L}_{\text{data}} = \frac{1}{N_s} \sum_{m=1}^{N_s} |u_\theta(x_m, y_m, t_m) - \widetilde{u}_m|^2, \qquad \mathcal{L}_{\text{PDE}} = \frac{1}{N_f} \sum_{j=1}^{N_f} |\mathcal{R}_\theta(\boldsymbol{\xi}_j)|^2,$$
$$\mathcal{L}_{\text{BC}} = \frac{1}{N_b} \sum_{j=1}^{N_b} |u_\theta(\boldsymbol{\xi}_j^{(b)})|^2, \qquad \mathcal{L}_{\text{IC}} = \frac{1}{N_0} \sum_{j=1}^{N_0} |u_\theta(x_j^{(0)}, y_j^{(0)}, 0) - u_0(x_j^{(0)}, y_j^{(0)})|^2. \tag{4}$$

The index j enumerates training points. The points $\boldsymbol{\xi}_j = (x_j^{(f)}, y_j^{(f)}, t_j^{(f)})$ lie inside $\Omega \times (0, T]$, and $\boldsymbol{\xi}_j^{(b)} = (x_j^{(b)}, y_j^{(b)}, t_j^{(b)})$ lie on $\partial\Omega \times (0, T]$. The pair $(x_j^{(0)}, y_j^{(0)})$ is an initial-time spatial point, and $u_0(x, y)$ is the prescribed initial field. The superscripts f, b, and 0 label interior, boundary, and initial sets. Accordingly, N_f, N_b, and N_0 are the numbers of interior, boundary, and initial points in each training batch.

A weak logarithmic prior,

$$\mathcal{L}_{\text{prior}} = (\log \alpha - \log \alpha_0)^2 + (\log \gamma - \log \gamma_0)^2 + (\log \beta - \log \beta_0)^2, \tag{5}$$

conditions the early inverse search, where α_0, γ_0, and β_0 are the initial coefficient guesses and log is the natural logarithm. Positivity is enforced through $\alpha = e^{\eta_\alpha}$, $\gamma = e^{\eta_\gamma}$, and $\beta = e^{\eta_\beta}$; e is the natural exponential base, and η_α, η_γ, and η_β are unconstrained trainable scalars.

The nominal weight vector is $(w_d, w_f, w_b, w_0, w_p) = (50, 1, 10, 10, 10^{-4})$. The data term is scaled upward because its unweighted mean-square magnitude is small relative to the PDE residual. The boundary and initial terms receive larger weights to preserve the known constraints, whereas the prior remains deliberately weak. Section 4.3 perturbs

each weight separately rather than treating the nominal vector as universally optimal. The network has five hidden layers of width 128 and hyperbolic-tangent activations. Its input contains the normalized coordinates (x, y, t) and the sine and cosine of 48 Gaussian random Fourier projections, which help represent the moving localized source. The neural network has 78,977 trainable parameters; the three physical scalars increase the total to 78,980.

3 Thermal benchmark and numerical protocol

The benchmark uses normalized coordinates on the unit square $\Omega = (0,1)^2$ over the time interval $0 \le t \le T = 1$:

$$\frac{\partial u}{\partial t} = \alpha \nabla^2 u - \gamma u + \beta S(x,y,t), \qquad u|_{\partial\Omega} = 0, \qquad u(x,y,0) = 0. \tag{6}$$

Here, $\nabla^2 u = \partial^2 u/\partial x^2 + \partial^2 u/\partial y^2$ is the two-dimensional Laplacian. The superscript $\star$ identifies the exact coefficient used only to generate the synthetic reference data: $\alpha^\star = 0.017$, $\gamma^\star = 0.85$, and $\beta^\star = 7.5$. The source combines a moving pulsed Gaussian with a weaker stationary hot spot:

$$\begin{aligned} S(x,y,t) = {} & p(t) \exp\left[-\frac{(x - c_x(t))^2}{2\sigma_x^2} - \frac{(y - c_y(t))^2}{2\sigma_y^2} \right] \\ & + A_s p_s(t) \exp\left[-\frac{(x - x_s)^2 + (y - y_s)^2}{2\sigma_s^2} \right], \end{aligned} \tag{7}$$

$$c_x(t) = \tfrac{1}{2} + r_x \cos(2\pi n_r t + \phi), \qquad c_y(t) = \tfrac{1}{2} + r_y \sin(2\pi n_r t + \phi), \tag{8}$$

with $p(t) = 0.65 + 0.35\sin^2(2\pi n_p t)$ and $p_s(t) = 0.5 + 0.5\cos^2(2\pi n_s t)$. The pair (c_x, c_y) is the moving-source center; r_x and r_y are its orbit radii; n_r is the number of rotations; and ϕ is the phase. The quantities σ_x and σ_y are the main-source spreads. For the secondary source, A_s is the relative amplitude, (x_s, y_s) is the center, and σ_s is the spread. Finally, n_p and n_s control the two pulse modulations. The numerical values are $r_x = 0.25$, $r_y = 0.18$, $n_r = 1.35$, $\phi = 0.15\pi$, $\sigma_x = 0.055$, $\sigma_y = 0.045$, $A_s = 0.35$, $(x_s, y_s) = (0.27, 0.73)$, $\sigma_s = 0.085$, $n_p = 5$, and $n_s = 2$.

A five-point explicit finite-difference scheme generates the reference field on a 192×192 grid. The temporal grid is automatically increased from 1001 to 2698 points to satisfy the sufficient stability condition

$$\Delta t \le \frac{2 s_f}{\gamma^\star + 4\alpha^\star(\Delta x^{-2} + \Delta y^{-2})}, \qquad s_f = 0.92, \tag{9}$$

where Δx, Δy, and Δt are the uniform spatial and temporal steps, and s_f is a dimensionless safety factor. Sixteen interior sensor locations are drawn once with seed 17 and a 12% boundary margin. Every eighth stable time sample is retained, including $t = 1$, which gives 339 samples per sensor and $N_s = 5424$ observations. Gaussian noise with standard deviation $\sigma_n = 10^{-3} \max|u| = 7.47 \times 10^{-4}$ normalized temperature units (n.t.u.) is added with seed 1701.

The training is performed using the MATLAB numerical-computing environment, release R2026a Update 4, Deep Learning Toolbox 26.1, Parallel Computing Toolbox 26.1, single precision, and an NVIDIA GeForce RTX 4050 Laptop graphics processing unit (GPU) with 6 gigabytes (GB) of memory. The adaptive moment estimation (Adam) optimizer runs for a fixed budget of 7200 iterations with an initial learning rate of 2×10^{-3} and decay of 10^{-4}; early stopping is disabled. Weights are initialized with the Glorot-uniform distribution, with per-layer limit $\sqrt{6/(n_{\text{in}} + n_{\text{out}})}$, where n_{in} and n_{out} are the input and output unit counts, to preserve the scale of activations and gradients across the five tanh layers; biases are zero. The 48 Gaussian random Fourier projections use a fixed scale of 2.5. A fixed seed of 2701 makes the nominal comparison reproducible. The initial coefficient guesses $(\alpha_0, \gamma_0, \beta_0) = (0.008, 0.35, 3.5)$ are deliberately biased away from the true values so that the recovery in Table 2 reflects identifiability rather than a favorable starting point. Each iteration uses all 5424 observations and newly sampled batches of 4096 interior, 1024 boundary, and 1024 initial points. The nominal wall-clock training time is 241.46 s; it is reproducibility metadata only and is never used as a performance statistic.

The data-only neural network uses the same architecture, Fourier map, initialization seed, observations, and 7200-iteration budget, but it minimizes only the sensor mean-square error and does not identify physical parameters. The interpolation baseline first applies linear interpolation in time at each sensor and then natural-neighbor interpolation in space, with nearest-neighbor extrapolation where needed. Both baselines use exactly the same sensor data as the physics-informed model, so differences in field accuracy can be attributed to the physics constraints rather than to data availability.

For evaluation frame k, the root-mean-square error (RMSE) and mean absolute error (MAE) are

$$\mathrm{RMSE}_k = \left(\frac{1}{N_g} \sum_{i=1}^{N_g} (\widehat{u}_{i,k} - u_{i,k})^2 \right)^{1/2}, \qquad \mathrm{MAE}_k = \frac{1}{N_g} \sum_{i=1}^{N_g} |\widehat{u}_{i,k} - u_{i,k}|, \tag{10}$$

where i indexes a grid point, $N_g = 192^2$ is the number of grid points, $\widehat{u}_{i,k}$ is the predicted temperature, and $u_{i,k}$ is the reference temperature. Over $N_e = 12$ evaluation frames, the global relative error is

$$E_{L_2} = \left(\frac{\sum_{k=1}^{N_e} \|\widehat{\mathbf{u}}_k - \mathbf{u}_k\|_2^2}{\sum_{k=1}^{N_e} \|\mathbf{u}_k\|_2^2} \right)^{1/2}, \tag{11}$$

where $\widehat{\mathbf{u}}_k$ and $\mathbf{u}_k$ are the vectorized predicted and reference fields, and $\|\cdot\|_2$ is the Euclidean norm. The zero-energy initial frame is excluded only from framewise relative-error averages; Equation (11) remains well defined over all N_e frames.

4 Results

4.1 Nominal optimization, reconstruction, and parameter identification

Figure 1 summarizes the nominal optimization: the weighted data and PDE terms dominate the final objective, the total loss reaches 1.53×10^{-3} at iteration 7200, and the normalized trajectories show late-stage recovery of α and β, while γ remains below its reference value. Training stops at the fixed iteration budget, so these curves describe optimization behavior rather than an early-stopping criterion.

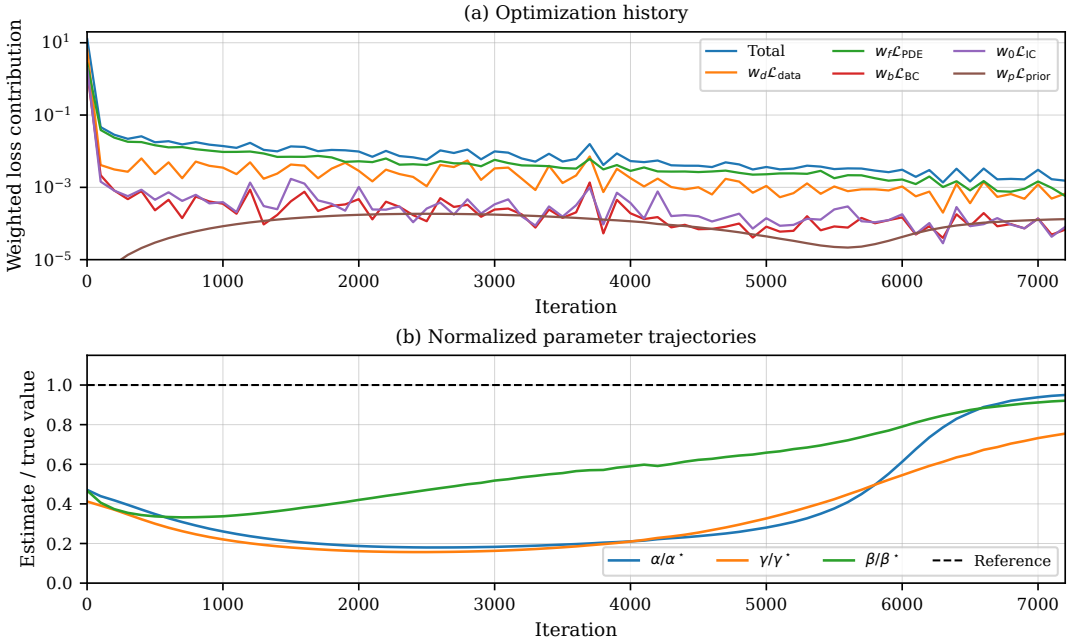


Figure 1: Nominal PINN training. (a) Total loss and weighted components. (b) Identified coefficients normalized by their true values. PDE, BC, and IC denote partial differential equation, boundary condition, and initial condition.

Across the 12 evaluation frames, the mean RMSE is 3.5175×10^{-3} n.t.u., the maximum RMSE is 4.4057×10^{-3} n.t.u., the mean MAE is 2.4203×10^{-3} n.t.u., and $E_{L_2} = 2.8689 \times 10^{-2}$. At $t = 1$, the RMSE is 2.5072×10^{-3} n.t.u. and the relative L_2 error is 1.3563×10^{-2}. As shown in Figure 2, the reconstruction preserves the dominant hot region, the secondary footprint, and the diffusion trail despite measurements from only sixteen locations; the largest discrepancies remain near steep source-induced gradients.

Table 2 shows relative errors below 8% for α and β, but 24.54% for γ. This difference is physically plausible: diffusivity and volumetric loss both affect temporal decay and spatial smoothing and are hard to separate with

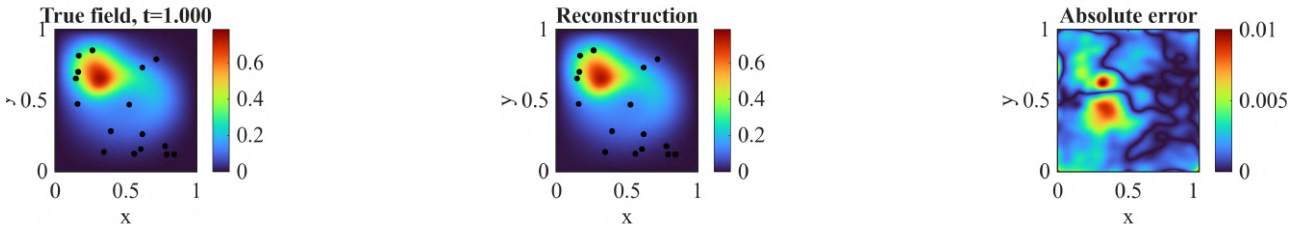


Figure 2: Final-time field at $t = 1$. Left: finite-difference reference; center: PINN reconstruction; right: absolute error. Black points indicate the sixteen sensor locations.

Table 2: Physical-parameter identification in the nominal run.

Parameter	True	Initial	Estimated	Relative error (%)
α	0.0170	0.0080	0.016144	5.036
γ	0.8500	0.3500	0.641444	24.536
β	7.5000	3.5000	6.907141	7.905

sparse sensors, whereas source amplitude is more directly related to peak temperature. Accurate field reconstruction and partial coefficient recovery therefore coexist, and state and parameter errors must be interpreted separately.

4.2 Controlled comparison with data-only reconstruction

Figure 3 and Table 3 provide the main controlled validation. The PINN reduces mean RMSE by 96.03% relative to the matched data-only neural network (NN) and by 95.56% relative to spatiotemporal interpolation. The corresponding reductions in E_{L_2} are 95.98% and 95.77%. At the final frame, the two data-only baselines have relative errors near 0.64, whereas the PINN gives 0.0136. The conventional NN has the same 78,977 neural parameters and the same initialization, so the accuracy gap cannot be explained by network size. Instead, it isolates the regularization provided by the PDE, boundary, and initial-condition terms. Only the PINN also estimates α, γ, and β. We acknowledge that the two iterative models are not symmetric in the information they use: the PINN receives the governing equation, the boundary condition, and the initial condition in addition to the sensor data, whereas the data-only network sees the sensor data alone. This asymmetry is the object of the comparison: it quantifies the value of the known physics for this benchmark. From sixteen scattered sensors a data-only network must extrapolate a 192-by-192 field from severely underdetermined information, and its error concentrates off-sensor (relative errors near 0.64 at the final frame), whereas the physics terms propagate information through the domain and, together with the sensor data, make both the field and the three parameters identifiable.

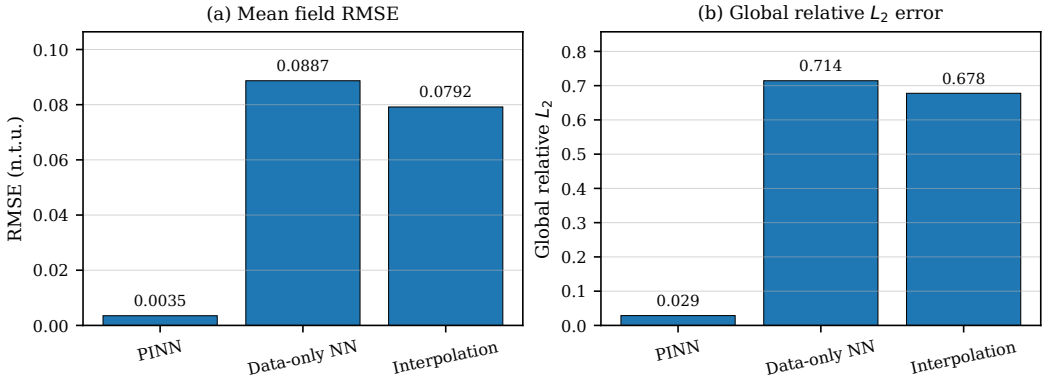


Figure 3: Controlled reconstruction comparison using the same sixteen sensors and 5424 noisy observations. Training time is intentionally excluded from the performance analysis.

This comparison is specific to one benchmark and is not a universal ranking: classical regularized optimization can be highly competitive when the forward model is reliable, and operator-learning surrogates may be preferable when many parameterized queries are available. The supported claim is narrower: for the present sparse moving-source problem, the physics constraints prevent the severe off-sensor degradation observed in the two data-only baselines.

Table 3: Reconstruction comparison on the common benchmark.

Method	Mean RMSE	Mean MAE	Global L_2	Final RMSE	Parameters
PINN	0.003518	0.002420	0.028689	0.002507	78,980
Data-only neural network	0.088679	0.060161	0.714344	0.117861	78,977
Spatiotemporal interpolation	0.079173	0.048275	0.677735	0.119443	0

4.3 Sensitivity and loss-weight analysis

The sensitivity campaign adds 21 PINN trainings: three sensor counts, three temporal strides, four noise levels, and eleven loss-weight configurations; Figure 4 summarizes these controlled perturbations. Every case uses seed 3701 and one run, so each comparison changes only the selected factor. These runs are diagnostic one-factor-at-a-time tests, not estimates of means, variances, or statistical significance, and wall-clock time is excluded.

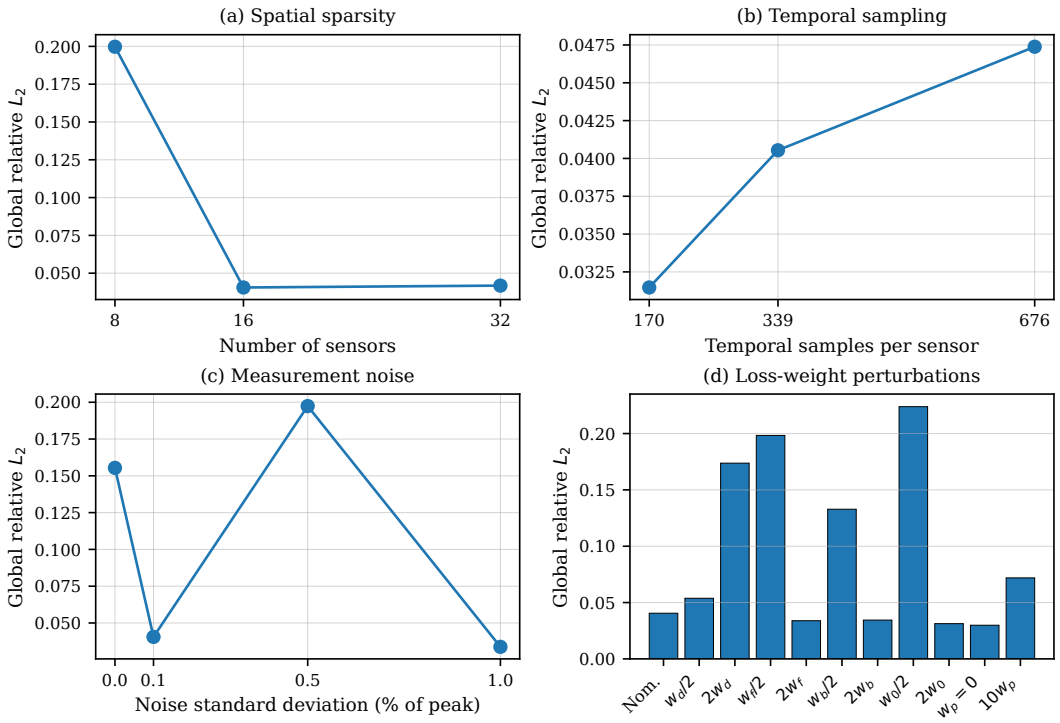


Figure 4: Single-run controlled sensitivity of E_{L_2}. Panels vary (a) sensor count, (b) temporal samples per sensor, (c) noise standard deviation, and (d) one loss weight at a time. "Nom." denotes the ordered vector $(w_d, w_f, w_b, w_0, w_p) = (50, 1, 10, 10, 10^{-4})$.

Spatial coverage has the clearest effect. With eight sensors, E_{L_2} rises to 0.1998 and the relative errors in (α, γ, β) are $(76.03, 70.20, 36.79)\%$. With sixteen sensors, the corresponding values are 0.0405 and $(3.38, 21.84, 6.81)\%$. Increasing the count to 32 leaves the field error nearly unchanged at 0.0418, but improves the parameter errors to $(2.11, 7.26, 2.23)\%$. Additional spatial coverage therefore improves coefficient observability even after field accuracy has nearly saturated.

Temporal subsampling is less damaging over the tested range. The cases with 170, 339, and 676 samples per sensor give E_{L_2} values of 0.0315, 0.0405, and 0.0474. This nonmonotonic order does not mean that fewer measurements are inherently better. It shows that fixed-budget, nonconvex training can respond to data density through changes in effective loss balance and stochastic collocation. The noise sweep is likewise nonmonotonic: E_{L_2} equals 0.1554, 0.0405, 0.1974, and 0.0338 for standard deviations of 0, 0.1%, 0.5%, and 1% of the peak field. These single-run values are not evidence that noise improves the inverse problem. They instead reveal optimizer variability and motivate repeated seeds, ensembles, or Bayesian uncertainty analysis [13].

The loss perturbations confirm the need for balance. Doubling w_d or halving w_f raises E_{L_2} to 0.1737 and 0.1983 because data fitting dominates without sufficient physics regularization. Doubling w_f, w_b, or w_0 gives errors of 0.0339, 0.0344, and 0.0313. Removing the weak prior gives 0.0299, whereas increasing it tenfold gives 0.0719 and biases all

three coefficients. The prior is therefore an early conditioning device, not a source of final physical information. The nominal vector is a stable reference configuration, but these results favor future adaptive or gradient-balanced weighting over any claim of universal optimality [10].

5 Discussion

The results show that the physics-informed formulation improves temperature-field reconstruction under sparse sensing, while parameter recovery remains more sensitive to observability. The controlled comparison isolates the contribution of the governing-equation and constraint terms, whereas the sensitivity analysis identifies spatial coverage and loss balance as important factors affecting the inverse solution. These findings should be interpreted within the scope of the synthetic benchmark and fixed-budget training protocol.

Table 2 shows relative errors below 8% for α and β, but 24.54% for γ. This difference is physically plausible. Diffusivity and volumetric loss both affect temporal decay and spatial smoothing, making them difficult to separate with sparse sensors; by contrast, source amplitude relates more directly to peak temperature. The result supports accurate field reconstruction and partial coefficient recovery, while confirming that state and parameter errors must be interpreted separately.

This comparison is specific to one benchmark and is not a universal ranking of inverse heat-transfer methods. Classical regularized optimization can be highly competitive when the forward model is reliable and repeated solves are affordable. Operator-learning surrogates may be preferable when many parameterized queries are available. The supported claim is narrower: for the present sparse moving-source problem, the physics constraints prevent the severe off-sensor degradation observed in the two data-only baselines.

5.1 Transfer to experimental measurements and limitations

The validation uses synthetic finite-difference data and therefore does not establish experimental deployment performance. Real thermocouples, resistance sensors, and infrared cameras introduce calibration offsets, gain drift, quantization, finite spatial footprints, temporal lag, missing samples, synchronization error, and sensor-position uncertainty; infrared measurements additionally depend on emissivity, reflected ambient radiation, viewing angle, and background conditions. These effects can exceed the independent additive Gaussian noise assumed here.

The zero initial field of Equation (6) is a property of the synthetic benchmark, not a limitation of the framework: the initial-condition term of the loss accepts any prescribed field $u_0(x, y)$, and an unknown initial state could be estimated jointly or supplied from a separate measurement. Transfer of the reported results to a real thermal system therefore requires a known or measured initial field, a valid two-dimensional model form and boundary representation, and a source model consistent with the actual heat input; under those conditions the identification workflow applies unchanged, while the reported error levels remain specific to this benchmark.

Model discrepancy is equally important: experimental boundaries may exchange heat by convection or radiation rather than satisfy a homogeneous Dirichlet condition, source position and intensity may be uncertain, material properties may vary with temperature, and three-dimensional losses may invalidate a two-dimensional model. A practical workflow should calibrate sensors independently, reserve spatially distinct sensors and time intervals for validation, use robust or uncertainty-weighted data losses, and introduce trainable sensor offsets or gains when justified; temporal and spatial convolution can represent finite sensor response, and uncertain boundary fluxes and source trajectories can be inferred jointly. Ensemble or Bayesian PINNs can provide uncertainty intervals instead of a single deterministic field [13]. Controlled tests on a plate instrumented with traceable contact sensors or a calibrated infrared camera are required before claiming experimental superiority.

The study also has computational and inferential limitations: it uses one nominal run and one run per sensitivity case, so optimizer variability is not quantified statistically; sensor locations are random rather than optimized, the source form is assumed known, and the parameter prior is centered on the initial guesses. The remaining bias in γ indicates structural correlation between diffusion and dissipation. These limitations motivate repeated-seed studies, optimal sensor placement, adaptive loss balancing, uncertainty quantification, hard boundary enforcement, and tests with unknown source trajectories or spatially varying coefficients.

6 Conclusions

A sparse-sensor PINN was evaluated for transient two-dimensional inverse heat conduction with simultaneous recovery of thermal diffusivity, volumetric heat loss, and source amplitude. With sixteen noisy sensors, the nominal

run achieved a mean RMSE of 3.52×10^{-3} n.t.u. and $E_{L_2} = 2.87 \times 10^{-2}$. The parameter errors were 5.04%, 24.54%, and 7.90%, showing that accurate field recovery does not imply equal observability of every coefficient.

The controlled baselines show that governing physics, not network capacity alone, explains reconstruction quality: mean RMSE decreases by more than 95% relative to both the matched data-only neural network and spatiotemporal interpolation. The sensitivity study identifies insufficient spatial coverage and unbalanced loss weights as the most consequential failure modes in the examined configuration. Its nonmonotonic temporal and noise results also confirm that one fixed-budget run is not a statistical robustness assessment. Future work should combine repeated seeds, adaptive loss weighting, optimized sensor placement, uncertainty quantification, and controlled experimental measurements.

Code and data availability. The MATLAB R2026a source code for this work and the result tables used are available at `https://la.mathworks.com/matlabcentral/fileexchange/183734-sparse-sensor-pinn-reconstruction-and-identification`.

Funding. This work was supported by the Instituto Politécnico Nacional, Mexico.

Conflicts of interest. The authors declare no conflicts of interest.

Acknowledgments. The first author gratefully acknowledges the support and encouragement of his wife, Carolina Rodríguez.

References

[1] Steven L. Brunton and J. Nathan Kutz. *Data-Driven Science and Engineering: Machine Learning, Dynamical Systems, and Control*. Cambridge University Press, 2022. DOI: 10.1017/9781009089517.

[2] Maziar Raissi, Paris Perdikaris, and George E. Karniadakis. "Physics-Informed Neural Networks: A Deep Learning Framework for Solving Forward and Inverse Problems Involving Nonlinear Partial Differential Equations". In: *Journal of Computational Physics* 378 (2019), pp. 686–707. DOI: 10.1016/j.jcp.2018.10.045.

[3] George E. Karniadakis et al. "Physics-Informed Machine Learning". In: *Nature Reviews Physics* 3.6 (2021), pp. 422–440. DOI: 10.1038/s42254-021-00314-5.

[4] Shengze Cai et al. "Physics-Informed Neural Networks for Heat Transfer Problems". In: *Journal of Heat Transfer* 143.6 (2021), p. 060801. DOI: 10.1115/1.4050542.

[5] Jorge Morales and Wen Yu. "Improving neural network's performance using Bayesian inference". In: *Neurocomputing* 461 (2021), pp. 319–326. DOI: 10.1016/j.neucom.2021.07.054.

[6] Weinan E and Bing Yu. "The Deep Ritz Method: A Deep Learning-Based Numerical Algorithm for Solving Variational Problems". In: *Communications in Mathematics and Statistics* 6.1 (2018), pp. 1–12. DOI: 10.1007/s40304-018-0127-z.

[7] Justin Sirignano and Konstantinos Spiliopoulos. "DGM: A Deep Learning Algorithm for Solving Partial Differential Equations". In: *Journal of Computational Physics* 375 (2018), pp. 1339–1364. DOI: 10.1016/j.jcp.2018.08.029.

[8] Lu Lu et al. "DeepXDE: A Deep Learning Library for Solving Differential Equations". In: *SIAM Review* 63.1 (2021), pp. 208–228. DOI: 10.1137/19M1274067.

[9] Ehsan Haghighat and Ruben Juanes. "SciANN: A Keras/TensorFlow Wrapper for Scientific Computations and Physics-Informed Deep Learning Using Artificial Neural Networks". In: *Computer Methods in Applied Mechanics and Engineering* 373 (2021), p. 113552. DOI: 10.1016/j.cma.2020.113552.

[10] Sifan Wang, Yujun Teng, and Paris Perdikaris. "Understanding and Mitigating Gradient Flow Pathologies in Physics-Informed Neural Networks". In: *SIAM Journal on Scientific Computing* 43.5 (2021), A3055–A3081. DOI: 10.1137/20M1318043.

[11] Ameya D. Jagtap, Kenji Kawaguchi, and George E. Karniadakis. "Adaptive Activation Functions Accelerate Convergence in Deep and Physics-Informed Neural Networks". In: *Journal of Computational Physics* 404 (2020), p. 109136. DOI: 10.1016/j.jcp.2019.109136.

[12] Ehsan Kharazmi, Zhongqiang Zhang, and George E. M. Karniadakis. "hp-VPINNs: Variational Physics-Informed Neural Networks with Domain Decomposition". In: *Computer Methods in Applied Mechanics and Engineering* 374 (2021), p. 113547. DOI: 10.1016/j.cma.2020.113547.

[13] Liu Yang, Xuhui Meng, and George E. Karniadakis. "B-PINNs: Bayesian Physics-Informed Neural Networks for Forward and Inverse PDE Problems with Noisy Data". In: *Journal of Computational Physics* 425 (2021), p. 109913. DOI: 10.1016/j.jcp.2020.109913.

[14] Lu Lu et al. "Learning Nonlinear Operators via DeepONet Based on the Universal Approximation Theorem of Operators". In: *Nature Machine Intelligence* 3.3 (2021), pp. 218–229. DOI: 10.1038/s42256-021-00302-5.

[15] Salvatore Cuomo et al. "Scientific Machine Learning Through Physics-Informed Neural Networks: Where We Are and What's Next". In: *Journal of Scientific Computing* 92 (2022), p. 88. DOI: 10.1007/s10915-022-01939-z.

[16] Nima Zobeiry and Kevin D. Humfeld. "A Physics-Informed Machine Learning Approach for Solving Heat Transfer Equation in Advanced Manufacturing and Engineering Applications". In: *Engineering Applications of Artificial Intelligence* 101 (2021), p. 104232. DOI: 10.1016/j.engappai.2021.104232.

[17] Vivek Oommen and Balaji Srinivasan. "Solving Inverse Heat Transfer Problems Without Surrogate Models: A Fast, Data-Sparse, Physics Informed Neural Network Approach". In: *Journal of Computing and Information Science in Engineering* 22.4 (2022), p. 041012. DOI: 10.1115/1.4053800.

[18] Zhili He et al. "A Physics-Informed Deep Learning Method for Solving Direct and Inverse Heat Conduction Problems of Materials". In: *Materials Today Communications* 28 (2021), p. 102719. DOI: 10.1016/j.mtcomm.2021.102719.

[19] Md Muhtasim Billah et al. "Physics-Informed Deep Neural Network for Inverse Heat Transfer Problems in Materials". In: *Materials Today Communications* 35 (2023), p. 106336. DOI: 10.1016/j.mtcomm.2023.106336.

[20] Myeong Seok Go, Jae Hyuk Lim, and Seungchul Lee. "Physics-Informed Neural Network-Based Surrogate Model for a Virtual Thermal Sensor with Real-Time Simulation". In: *International Journal of Heat and Mass Transfer* 214 (2023), p. 124392. DOI: 10.1016/j.ijheatmasstransfer.2023.124392.

[21] MS Bidou, J-G Bauzin, and N Laraqi. "Physics-informed neural networks for 2D-transient inverse heat conduction problem involving static and moving heat source". In: *International Journal of Heat and Mass Transfer* 259 (2026), p. 128349.

[22] Yuxuan Li et al. "An improved physics-informed neural network framework for solving transient nonlinear and inhomogeneous heat conduction problems". In: *International Journal of Heat and Mass Transfer* 252 (2025), p. 127515. DOI: 10.1016/j.ijheatmasstransfer.2025.127515.

[23] Xinchao Jiang et al. "Practical uncertainty quantification for space-dependent inverse heat conduction problem via ensemble physics-informed neural networks". In: *International Communications in Heat and Mass Transfer* 147 (2023), p. 106940. DOI: 10.1016/j.icheatmasstransfer.2023.106940.

[24] Yuanbin Shang, Huaiguo Ban, and Donghuan Liu. "Simultaneous identification of boundary heat flux and thermal conductivity in inverse heat conduction problems using physics-informed neural networks". In: *Thermal Science and Engineering Progress* 65 (2025), p. 103905. DOI: 10.1016/j.tsep.2025.103905.

[25] Mohamed Salim Bidou, Jean-Gabriel Bauzin, and Najib Laraqi. "Physics-informed neural networks for 2D-transient inverse heat conduction problem involving static and moving heat source". In: *International Journal of Heat and Mass Transfer* 259 (2026), p. 128349. DOI: 10.1016/j.ijheatmasstransfer.2026.128349.

[26] Cesar Solis et al. "Transformer- and GRU-Based Identification of Open-Chain Robot Kinematics Using Product-of-Exponentials Coordinates". In: *Technologies* 14.6 (2026), p. 333. DOI: 10.3390/technologies14060333.

Journal of Dynamical Systems and Complexity (2026) vol.1(3): 1-End
eISSN: 3122-4326, DOI: 10.66131/JDSC12202615-27

Noise-Induced Dynamics in a Multistable Erbium-Doped Fiber Laser: A Short Review From Extreme Events to Photonic Information Processing

Rider Jaimes Reátegui, Juan Hugo García López, and Guillermo Huerta Cuellar *

Optics, Complex Systems and Innovation Laboratory, Centro Universitario de los Lagos
Universidad de Guadalajara, Enrique Díaz de León 1144, Lagos de Moreno, Jalisco, México, CP 47463.

Abstract

Noise is often regarded as a source of instability and degraded performance in optical systems. In nonlinear dynamical systems, this view is incomplete: fluctuations can reveal critical susceptibility, activate transitions among coexisting attractors, generate rare extreme excursions, and enable probabilistic information processing. This review develops a unified narrative around diode-pumped erbium-doped fiber lasers (EDFLs), a compact photonic platform in which multistability, bifurcations, attractor hopping, prebifurcation noise amplification, rogue-wave generation, deterministic Brownian-like dynamics, symbolic diagnostics, optical logic, and data-driven stochastic cloning have all been investigated. We first establish the EDFL as a class-B nonlinear oscillator and review its reduced rate-equation description, emphasizing the roles of pump modulation, amplified spontaneous emission, and basin geometry. We then examine noise-induced hopping among periodic attractors and the amplification of fluctuations near saddle-node, period-doubling, and crisis bifurcations. These mechanisms lead naturally to extreme-event physics, where filtered noise promotes rare visits to high-amplitude subharmonic states and produces non-Gaussian rogue-wave statistics. A central methodological issue is the distinction between stochastic forcing and deterministic dynamics that exhibit Brownian-like or pink-noise-like statistics. We discuss deterministic Brownian motion and ordinal-pattern methods as complementary diagnostic tools. Finally, we review how noise-controlled state occupation can be used for optical logic and how reservoir computing differentiates strong trajectory cloning from weak statistical cloning in partially observed stochastic systems. The main conclusion is that noise in a multistable EDFL is simultaneously a perturbation, a probe of hidden dynamical structure, and a controllable resource for photonic information processing.

Keywords— erbium-doped fiber laser; nonlinear dynamics; multistability; noise-induced intermittency; bifurcation; rogue waves; reservoir computing; optical logic gates

1 Introduction

Noise is commonly associated with uncertainty, limited reproducibility, and reduced signal quality. This association is justified in many practical systems, but nonlinear dynamics provides a more nuanced picture. In the presence of multiple stable attractors, noise can induce transitions between qualitatively distinct states; near a bifurcation, it can be strongly amplified; and in metastable regimes, it can make rare high-amplitude excursions observable. Consequently, the effect of noise is determined not only by its variance or amplitude but also by the geometry of the deterministic phase space, the local stability of attractors, the location of basin boundaries, the distance to critical transitions, and the temporal spectrum of the forcing [1, 2].

This broader perspective has been developed in many physical contexts. Noise-induced switching between attractors, stochastic resonance, coherence resonance, critical amplification, and noise-induced intermittency show that fluctuations can produce structured dynamical responses rather than merely featureless disturbances [3, 4, 5, 6]. The challenge is to identify the deterministic mechanism through which noise is transformed into a measurable response. A particularly effective strategy is to use a physical system that is simultaneously nonlinear, experimentally controllable, and sufficiently well modeled to connect observations with state-space dynamics.

Lasers fulfill these criteria. Their dynamics may include locking, period doubling, quasiperiodicity, chaotic oscillations, synchronization, and coexistence of multiple attractors. The experimental discovery of subharmonic bifurcations, multistability, and turbulence in a Q-switched gas laser provided an early demonstration that lasers are

*Corresponding author: guillermo.huerta@academicos.udg.mx
Received: July 19, 2025, **Published:** October 30, 2026
Editor: E. Ditor

useful laboratories for nonlinear dynamics [7]. Fiber lasers are especially attractive because they are compact, efficient, compatible with fiber-optic components, and relevant to communications, sensing, reflectometry, medicine, and metrology [8, 9]. Erbium-doped fiber lasers, in particular, operate in the technologically important telecommunications region and possess a rich interplay between gain, loss, population inversion, cavity feedback, spontaneous emission, and external pump modulation.

The present review focuses on a connected body of work involving diode-pumped EDFLs subjected to harmonic pump modulation and externally added noise. The sequence begins with experimental evidence that noise can cause hopping among coexisting periodic attractors [10]. It then shows that fluctuations are amplified as the laser approaches saddle-node, period-doubling, and crisis bifurcations [11]. These observations lead to extreme-event physics: low-pass-filtered perturbations can trigger rare high-amplitude periodic excursions whose peak-intensity statistics satisfy a rogue-wave criterion [12]. The ensuing analysis of multistate intermittency demonstrates that the amplitude and cutoff frequency of the injected noise regulate which periodic states are visited and how likely extreme pulses become [13].

A complementary step is to determine whether forcing merely changes the state reached from a given preparation or actually removes competing attractors. Numerical basin mapping addresses this distinction: harmonic control can eliminate selected attractors together with their basins, whereas weak random forcing changes the statistical distribution of initial conditions assigned to each surviving state [14]. Building on earlier attractor-annihilation theory and EDFL experiments [15, 16], this basin-resolved perspective connects observed switching to the control of the underlying phase-space organization.

The review also addresses an essential inferential problem. An irregular time series may be caused by external stochastic forcing, deterministic chaos, hidden variables, or a mixture of all three. Therefore, the study of noisy lasers requires methods capable of detecting deterministic constraints even when standard statistics appear stochastic.

Finally, this body of research has moved from characterization toward function. Noise-controlled multistability can serve as a basis for optical logic, where individual periodic laser states encode logical operations [17]. Reservoir computing further provides a framework for determining whether a noisy, partially observed system can be predicted trajectory by trajectory or only statistically cloned [18]. This work reviews the importance of noise in nonlinear dynamical systems, using the erbium-doped fiber laser as a natural and exceptionally useful example. The EDFL is compelling because it concentrates, within a compact photonic cavity, the central themes of complex dynamics: bifurcations, multistability, stochastic activation, intermittency, extreme events, hidden variables, and information processing. Understanding how noise reshapes its dynamics makes it possible not only to explain rare optical events, but also to transform fluctuations into a controllable resource for sensing, computation, and statistical prediction.

2 Conceptual Background: Multistability, Noise, and Criticality

2.1 Multistability and basin structure

A multistable system possesses more than one attractor for the same set of control parameters. The asymptotic state reached by a trajectory therefore depends on its initial condition. The collection of initial conditions converging to an attractor defines its basin of attraction. Basin boundaries can be smooth or fractal, and their geometry can strongly influence sensitivity to perturbations [2]. In experimental systems, multistability is often detected by varying initial conditions, scanning control parameters in opposite directions, or repeatedly resetting the system.

The importance of multistability is twofold. From a fundamental perspective, it creates a state-space organization in which different long-term behaviors coexist. From an applied perspective, it offers a set of possible dynamical states that can represent memory, logic levels, operating modes, or encoded information. However, it also creates ambiguity: small perturbations may redirect the system to an undesired attractor. Noise-induced hopping is precisely the process through which fluctuations exploit this sensitivity.

In a simplified potential analogy, different stable attractors can be represented as wells separated by barriers. This analogy is useful for intuition but incomplete in non-gradient, driven, and chaotic systems. In such systems, switching may involve unstable periodic orbits, chaotic saddles, riddled or fractal basin boundaries, and transient channels rather than thermal activation over a static energy barrier [1, 2]. The EDFL studies reviewed below are important because they provide experimentally accessible examples of multistate hopping in a nonequilibrium optical oscillator.

2.2 Noise-induced transitions and intermittency

Noise-induced switching occurs when a perturbation displaces a trajectory from one basin into another. The resulting time series may alternate between discrete dynamical regimes, producing intermittency. In a two-state system, the key observables are switching probabilities, residence times, transition rates, and the stationary occupation distribution. In a multistate system, the dynamics can be represented by a transition matrix, symbolic sequence, or state network. The number of accessible states may itself depend on noise amplitude and spectrum.

The interplay between deterministic and random structure can be quantified using entropy measures. If a symbolic sequence contains a single repeated state, its Shannon entropy vanishes. When several states occur with comparable probability, the entropy increases. Entropy alone does not identify the underlying mechanism, but in a controlled experiment it provides a compact descriptor of the complexity of the state sequence [10]. Such coarse-grained representations are especially useful when the underlying intensity signal contains fast oscillations while the relevant physical question concerns the order and probability of visits to attractors.

2.3 Bifurcations and critical susceptibility

A bifurcation is a qualitative change in the set or stability of solutions caused by variation of a control parameter. In the EDFL literature considered here, saddle-node bifurcations create or destroy periodic attractors, period-doubling transitions change temporal periodicity, and crises reorganize chaotic or attracting sets [11]. Close to a bifurcation, restoring stability weakens and the response to perturbations may become large. This is the basis of prebifurcation noise amplification.

Theoretical studies of noisy bifurcations have shown that small perturbations can be amplified near critical points and that the response depends on both deterministic normal forms and noise properties [3, 4]. In applications, this observation motivates early-warning indicators. However, an increase in variance, autocorrelation, or spectral power should not be interpreted as a universal predictor without system-specific validation. Measurement noise, slow parameter drift, nonstationarity, and changes in forcing can imitate critical signals. The EDFL platform is valuable because the control parameter can be scanned reproducibly and the noise input can be adjusted deliberately.

3 Erbium-Doped Fiber Lasers as a Platform for Nonlinear Dynamics

3.1 Physical architecture and technological relevance

An EDFL is based on an optical fiber whose core contains erbium ions. Optical pumping raises ions to an excited manifold, and stimulated emission near the 1.5-μm region supports laser action. Fiber Bragg gratings, mirrors, couplers, wavelength-division multiplexers, isolators, and photodetectors can be incorporated into a compact cavity and measurement chain. Rare-earth-doped fiber lasers offer high gain, single-mode operation, robust beam guidance, and compatibility with telecommunication components [8, 9].

The Fig 1, shows the EDFL configuration used in the 2009 prebifurcation study consisted of a 1560-nm fiber laser with a 3.51-m Fabry–Pérot cavity formed by an 82-cm heavily doped erbium fiber, a Faraday rotating mirror, and a fiber Bragg grating. The cavity was pumped by a 977-nm diode. A wavelength-division multiplexer guided the output to a photodetector, oscilloscope, and Fourier spectrum analyzer [11]. The Faraday rotating mirror was used to reduce polarization-mode-beating effects that could add unwanted complexity. These experimental details matter because they identify the physical source of the observed dynamics and delimit the model's intended regime.

3.2 EDFL Dynamical Model

The pump-modulated erbium-doped fiber laser is described as a class-B laser. Since polarization relaxes much faster than the optical field and the population inversion, its dynamics can be reduced to two coupled equations for the intracavity power $P_g(t)$ and the normalized upper-level population $y(t)$. The model includes gain saturation, ground-state absorption, excited-state absorption, cooperative upconversion, amplified spontaneous emission (ASE), and periodic and stochastic pump forcing [11].

The intracavity power obeys

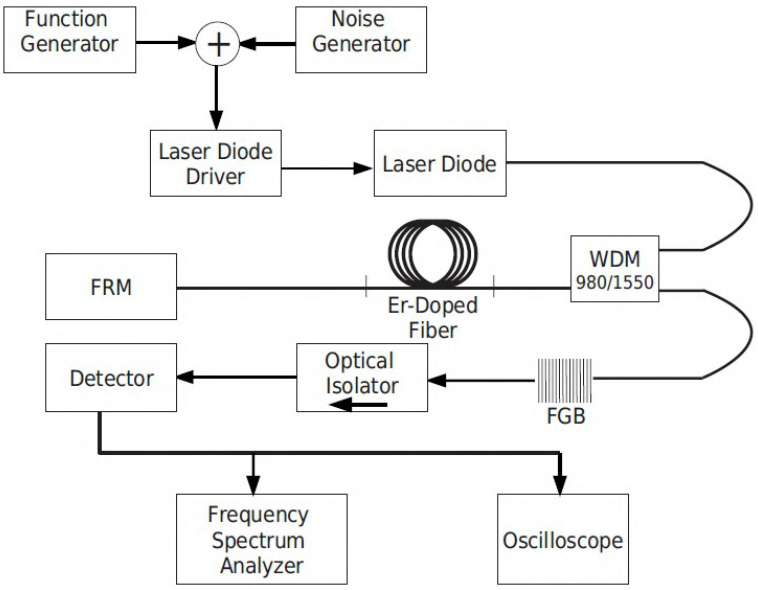


Figure 1: Experimental EDFL setup, [11].

$$\frac{dP_g}{dt} = \frac{2L_0}{T_r}\Big[P_g\left\{\gamma\alpha_0\left[(\tau-\xi)y-1\right]-\alpha_l\right\} + 2\gamma\alpha_0(\tau-1)y\frac{\Delta\lambda_g}{\Delta\lambda_{\mathrm{Er}}}K(y)\exp(-L\alpha_l)\Big], \tag{1}$$

where the first contribution represents the net balance between optical gain and cavity losses, while the second term accounts for ASE seeding of the laser mode.

The upper-level population evolves as

$$\frac{dy}{dt} = -\frac{\gamma\alpha_0 N_0 S_a}{h\nu_g}P_g(\tau y-1) - \frac{y}{\tau_0} + \frac{4\left[K'(y)-1\right]\gamma\alpha_0(\tau-1)}{\tau_0\Delta\lambda_{\mathrm{Er}}N_0S_a} - \frac{y^2}{\tau_1} + \frac{\left[1-\exp\left(-\varepsilon\alpha_0L_0(1-y)\right)\right]S_p}{N_0L_0h\nu_p}P_p\left[1+A\sin(2\pi f_m t)+n\zeta\right]. \tag{2}$$

The terms in Eq. (2) describe, respectively, stimulated transitions, spontaneous relaxation of isolated Er^{3+} ions, ASE-related population depletion, cooperative upconversion in excited ion pairs, and pump absorption. The final factor contains harmonic modulation of amplitude A and frequency f_m, together with externally applied noise of amplitude n; ζ represents the random sequence.

The ASE coefficients averaged over the active fiber are

$$K(y) = \frac{\exp\left[L_0\gamma\alpha_0\left((\tau-\xi)y-1\right)\right]-1}{L_0\gamma\alpha_0\left((\tau-\xi)y-1\right)}, \tag{3}$$

$$K'(y) = \frac{\exp\left[L_0\gamma\alpha_0'\left((\tau'-\xi')y-1\right)\right]-1}{L_0\gamma\alpha_0'\left((\tau'-\xi')y-1\right)}. \tag{4}$$

For simplicity, the model assumes

$$\tau' = \tau, \qquad \xi' = \xi, \qquad \gamma' = \gamma. \tag{5}$$

The main definitions are

$$\alpha_0 = N_0\sigma_{\mathrm{GSA}}, \qquad \tau = 1 + \frac{\sigma_e}{\sigma_{\mathrm{GSA}}}, \qquad \xi = \frac{\sigma_{\mathrm{ESA}}}{\sigma_{\mathrm{GSA}}}, \tag{6}$$

$$\gamma = 1 - \exp\left(-\frac{S_a}{S_w}\right), \qquad S_a = \pi a^2, \qquad S_w = \frac{\pi w_0^2}{2}, \tag{7}$$

$$T_r = \frac{2n_0 L}{c}, \qquad L = L_0 + l_0, \qquad \alpha_l = \alpha - \frac{\ln(R_1 R_2)}{2L}. \tag{8}$$

Here, N_0 is the erbium-ion concentration, σ_{GSA}, σ_e, and σ_{ESA} are the ground-state absorption, emission, and excited-state absorption cross sections, respectively. The quantities τ_0 and τ_1 are the relaxation times of isolated ions and excited ion pairs. The parameters L_0, l_0, and L define the active, passive, and total cavity lengths, whereas R_1 and R_2 are the cavity reflectivities.

Including ASE is essential in this model because it permits agreement between simulations and the experimentally measured relaxation oscillation frequency, close to 30 kHz for the operating conditions reported in [11], and its references.

The model contains physically meaningful parameters: photon round-trip time, small-signal absorption, threshold losses, erbium-ion lifetime, overlap between the guided mode and doped core, absorption and stimulated-emission cross sections, and pump absorption. Its strength is that the same basic equations can reproduce experimentally observed relaxation oscillations, periodic locking, multistability, and responses to modulation. Its limitation is that it represents a reduced effective description: spatial, polarization, longitudinal-mode, thermal, and technical noise degrees of freedom may not be fully resolved. The laser parameters for equations 1 and 2, are as the next Table 1:

Table 1: Parameters used in the numerical simulations of the pump-modulated erbium-doped fiber laser (EDFL). Values are reproduced from Table I of Huerta-Cuellar et al. [11].

Symbol	Description	Value	Units
λ_g	Laser-generation wavelength	1560	nm
λ_p	Pump wavelength	977	nm
$h\nu_p$	Pump-photon energy	2.037×10^{-19}	J
α_0	Small-signal absorption coefficient at λ_g	0.06	cm^{-1}
N_0	Er^{3+} ion concentration	2.4×10^{19}	cm^{-3}
σ_{GSA}	Ground-state absorption cross section	2.48×10^{-21}	cm^2
σ_e	Emission cross section	2.25×10^{-21}	cm^2
τ_0	Lifetime of an isolated excited Er^{3+} ion	10	ms
τ_1	Effective relaxation time of excited Er^{3+}–Er^{3+} pair clusters	0.71	ms
$\Delta\lambda_g$	Er^{3+} generation bandwidth	25	nm
$\Delta\lambda_{\mathrm{Er}}$	Er^{3+} emission-band width	10^3	nm
w_0	Guided fundamental-mode radius	3.5	μm
a	Erbium-doped fiber-core radius	2.7	μm
L_0	Active erbium-fiber length	0.82	m
L	Total cavity length	3.51	m
l_0	Total length of passive intracavity fiber components	2.61	m
R_1	Faraday rotating mirror reflectivity	1.00	–
R_2	Fiber Bragg grating reflectivity	0.91	–
ε	Ratio of pump absorption coefficients at λ_p and λ_g	0.7	–
ξ	Ratio of excited-state to ground-state absorption cross sections	0.24	–
η	Ratio of generation to spontaneous-emission bandwidths	2	–
n_0	Refractive index of the fiber core	1.46	–

Note. The parameter names follow the physical definitions given in the model description of Huerta-Cuellar et al. [11]. Verify the symbols against the notation ultimately adopted in the review, since different EDFL articles sometimes use equivalent coefficients with different symbols.

Table 2: Periodic states and their roles in the EDFL narrative.

State	Spectral/dynamical interpretation	Role in the reviewed studies
$P1$	Fundamental response, dominant frequency near f_m	Baseline attractor; one endpoint of hopping; associated with OR in the logic proposal
$P3$	Period-three subharmonic response, near $f_m/3$	Coexisting attractor; first state often involved in hopping; associated with AND
$P4$	Period-four subharmonic response, near $f_m/4$	Large-amplitude state; rare occupation can generate rogue-wave-like events; associated with NOR
$P5$	Period-five subharmonic response, near $f_m/5$	Appears in extended multistate intermittency; associated with NAND

The pump can be harmonically modulated as

$$P_p(t) = p\,[1 - m\sin(2\pi f_m t)]\,, \tag{9}$$

where p denotes the pump level in the absence of modulation, m is modulation depth, and f_m is the driving frequency. Under this forcing, the EDFL can support a fundamental period-one response $P1$ as well as subharmonic periodic responses $P3$, $P4$, and $P5$. The latter have dominant frequencies near $f_m/3$, $f_m/4$, and $f_m/5$, respectively [13, 17].

The numerical bifurcation diagrams, Figure 2 in the 2012 and 2024 studies show parameter regions in which several of these orbits coexist. Basin calculations at fixed modulation frequency reveal that increasing modulation depth changes their relative basin volumes: subharmonic attractors emerge and expand while the relative basin of $P1$ may shrink [13]. This provides a direct dynamical interpretation of why externally injected noise can change the observed state distribution without changing the nominal deterministic control parameters.

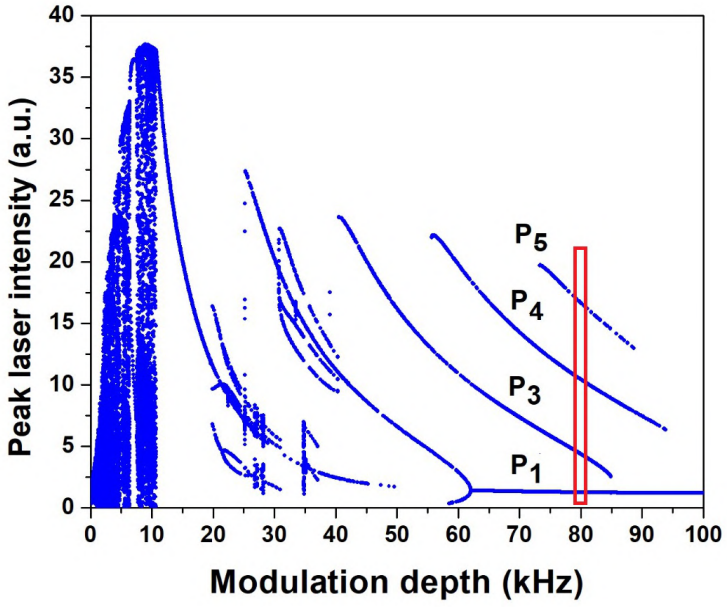


Figure 2: Bifurcation diagram [17].

4 Experimental Characterization of Hopping Dynamics in a Multistable Fiber Laser

The 2008 study *Experimental characterization of hopping dynamics in a multistable fiber laser* provides the experimental foundation of the review [10]. The central question was how external noise changes the dynamics of a fiber laser operating in a multistable region. At a low noise amplitude, the laser remains on a periodic attractor selected by initial conditions. As the noise increases, the system begins to switch between coexisting periodic states. The observed dynamics progresses from $P3$–$P1$ hopping to regimes involving $P4$ and ultimately $P5$.

4.1 From state persistence to multistate hopping

At low noise, the experiment showed coexistence of periodic attractors whose characteristic power spectra contained distinct subharmonic components. The system remained in the chosen attractor for arbitrarily long observation times within the experimental window, apart from noisy fluctuations around the periodic orbit. When input noise exceeded a threshold, the laser jumped between $P3$ and $P1$. At larger amplitudes, three and four periodic states participated in the intermittent dynamics [10].

The appearance of $P5$ only at a sufficiently large noise amplitude is particularly informative. It raises the possibility that a state with a small basin is inaccessible in practice without perturbation, or that noise reorganizes the effective dynamics so that a new periodic state becomes observable. The authors appropriately state that the experiment cannot fully distinguish these possibilities because all initial conditions cannot be varied exhaustively. This caution illustrates a recurring challenge in experimental multistability: observed state sets can depend on finite sampling, preparation protocol, and noise level.

4.2 Noise transfer and saturation-like behavior

The relation between input noise N_{in} and output spectral noise N_{out} was measured for individual periodic states and for hopping regimes. For isolated $P1$, $P3$, and $P4$ attractors, the output spectral component was approximately linear in the input amplitude, with larger slopes for higher-period orbits. In contrast, once the laser began hopping among states, the output-noise dependence became much weaker. Figuer 3, shows the reported $P3$–$P1$–$P4$–$P5$ hopping regime, the effective slope was substantially smaller than the slope associated with the isolated periodic states [10].

This behavior was described as a noise-saturation effect. Its exact physical mechanism remained unresolved, but the proposed interpretation was that input-noise energy may be redistributed over an increasing number of transitions and states. That interpretation is plausible but should be treated as a hypothesis rather than a settled mechanism. A future experiment could test it by measuring state-resolved spectra, transition-conditioned fluctuations, and the dependence of output power on dwell time in each attractor.

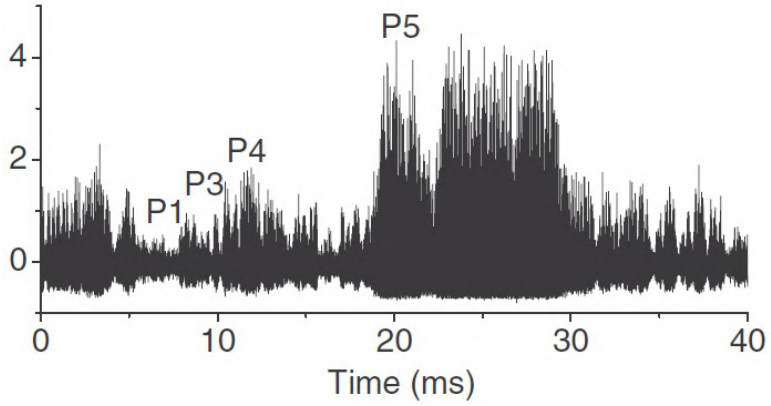


Figure 3: Four attractors interacting in hopping regime, [10].

4.3 Occupation probabilities, entropy, and residence times

The probability of visiting a periodic state is a key observable in noise-driven multistability. In the 2008 experiment, the probability of visiting $P3$ decayed exponentially with noise amplitude in the hopping regime, whereas the

probability of $P1$ increased. The crossover in state probabilities coincided with a change in the output-noise curve, suggesting that occupation redistribution and noise transfer are linked [10, 13].

The authors encoded the sequence of attractor visits symbolically and computed a Shannon entropy rate. A purely periodic regime yields zero entropy because only one symbol appears. The entropy rose when new states entered the dynamics, then remained approximately constant inside a multistate region. Residence-time statistics also displayed scaling behavior, including a reported $-3/2$ power-law feature for a distribution associated with period-one windows in a two-state intermittent regime [10]. These results establish that the relevant dynamics are not captured by amplitude statistics alone: state sequencing and temporal organization matter.

4.4 Connection with general multistable dynamics

The EDFL experiment is consistent with prior observations of noise-induced attractor hopping in multistable systems [1]. More generally, multistability has been identified as an organizing principle in physical, biological, and cognitive systems [2, 19]. The laser contribution is distinctive because the attractors are optical periodic states with well-defined spectral signatures and the noise input can be electronically controlled. This makes the EDFL a promising system for controlled studies of multistate transition networks.

5 Prebifurcation Noise Amplification in a Fiber Laser

The 2009 study *Prebifurcation noise amplification in a fiber laser* investigated how intrinsic and externally added noise behave near critical transitions [11]. The work combined experiment and numerical modeling to address a basic question: can the approach to bifurcation be detected through enhanced fluctuations in an EDFL?

5.1 Bifurcation structure and experimental protocol

The experimental bifurcation diagram was constructed by scanning modulation frequency while recording the peak-to-peak laser intensity. Initial conditions were varied by switching the signal generator on and off and by scanning the modulation frequency in opposite directions. The resulting diagram displayed periodic states and chaotic regions, including $P3$, $P4$, and $P5$ branches born and destroyed through saddle-node bifurcations. Crisis and inverse period-doubling transitions were also identified [11].

This protocol illustrates an important experimental principle: detecting multistability requires intentional perturbation or resetting. A standard one-direction parameter scan may miss coexisting branches. The EDFL therefore serves not only as a source of complex behavior but also as a controlled system in which state preparation can be incorporated into the measurement design.

5.2 Experimental evidence of amplification

The spectral noise density at the modulation frequency was measured as the modulation frequency approached critical points. For both intrinsic laser noise and externally added noise, the noise floor rose near saddle-node, period-doubling, and crisis bifurcations. The closer the operating point was to a critical transition, the stronger the amplification. In the reported data, noise near saddle-node and crisis points could increase by approximately 30 dB, i.e., by about three orders of magnitude in amplitude [11].

The amplification was most pronounced at the corresponding subharmonic frequency of each periodic state. This reflects the dynamical selectivity of the laser: fluctuations are not amplified uniformly at all frequencies but most strongly in the channels associated with the approaching periodic instability. Near a period-doubling bifurcation, amplification was stronger for smaller input-noise levels, consistent with earlier work on small-signal amplification near bifurcations [4].

5.3 Theoretical interpretation and wider context

Numerical simulations using the EDFL model reproduced the experimental rise in spectral noise near saddle-node bifurcations. The fact that the same model also reproduced the relaxation-frequency dependence strengthened the interpretation that the observed effect originates in nonlinear EDFL dynamics rather than in frequency-dependent noise generation by the pump source [11]. Fig. 4 shows an experimental and theoretical comparative of the noise amplification obtained for frequency modulation variation.

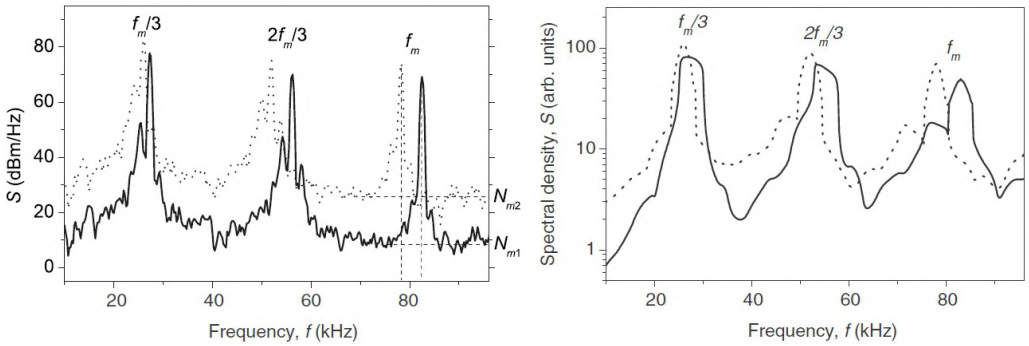


Figure 4: Experimental power spectrum analysis (left) and theoretical (right) comparison of the noise amplification obtained for frequency modulation variation, [11].

The general idea of critical amplification has relevance beyond lasers. Noise growth near bifurcations can be related to critical slowing down, reduced restoring forces, and increased susceptibility. Such behavior has been discussed in nonlinear optical systems, climate variability, population dynamics, and excitable systems [3, 5]. Yet, early-warning applications must be formulated carefully. A fluctuation increase can signal an approaching bifurcation only if the relevant control parameter, forcing statistics, and measurement chain are sufficiently stable. The EDFL provides a valuable testbed for determining which indicators remain reliable under controlled but realistic noise conditions.

6 Control of basins of attraction in a multistable fiber laser

The article *Control of basins of attraction in a multistable fiber laser* adds a global phase-space perspective to the preceding studies of hopping and critical amplification. Rather than asking only which periodic responses appear in a measured trace, Pisarchik and Jaimes-Reategui [14] investigate how their basins change under deterministic and stochastic pump perturbations. The distinction is important: failure to observe an attractor does not establish its destruction, because its basin may be small or inaccessible to the experimental preparation protocol. The new evidence in this study is numerical basin mapping; its agreement with earlier experimental results on harmonic control supports, but should not be confused with, direct experimental measurement of the basins.

6.1 Physical model and connection to earlier control studies

The study builds on the proposal that slow parameter modulation can remove an unwanted attractor through a boundary crisis, rather than simply transfer a trajectory to another state [15]. In an EDFL experiment, additional weak harmonic modulation had already been shown to eliminate one or two stable limit cycles, with the outcome depending on the control frequency and amplitude [16]. These two precedents are references 13 and 26, respectively, in the basin-control article. The subsequent basin calculations examine the phase-space organization behind that experimentally observed selection.

The numerical description uses two rate equations for the intracavity radiation variable P and the longitudinally averaged upper-level population N, derived from an erbium-level scheme that includes excited-state absorption and spontaneous emission into the fundamental laser mode, as shown in Figure 5 [14]. Its modeling antecedent, reference 27 of that article, connected pump-modulated EDFL dynamics with coexisting periodic and chaotic responses through experimental and theoretical bifurcation diagrams [20]. Importantly, the basin-control model explicitly excludes mechanisms for autonomous self-pulsing; its periodic responses are generated through pump modulation [14]. It should therefore not be treated as an interchangeable transcription of the more elaborate model used in the separate 2009 prebifurcation study.

In the article's normalization, the unmodulated pump parameter is $p = 7.4 \times 10^{19}\,\mathrm{s}^{-1}$, and the relaxation-oscillation frequency is approximately 30 kHz. The principal basin calculations use driving frequency $f_d = 70.2$ kHz and modulation depth $m_d = 0.8$, where the responses $P1$, $P3$, and $P4$ coexist [14]. These values specify a particular operating point, not universal thresholds for EDFLs. In particular, the pump parameter expressed in s^{-1} should not be inserted as a power in watts into a differently normalized model.

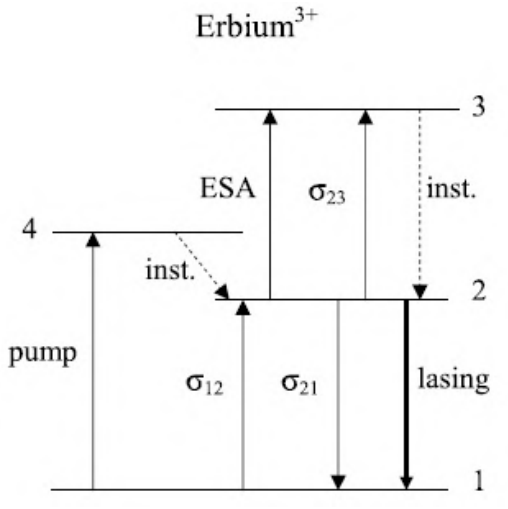


Figure 5: Energy Erbium diagram, [14].

6.2 Harmonic control and destruction of competing basins

The control protocol introduces a second sinusoidal signal into the depth of the principal pump modulation. Using the notation of the source, the resulting pump is

$$P_p(t) = p\left\{1 - \left[m_d^0 - m_c \sin(2\pi f_c t)\right] \sin(2\pi f_d t)\right\}, \tag{10}$$

where m_d^0 is the baseline modulation depth and m_c and f_c are the amplitude and frequency of the control signal [14, Eq. 6]. Thus, the control modulates the driving amplitude rather than merely adding a second independent pump tone. This distinction matters when reproducing the excitation electronically or numerically.

As the control is increased, the driven responses change their extent and structure in phase space. The authors interpret attractor annihilation through the development of a two-frequency response, possible further bifurcations, and eventual collision with a basin boundary. Control-frequency dependence is pronounced: the smallest amplitudes required for annihilation occur below the relevant resonance frequency, consistent with a nonlinear rather than purely linear response [14]. The earlier theoretical work provides the underlying boundary-crisis interpretation, while the EDFL basin maps make the associated loss of accessible initial conditions explicit [15, 14].

Two reported parameter sets illustrate the outcome. At $m_c = 0.128$ and $f_c = 2.6\,\text{kHz}$, the $P4$ attractor and its basin disappear while $P1$ and $P3$ remain. At $m_c = 0.38$ and $f_c = 2.8\,\text{kHz}$, both higher-period responses are removed, leaving $P1$ throughout the sampled initial-condition domain [14, Fig. 6(c, d)]. The significance of these maps is that selection is not demonstrated only for one trajectory: many initial conditions are tested after applying control. Nevertheless, finite numerical basin sampling does not constitute an exhaustive mathematical proof over an unbounded phase space.

6.3 Weak noise and probabilistic basin assignment

The stochastic protocol is different from the harmonic control above. The pump is written as

$$P_p(t) = p\left[1 - m_d \sin(2\pi f_d t) + \eta\zeta(t)\right], \tag{11}$$

where η controls the perturbation amplitude and the numerical random variable satisfies $\zeta \in [-1, 1]$ [14, Eq. 7]. The source describes this forcing as white noise. A reproduction should preserve its implemented sampling and bandwidth rather than silently substitute a Gaussian Wiener increment, whose normalization would require an additional specification.

The authors focus on weak forcing, described as $\eta < 0.1$, for which sustained intermittency is not observed under their simulation conditions; their statistical illustration also includes the boundary value $\eta = 0.1$ [14]. In this regime, noise can redirect a transient toward a different final periodic response without producing repeated hopping after that response is reached. Consequently, the object being measured is the distribution of outcomes across repeated preparations, not the residence-time distribution along a single intermittent trajectory.

Table 3: Distinct control outcomes in the basin study. Conditions and results are taken from Pisarchik and Jaimes-Reategui [14]; the baseline is $m_d^0 = 0.8$ and $f_d = 70.2\,\text{kHz}$.

Protocol	Reported condition	Outcome and evidential scope
No additional control	$m_c = 0$, $\eta = 0$	Coexisting $P1$, $P3$, and $P4$ with distinct basins.
Harmonic control	$m_c = 0.128$, $f_c = 2.6\,\text{kHz}$	$P4$ and its basin disappear in the numerical map.
Harmonic control	$m_c = 0.38$, $f_c = 2.8\,\text{kHz}$	Only $P1$ remains in the sampled domain.
Weak stochastic forcing	Low-noise regime described by $\eta < 0.1$	Outcome distributions change across repeated preparations without sustained hopping in the reported regime.

For each noise amplitude, the basin calculation is repeated 100 times over the initial-condition region shown in the source's Fig. 6. Each repetition yields a count of points assigned to each periodic state, and the resulting ensemble defines a distribution of basin-point counts [14, Fig. 7]. The method can be summarized, using notation introduced here for clarity, as

$$B_i^{(r)}(\eta) = \sum_{j=1}^{M} \mathbf{1}\{\mathcal{C}_r(\mathbf{x}_{0,j};\eta) = i\}\,, \qquad i \in \{1,3,4\}, \tag{12}$$

where M is the number of sampled initial conditions, r indexes a repeated noisy basin calculation, and $\mathcal{C}_r$ denotes classification after the transient. Equation (12) restates the counting protocol; it is not an additional laser evolution equation or a fitted result. For a fixed uniformly sampled domain, $B_i^{(r)}/M$ is a sampled basin fraction, whose numerical value depends on the domain and classification protocol.

6.4 Statistical findings and limits of the resonance interpretation

The distributions change systematically with noise amplitude. Their most probable basin-point counts generally increase for $P1$ and $P3$ and decrease for $P4$, approximately linearly over the explored range [14]. At the same time, the probabilities associated with particular counts vary nonmonotonically. For example, at $\eta = 0.1$ the paper reports a probability of approximately 30% for a $P1$ count near 1.3×10^3, compared with approximately 10% for a count near 1.9×10^3 [14]. These are probabilities of obtaining specified counts across repeated basin maps; they are not probabilities that a single laser trace spends 30% or 10% of its time in $P1$.

The authors describe maxima and minima in the probability distributions as resonance-like and suggest a possible connection with stochastic resonance [14]. This wording should remain qualified. Their reported evidence concerns the statistics of basin assignment, rather than a demonstrated optimum in signal-to-noise ratio or a measured matching of transition times to a periodic signal. Accordingly, the result establishes nonmonotonic statistical sensitivity to noise, while a specific stochastic-resonance mechanism would require further diagnostics.

6.5 Connection to extreme events and information processing

This study provides a useful distinction between three operations: removing a competing attractor, biasing the response selected after a transient, and sustaining transitions among surviving states. Harmonic annihilation concerns the first; the weak-noise basin analysis concerns the second; the hopping and multistate-intermittency studies concern the third [14, 10, 13]. A change in output-state statistics should therefore not automatically be interpreted as attractor destruction.

The same distinction clarifies the transition to extreme-event physics. The presence of a high-amplitude branch and the accessibility of its basin help organize possible excursions, but the 2009 basin study does not itself establish rogue-wave statistics; that evidence belongs to the subsequent extreme-pulse studies [12, 13]. Likewise, probabilistic basin selection provides a conceptual precursor to state-selective optical logic, not a demonstration of a working logic gate [17]. For future devices, the combined results suggest comparing the reliability of deterministic elimination of unwanted states with deliberate probabilistic selection, while measuring reset dependence, switching latency, and output errors. This last comparison is a research direction motivated by the reviewed results rather than a performance claim made by the basin-control article. Figure 6 shows four stages, from all present attractors to the annihilation of the less probable ones, in the system controlled on the P1 attractor.

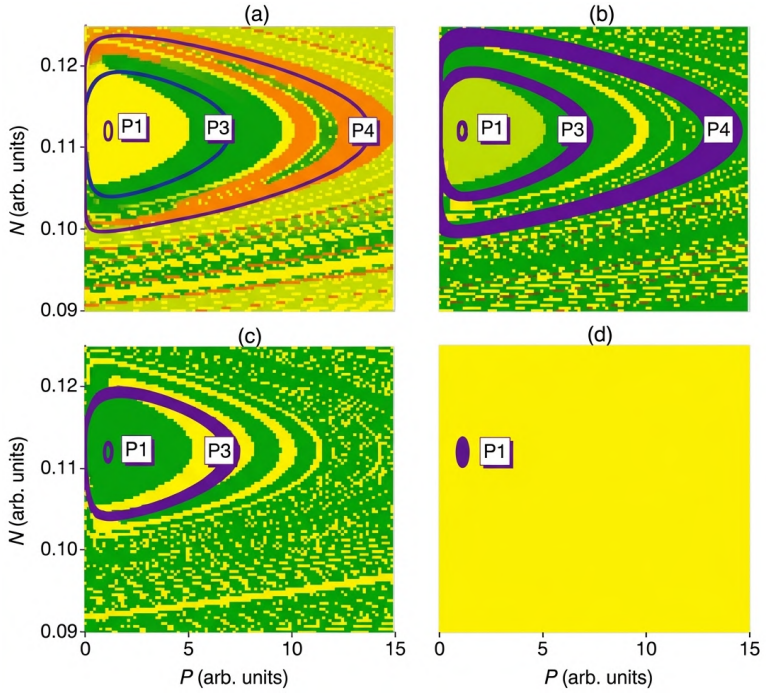


Figure 6: Annihilation of P3 and P4 attractors, [14].

7 Rogue Waves in a Multistable System

7.1 Extreme events in optics

The term "rogue wave" refers to a rare event of exceptional amplitude whose probability is much larger than expected from a simple Gaussian background model. The concept originates in ocean-wave science but has become important in optics after the observation of extreme pulses in nonlinear fiber systems [21]. In optical contexts, several mechanisms may generate extreme events, including modulation instability, nonlinear focusing, soliton interactions, chaotic dynamics, and state switching. The EDFL work reviewed here identifies a mechanism centered on multistability and noise-induced transitions [12].

7.2 Rare excursions to high-amplitude periodic states

In *Rogue Waves in a Multistable System*, the EDFL was operated in a region where $P1$, $P3$, and $P4$ coexist. The pump current received both harmonic modulation and low-pass-filtered noise. A rare event was observed when the laser left the ordinary $P1$ response and briefly entered the large-amplitude $P4$ state for several periods before returning to $P1$. The average time between events was reported to be about 30 s under the explored conditions [12].

This observation provides a physically specific interpretation of a rogue pulse. The event is not an isolated amplitude fluctuation around a single attractor; it is a transient visit to a different, coexisting dynamical regime. Such a mechanism makes the event probability controllable through the noise parameters and the underlying basin geometry. It also implies that a large-amplitude event can have a recognizable precursor in terms of state-space movement, even if that precursor is difficult to infer from a scalar intensity measurement alone.

7.3 Statistical evidence and non-Gaussian tails

The rogue-wave interpretation was supported by probability density functions of peak intensity. The large peaks appeared far more often than expected under Gaussian statistics, producing a heavy-tail signature [12], Fig. 7. This statistical criterion is essential because visual inspection alone cannot establish whether a high pulse is genuinely anomalous relative to the background distribution.

In numerical simulations, the probability of a calculated period-four rogue event was very small, and the probability maps in noise-amplitude–cutoff-frequency space showed that high-amplitude states became more likely

as the noise cutoff approached the relaxation frequency. The experimental and numerical results thus agree on the key point: extreme events emerge from an interplay between stochastic modulation and deterministic nonlinear multistability.

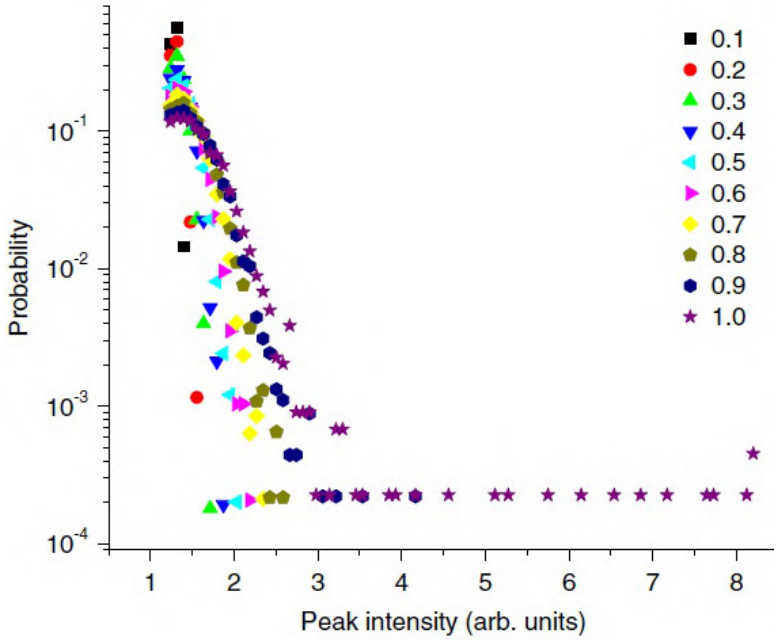


Figure 7: Non-Gaussian heavy-tail rogue-wave signature in numerical results, [12].

7.4 Relation to other rogue-wave mechanisms

The EDFL mechanism should be placed in the broader rogue-wave literature without conflating distinct processes. In ocean models, nonlinear wave interactions and modulation instability can create large transient waves [22, 23]. In optical-fiber experiments, nonlinear propagation and soliton dynamics can produce extreme pulses [21]. In the EDFL case, the central mechanism is noise-assisted switching among coexisting attractors. These mechanisms may share statistical signatures but differ in their dynamical origin. A major contribution of the EDFL studies is to show that multistability provides a concrete route to heavy-tailed pulse statistics.

8 Multistate Intermittency and Extreme Pulses in a Fiber Laser

The 2012 article *Multistate intermittency and extreme pulses in a fiber laser* extended the rogue-wave study by examining how the amplitude and spectral content of noise regulate the occupancy of periodic states [13]. The work is central to the present review because it converts the qualitative claim that "noise matters" into a parameter-dependent control map.

8.1 Stochastic modulation

The pump modulation was represented as

$$P_p(t) = p\,[1 - m_d \sin(2\pi f_d t) + \eta G(\zeta, f_n)]\,, \tag{13}$$

where η is the noise amplitude, G is a zero-mean random function, ζ denotes the random input, and f_n is the low-pass cutoff frequency. White noise was filtered with a discrete low-pass Butterworth filter. This formulation emphasizes that the perturbation has at least two physically distinct controls: intensity and bandwidth.

For small noise amplitude, the initially selected $P1$ attractor remained stable while other attractors could coexist. For larger amplitude, the laser entered intermittent regimes. Depending on the noise parameters, it switched between $P1$ and $P3$, among $P1$, $P3$, and $P4$, or among all four periodic states. The period-five response was notable because it

appeared only in the intermittent regime under the explored conditions, indicating that noise can make otherwise inaccessible or unstable dynamics observable [13].

8.2 Spectral selectivity of noise-induced switching

The major result is that the low-frequency content of noise controls access to high-amplitude subharmonic responses. In the numerical analysis, $P4$ occurred only when the cutoff frequency was below 1 MHz and $P5$ only below 200 kHz. The boundaries of intermittency regimes had minima close to the relaxation frequency of the EDFL, around 30 kHz [13]. This reveals a resonance-like susceptibility: filtered noise is especially efficient when it contains temporal components compatible with the laser's intrinsic dynamics.

The result is conceptually important because it rejects a simple variance-based view of stochastic forcing. Two noise signals with the same amplitude can have qualitatively different effects if their correlation time or spectral content differs. In a nonlinear oscillator, the temporal organization of fluctuations can determine whether they merely perturb a periodic orbit or drive the system across basin boundaries.

8.3 Extreme pulses as rare state occupation

The probabilities of $P4$ and $P5$ pulses increased as the cutoff frequency decreased, while the probability of $P1$ decreased. However, high amplitude alone does not define an extreme event. The authors stressed that such pulses should be treated as extremes only within a region where their occurrence probability is low [13]. This is a rigorous and useful distinction: changing noise parameters can turn a formerly rare event into a common state, at which point it no longer represents a statistical extreme even though its amplitude remains large.

The paper therefore supplies a blueprint for extreme-event engineering. One can map the parameter region where large pulses are both accessible and rare, then tune the noise spectrum to increase or suppress their probability. This framework is potentially relevant to the design of rare-pulse sources, to the avoidance of dangerous excursions in laser systems, and to the general study of extremes in multistable nonlinear systems.

9 Harnessing Multistability: A Novel Approach to Optical Logic Gate Construction Using Erbium-Doped Fiber Lasers

The 2024 article *Harnessing Multistability: A Novel Approach to Optical Logic Gate Construction Using Erbium-Doped Fiber Lasers* moves from analysis to application [17]. Its central proposal is to use noise-induced multistate intermittency as a mechanism for selecting logical operations.

9.1 Dynamical logic and chaos computing

Dynamical systems can implement logic if distinct attractors or responses are assigned to output states. This idea has been developed in chaos computing and nonlinear circuit research [24, 25, 26]. Systems with coexisting attractors are attractive because they can support multiple functional states within one physical device. Logic gates and memory elements have been demonstrated or proposed in nonlinear circuits, cavity magnonics, and optical systems [27, 28, 29].

The EDFL proposal differs from schemes based exclusively on deterministic digital forcing. Here, the laser's noise-controlled intermittent state determines which logic operation is active. The four coexisting periodic states are associated with four logic functions: $P1$ with OR, $P3$ with AND, $P4$ with NOR, and $P5$ with NAND [17].

9.2 Noise-controlled probability balancing

The article uses the normalized EDFL model to locate a multistable region where $P1$, $P3$, $P4$, and $P5$ coexist near a modulation frequency of 80 kHz. With low-pass-filtered noise, the laser undergoes a progression from a single state to two-state, three-state, and four-state intermittency. The occurrence probability of each period was mapped over noise intensity and filter-frequency parameters [17].

A critical design objective is to find regions in which the probabilities of the periodic states are comparable. If one state dominates, then the corresponding logic operation would be selected disproportionately often. More balanced occupation makes it possible to generate less biased state sequences and to use the local maxima of the laser signal as a dynamical selector of logic operations 8. DFA was employed to identify correlated regimes and to characterize the temporal organization of the intermittent signal [17, 30].

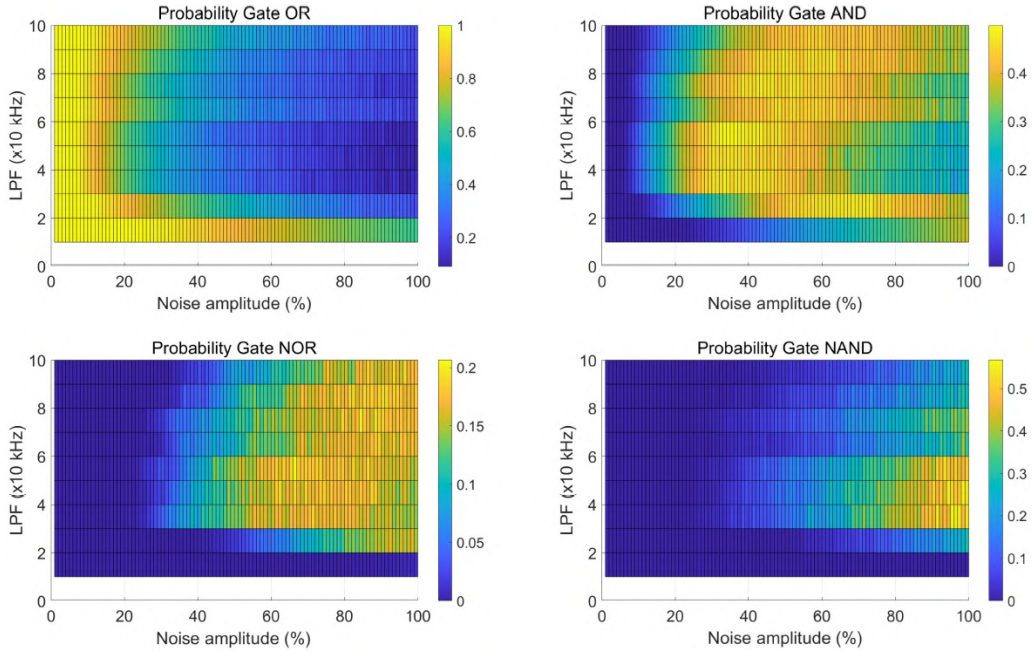


Figure 8: Hopping multistate intermittency regime as a function of noise intensity $\eta \times 10^2$ and a low pass filter for frequency $f_n \times 10$ kHz, [17].

9.3 Potential applications and limitations

The proposal includes an experimental implementation concept involving a function generator, noise generator, laser driver, EDFL cavity, photodetector, and data-acquisition system. The state-dependent amplitude of the laser output would select the logical operation performed on two digital inputs. Beyond logic gates, the authors point to potential use in pseudo-random number generation, encryption, simulations, and optimization [17].

A rigorous review must separate promise from demonstrated performance. The study is numerical and proposes an experimental configuration. It does not yet establish gate speed, error rate, cascaded operation, energy consumption, or robustness to uncontrolled intrinsic noise. These are important next steps. Nevertheless, the work demonstrates a general principle: multistable photonic dynamics can be functionalized when noise is treated as a tunable state-selection input rather than as an uncontrolled disturbance.

10 Stochastic Cloning of Dynamical Systems with Hidden Variables

The 2025 study *Stochastic cloning of dynamical systems with hidden variables* introduces a data-driven perspective on noisy nonlinear systems [18]. It uses reservoir computing to reconstruct the response of stochastic systems driven by known external noise while only part of the internal dynamics is observed.

10.1 Strong versus weak cloning

A strong clone reproduces the trajectory of the target system under the same external noise realization. A weak clone reproduces selected statistical properties, for example distributions of activation intervals, without requiring pointwise trajectory agreement. The distinction is fundamental. Strong cloning requires a deterministic functional mapping from the external input to the observed response. If the same forcing applied to identical systems with different initial conditions does not make them converge, then the response is not uniquely determined by the forcing and exact trajectory cloning is impossible [18].

The study formalizes weak cloning through agreement of moments or relevant statistical metrics between the true and reconstructed processes. This viewpoint is appropriate for stochastic or partially observed systems, where a probabilistic model can be scientifically useful even if it cannot predict individual future events exactly.

Table 4: Noise functions, observables, and applications in the reviewed EDFL studies.

Role of noise	Primary observables	Consequence or application
Perturbation	Spectral background, amplitude fluctuations	Stability limitation; baseline characterization
Critical probe	Spectral noise near bifurcations	Detection of enhanced susceptibility and approaching transitions
Switching mechanism	State probabilities, residence times, transition sequences	Noise-induced attractor hopping and multistate intermittency
Extreme-event regulator	Peak-intensity PDFs, waiting times, probability maps	Control or suppression of rare high-amplitude pulses
Information resource	Periodic-state labels, logic outputs, statistical metrics	Optical logic, pseudo-random sequences, weak stochastic cloning

10.2 Reservoir-computing architecture

The reservoir receives the external noise, the measured system response, and delayed copies of both. A recurrent hidden layer transforms the inputs nonlinearly, and a trained readout produces the predicted signal. Delay-coordinate embedding enriches the representation of partially observed dynamics [18]. Reservoir computing is well suited to nonlinear temporal systems because it can approximate complex input–output mappings without explicitly estimating the full governing equations [31, 32].

Previous work has shown that RC can infer unmeasured variables in chaotic systems, forecast large spatiotemporally chaotic dynamics, construct data-driven digital twins, and predict critical transitions [33, 34, 35, 36]. The stochastic-cloning framework adds a useful theoretical criterion: it identifies when trajectory-level prediction is physically feasible and when only statistical reproduction should be expected.

10.3 Application to the stochastic EDFL

The article examined a stochastic EDFL model with laser intensity and population inversion as state variables. Only the externally injected noise and laser intensity were supplied to the RC; inversion was treated as hidden. Exact prediction was not achieved. The best strong-prediction accuracy remained limited even after adding delayed inputs. Nevertheless, the distribution of interspike activation intervals of the RC output closely matched the distribution for the original EDFL signal, yielding high weak-cloning performance [18].

The authors then performed an experimental verification with a noise-driven EDFL. The weak clone reproduced key statistical properties, although background measurement noise limited the reconstruction quality. This result gives a realistic perspective on data-driven modeling of noisy lasers. A model can be useful for predicting distributions, activation statistics, or risk measures even when the exact pulse sequence is not reproducible.

11 Synthesis: A Hierarchy of Noise Functions in Multistable EDFLs

The studies reviewed above support a hierarchy of roles for noise in EDFLs. First, noise is a *perturbation*: it broadens signals and can destabilize a desired operating state. Second, it is a *probe*: near bifurcations, amplified fluctuations reveal increasing susceptibility. Third, it is a *transition mechanism*: it enables hopping across basin boundaries and creates multistate intermittency. Fourth, it is an *extreme-event control*: through amplitude and filtering, it regulates the probability of rare high-amplitude excursions. Fifth, it is an *information resource*: state occupancy can select logic operations and drive statistical inference.

This hierarchy also identifies experimental requirements. A credible noise-control study must specify the injection point, amplitude calibration, spectral filtering, probability distribution, sampling rate, measurement bandwidth, initial-condition protocol, state-classification method, and observation duration. Without this information, it is difficult to distinguish a true change in nonlinear dynamics from a change in measurement conditions or forcing statistics.

12 Open Problems and Future Directions

12.1 Transition matrices and basin-resolved experiments

Future work should construct state-to-state transition matrices as functions of noise amplitude and correlation time. Such matrices would quantify whether transitions are symmetric, whether particular states act as hubs, and whether direct transitions are suppressed by phase-space structure. Combining these measurements with numerical basin maps and unstable invariant-set calculations would clarify the mechanisms behind hopping and saturation-like noise transfer.

The 2009 basin calculations also motivate a separate repeated-preparation experiment at noise levels below the observed hopping regime [14]. Such a test would estimate the probability of selecting each response following a controlled reset and compare it with finite-time occupation probabilities measured after selection. Because population inversion is not directly initialized or observed in the original experiments, agreement with a simulated basin map must account for the experimentally accessible preparation ensemble rather than assume uniform sampling of the full model state space.

12.2 Early-warning indicators in photonic systems

The observed prebifurcation amplification motivates a systematic comparison of candidate early-warning signals: spectral background, variance, autocorrelation, recovery time, residence-time changes, and symbolic entropy. EDFLs could serve as benchmark systems because their control parameters and noise injection can be manipulated reproducibly. The objective should not be to identify a universal indicator, but to establish operating conditions under which a given observable provides reliable warning of a specified transition.

12.3 Extreme-event forecasting and control

The multistable rogue-wave mechanism suggests that extreme events may be forecast probabilistically from proximity to basin boundaries and state-occupation statistics. A practical research program would measure conditional probabilities of high-amplitude excursions given recent dwell times, spectral fluctuations, or filtered-noise history. Reservoir computing and physics-informed models could be compared for this task. The relevant metric is likely not pointwise prediction but calibrated event probability and false-alarm rate.

12.4 Experimental optical logic

The logic proposal needs experimental validation under controlled and uncontrolled noise. Important metrics include gate-selection error, latency, repeatability, state-recognition robustness, effect of finite detector bandwidth, energy cost, and compatibility with cascaded photonic circuits. An intermediate demonstration could implement a single state-selected operation with repeated trials and full uncertainty analysis before moving to four-gate functionality.

12.5 Hybrid physics–machine-learning models

The stochastic-cloning results motivate hybrid approaches in which a reduced EDFL model supplies physically meaningful coordinates while a reservoir or other learning system captures unresolved effects. Such models may improve statistical prediction without overstating trajectory-level predictability. They could also identify which additional measurements—for example pump-current fluctuations, polarization information, or spectral components—most improve observability of the hidden population-inversion dynamics.

13 Conclusions

The reviewed works establish the diode-pumped erbium-doped fiber laser as a versatile laboratory for the study of noise in nonlinear dynamical systems. The EDFL supports multistability among periodic states, and this deterministic structure allows external noise to produce organized effects: attractor hopping, changes in state probability, enhanced fluctuations near bifurcations, and rare high-amplitude excursions with rogue-wave statistics. The response depends not only on noise amplitude but also on its spectral content, especially relative to the intrinsic relaxation time scale of the laser.

Basin-resolved control supplies the connection between state accessibility and state elimination. Harmonic modulation can remove competing attractors together with their sampled basins, whereas weak stochastic modulation can bias preparation outcomes without sustained intermittency in the reported regime [14]. Preserving this distinction prevents a change in observed state probability from being mistaken for a change in the number of underlying attractors, and helps frame both extreme-event control and reliable photonic state selection.

The review also emphasizes a methodological lesson. Brownian-like spectra, DFA exponents, and heavy-tailed distributions do not uniquely establish stochastic origin. Deterministic systems can exhibit similar signatures, so physically meaningful interpretation requires controlled forcing, validated models, symbolic diagnostics, and carefully designed statistical tests. Ordinal-pattern analysis and reservoir-based stochastic cloning provide complementary tools for this purpose.

Finally, multistability and noise can be exploited rather than merely tolerated. Noise-controlled occupation of coexisting EDFL states offers a route toward reconfigurable optical logic. When exact trajectories are not predictable because of hidden variables and stochastic influences, reservoir computing can still provide weak clones that reproduce relevant statistics. Taken together, these results show that noise is not simply an imperfection in nonlinear photonics. Properly characterized and controlled, it is a tunable probe of criticality, a mechanism for state selection, a driver of rare events, and a resource for photonic information processing.

Declaration of Generative AI and AI-Assisted Technologies in the Manuscript Preparation Process

During the preparation of this review, the authors used Perplexity AI to assist in organizing and revising portions of the text, formatting, preparing content in LaTeX, and verifying references. The authors critically reviewed and edited the material processed with the aid of AI, ensuring that all scientific claims, equations, numerical values, and bibliographic references were consistent with the sources. The authors assume full responsibility for the accuracy, integrity, and final content of the manuscript.

References

[1] Stefan Kraut, Ulrike Feudel, and Celso Grebogi. “Experimental Observation of Noise-Induced Attractor Hopping in a Multistable System”. In: *Physical Review E* 59 (1999), pp. 5253–5256. DOI: 10.1103/PhysRevE.59.5253.

[2] Ulrike Feudel. “Complex Dynamics in Multistable Systems”. In: *International Journal of Bifurcation and Chaos* 18.6 (2008), pp. 1607–1626. DOI: 10.1142/S0218127408021057.

[3] Kurt Wiesenfeld. “Noisy Period-Doubling Bifurcation”. In: *Journal of Statistical Physics* 38 (1985), pp. 1071–1097. DOI: 10.1007/BF01017865.

[4] Kurt Wiesenfeld and Bruce McNamara. “Small-Signal Amplification in Bifurcating Dynamical Systems”. In: *Physical Review A* 33 (1986), pp. 629–642. DOI: 10.1103/PhysRevA.33.629.

[5] Benjamin Lindner et al. “Effects of Noise in Excitable Systems”. In: *Physics Reports* 392.6 (2004), pp. 321–424. DOI: 10.1016/j.physrep.2003.10.015.

[6] Oleg I. Moskalenko et al. “Characteristics of Noise-Induced Intermittency”. In: *Chaos, Solitons & Fractals* 117 (2018), pp. 269–275. DOI: 10.1016/j.chaos.2018.10.026.

[7] Fortunato T. Arecchi et al. “Experimental Evidence of Subharmonic Bifurcations, Multistability, and Turbulence in a Q-Switched Gas Laser”. In: *Physical Review Letters* 49 (1982), pp. 1217–1220. DOI: 10.1103/PhysRevLett.49.1217.

[8] Michel J. F. Digonnet, ed. *Rare-Earth-Doped Fiber Lasers and Amplifiers*. New York, NY: Marcel Dekker, 1993.

[9] Oleg G. Okhotnikov, ed. *Fiber Lasers*. Weinheim, Germany: Wiley-VCH, 2012.

[10] Guillermo Huerta-Cuellar, Alexander N. Pisarchik, and Yury O. Barmenkov. “Experimental Characterization of Hopping Dynamics in a Multistable Fiber Laser”. In: *Physical Review E* 78 (2008), p. 035202. DOI: 10.1103/PhysRevE.78.035202.

[11] Guillermo Huerta-Cuellar et al. “Prebifurcation Noise Amplification in a Fiber Laser”. In: *Physical Review E* 79 (2009), p. 036204. DOI: 10.1103/PhysRevE.79.036204.

[12] Alexander N. Pisarchik et al. “Rogue Waves in a Multistable System”. In: *Physical Review Letters* 107 (2011), p. 274101. DOI: 10.1103/PhysRevLett.107.274101.

[13] Alexander N. Pisarchik et al. “Multistate Intermittency and Extreme Pulses in a Fiber Laser”. In: *Physical Review E* 86 (2012), p. 056219. DOI: 10.1103/PhysRevE.86.056219.

[14] Alexander N. Pisarchik and Rider Jaimes-Reategui. “Control of basins of attraction in a multistable fiber laser”. In: *Physics Letters A* 374.2 (2009), pp. 228–234. DOI: 10.1016/j.physleta.2009.10.061.

[15] Alexander N. Pisarchik and B. K. Goswami. “Annihilation of one of the coexisting attractors in a bistable system”. In: *Physical Review Letters* 84.7 (2000), pp. 1423–1426. DOI: 10.1103/PhysRevLett.84.1423.

[16] Alexander N. Pisarchik, Yu. O. Barmenkov, and A. V. Kir’yanov. “Experimental demonstration of attractor annihilation in a multistable fiber laser”. In: *Physical Review E* 68.6, 066211 (2003). DOI: 10.1103/PhysRevE.68.066211.

[17] Safara Bibi et al. “Harnessing Multistability: A Novel Approach to Optical Logic Gate Construction Using Erbium-Doped Fiber Lasers”. In: *Photonics* 11.2 (2024), p. 176. DOI: 10.3390/photonics11020176.

[18] Andrey V. Andreev et al. “Stochastic Cloning of Dynamical Systems with Hidden Variables”. In: *Physical Review E* 112 (2025), p. 015303. DOI: 10.1103/dynj-xqrm.

[19] Alexander N. Pisarchik and Alexander E. Hramov. *Multistability in Physical and Living Systems: Characterization and Applications*. Cham, Switzerland: Springer, 2022.

[20] Alexander N. Pisarchik et al. “Dynamics of an erbium-doped fiber laser with pump modulation: Theory and experiment”. In: *Journal of the Optical Society of America B* 22.10 (2005), pp. 2107–2114. DOI: 10.1364/JOSAB.22.002107.

[21] Daniel R. Solli et al. “Optical Rogue Waves”. In: *Nature* 450 (2007), pp. 1054–1057. DOI: 10.1038/nature06402.

[22] Miguel Onorato et al. “Freak Waves in Random Oceanic Sea States”. In: *Physical Review Letters* 86 (2001), pp. 5831–5834. DOI: 10.1103/PhysRevLett.86.5831.

[23] Miguel Onorato, Alfred R. Osborne, and Marina Serio. “Modulational Instability in Crossing Sea States: A Possible Mechanism for the Formation of Freak Waves”. In: *Physical Review Letters* 96 (2006), p. 014503. DOI: 10.1103/PhysRevLett.96.014503.

[24] Sudeshna Sinha and William L. Ditto. “Dynamics-Based Computation”. In: *Physical Review Letters* 81 (1998), pp. 2156–2159. DOI: 10.1103/PhysRevLett.81.2156.

[25] Toshinori Munakata, Sudeshna Sinha, and William L. Ditto. “Chaos Computing: Implementation of Fundamental Logical Gates by Chaotic Elements”. In: *IEEE Transactions on Circuits and Systems I: Fundamental Theory and Applications* 49.11 (2002), pp. 1629–1633. DOI: 10.1109/TCSI.2002.804540.

[26] K. Murali et al. “Reliable Logic Circuit Elements That Exploit Nonlinearity in the Presence of a Noise Floor”. In: *Physical Review Letters* 102 (2009), p. 104101. DOI: 10.1103/PhysRevLett.102.104101.

[27] P. Ashokkumar et al. “Realization of All Logic Gates and Memory Latch in the SC-CNN Cell of the Simple Nonlinear MLC Circuit”. In: *Chaos* 22 (2012), p. 063119. DOI: 10.1063/1.4754871.

[28] Rui-Cheng Shen et al. “Long-Time Memory and Ternary Logic Gate Using a Multistable Cavity Magnonics System”. In: *Physical Review Letters* 127 (2021), p. 183202. DOI: 10.1103/PhysRevLett.127.183202.

[29] Rider Jaimes-Reategui et al. “Optoelectronic Flexible Logic Gate Based on a Fiber Laser”. In: *The European Physical Journal Special Topics* 223 (2014), pp. 2837–2846. DOI: 10.1140/epjst/e2014-02270-5.

[30] Chung-Kang Peng et al. “Mosaic Organization of DNA Nucleotides”. In: *Physical Review E* 49 (1994), pp. 1685–1689. DOI: 10.1103/PhysRevE.49.1685.

[31] Herbert Jaeger and Harald Haas. “Harnessing Nonlinearity: Predicting Chaotic Systems and Saving Energy in Wireless Communication”. In: *Science* 304.5667 (2004), pp. 78–80. DOI: 10.1126/science.1091277.

[32] Mantas Lukosevicius and Herbert Jaeger. “Reservoir Computing Approaches to Recurrent Neural Network Training”. In: *Computer Science Review* 3.3 (2009), pp. 127–149. DOI: 10.1016/j.cosrev.2009.03.005.

[33] Zhixin Lu et al. “Reservoir Observers: Model-Free Inference of Unmeasured Variables in Chaotic Systems”. In: *Chaos* 27 (2017), p. 041102. DOI: 10.1063/1.4979664.

[34] Jaideep Pathak et al. “Model-Free Prediction of Large Spatiotemporally Chaotic Systems from Data: A Reservoir Computing Approach”. In: *Physical Review Letters* 120 (2018), p. 024102. DOI: 10.1103/PhysRevLett.120.024102.

[35] Lu-Wang Kong et al. “Reservoir Computing as Digital Twins for Nonlinear Dynamical Systems”. In: *Chaos* 33 (2023), p. 033111. DOI: 10.1063/5.0137822.

[36] Soroush Panahi and Ying-Cheng Lai. “Adaptable Reservoir Computing: A Paradigm for Model-Free Data-Driven Prediction of Critical Transitions in Nonlinear Dynamical Systems”. In: *Chaos* 34 (2024), p. 051501. DOI: 10.1063/5.0202054.

Editorial Board

Editor-in-Chief
Esteban Tlelo Cuautle, Instituto Nacional de Astrofísica, Óptica y Electrónica (INAOE), México

Managing Editor
Guillermo Huerta Cuellar, Centro Universitario de los Lagos, Universidad de Guadalajara (UDG), México

Production Editor
Adriana Ruiz Silva, Universidad de Sonora (UNISON), México

Copyediting
Roberto Rafael Rivera Duron, Centro Universitario de los Lagos, Universidad de Guadalajara (UDG), México

José de Jesús Barba Franco, Instituto Tecnológico José Mario Molina Pasquel y Henríquez / TECMM Tecnológico Nacional de México, México

Section Editors

- *Eric Campos Cantón*, *Applied Mathematics and Interdisciplinary Applications*, — Instituto Potosino de Investigación Científica y Tecnológica (IPICyT), México
- *Rider Jaimes Reátegui*, *Multidisciplinary Physics*, — Centro Universitario de los Lagos, Universidad de Guadalajara (UDG), México
- *Luis Javier Ontañon García Pimentel*, *Electronic, Embedded, and Hardware in Dynamical Systems*, — Universidad Autónoma de San Luis Potosí (UASLP), México.
- *Luis Gerardo de la Fraga*, *Computer and Information Systems*, — Centro de Investigación y de Estudios Avanzados del Instituto Politécnico Nacional (CINVESTAV), México.
- *Jesús Muñoz Pacheco*, *Artificial Intelligence and Cybersecurity*, — Benemérita Universidad Autónoma de Puebla (BUAP), México.
- *Everardo Inzunza González*, *Machine Learning and Edge Computing for Biomedical and Healthcare Applications*, — Universidad Autónoma de Baja California (UABC), México.

Associate Editors

- Dr. Rui Li, School of Automation Engineering, University of Electronic Science and Technology of China, Chengdu, China.

- Dr. Iclia Villordo-Jiménez, Instituto Politécnico Nacional – UPIITA, Ciudad de México, México.
- Prof. Dr. Akif AKGÜL, HITIT UNIVERSITY, Faculty of Engineering, Department of Computer Engineering, Çorum, Türkiye.
- Prof. Dr. Javier Buldú, Universidad Rey Juan Carlos (URJC) & Centro de Tecnología Biomédica (CTB), Madrid, Spain.
- Dr. Gonzalo Barajas Ramírez, Instituto Potosino de Investigación Científica y Tecnológica (IPICyT), México.
- Dr. Christos Volos, Aristotle University of Thessaloniki, Laboratory of Nonlinear Systems - Circuits & Complexity (LaNSCom), Thessaloniki, Greece.
- Prof. Dr. Sundarapandian Vaidyanathan, Vel Tech University, Research and Development Centre, Tamil Nadu, INDIA.
- Dr. Norbert Herencsar, BRNO UNIVERSITY OF TECHNOLOGY, Department of Telecommunications, Brno, Czech Republic.
- Dr. Juan Hugo García López, Centro Universitario de los Lagos, Universidad de Guadalajara (UDG), México.
- Dr. Israel Cruz Vega, Instituto Nacional de Astrofísica, Óptica y Electrónica (INAOE), México.
- Dr. Alejandro Díaz Sánchez, Instituto Nacional de Astrofísica, Óptica y Electrónica (INAOE), México.
- Dr. Jorge Antonio López Rentería, Instituto Tecnológico de Tijuana (ITT), México.
- Dr. Carlos Sánchez López, Universidad Autónoma de Tlaxcala (UATx), México.
- Dr. Isaac Campos Cantón, Universidad Autónoma de San Luis Potosí (UASLP), México.
- Dr. Everardo Inzunza González, Universidad Autónoma de Baja California (UABC), México.
- Dr. Bahia Betzabet Cassal Quiroga, Universidad Autónoma de San Luis Potosí (UASLP), México.
- Dr. Adriana Ruíz Silva, Universidad Estatal de Sonora (UES), México.
- Dr. Omar Guillén Fernández, Instituto Nacional de Astrofísica, Óptica y Electrónica (INAOE), México.
- Dr. Walter D. Leon Salas, Purdue University, Indiana, United States.
- Dr. Ernesto Zambrano Serrano, Universidad Autónoma de Nuevo León (UANL), México.

- Dr. Héctor Eduardo Gilardi Velázquez, Universidad Panamericana (UP), México.
- Dr. José Luis Echenausía Monroy, Centro de Investigación Científica y de Educación Superior de Ensenada (CICESE), México.
- Dr. Yazmin Maldonado, Instituto Tecnológico de Tijuana (ITT), México.
- Dr. Claudio Alejandro García Grimaldo, Universidad Politécnica de San Luis Potosí (UPSLP), México.
- Dr. Miguel Platas Garza, Universidad Autónoma de Nuevo León (UANL), México.
- Dr. Luis Javier Ontañón García Pimentel, Universidad Autónoma de San Luis Potosí (UASLP), México.
- Dr. Rodolfo de Jesús Escalante González, Instituto Tecnológico de San Luis Potosí (ITSLP), México.
- Dr. Juan Onofre Orozco López, Centro Universitario de Los Lagos, Universidad de Guadalajara (CU Lagos, UdG), México.
- Dr. Yair Lozano Hernández, Unidad Profesional Interdisciplinaria de Ingeniería campus Hidalgo, Instituto Politécnico Nacional (UPIIH), México.
- Dr. Pánfilo Raymundo Martínez Rodríguez, Facultad de Ciencias, Universidad Autónoma de San Luis Potosí (UASLP), México.

Instructions for Authors

Scope and Policy

The *Journal of Dynamical Systems and Complexity* (JDSC) is dedicated to advancing the knowledge of both linear and nonlinear dynamical systems. We welcome high-quality contributions, including original research articles, comprehensive reviews, and brief communications. Our scope covers theoretical developments, numerical simulations, computational algorithms, and experimental methods, with a particular interest in emerging phenomena in complex systems.

Submission Guidelines

Interested in submitting to this journal? We recommend that you review the About the Journal page for the journal's section policies, as well as the Author Guidelines. Authors need to register with the journal prior to submitting or, if already registered, can simply log in and begin the five-step process. Here you can download the template for writing your paper.

Author Guidelines

1. Submission Overview. All manuscripts must be submitted in English and represent original work not previously published or under consideration elsewhere. Submissions should include a Title Page, Abstract (max 200 words), Keywords, and the Main Text.

2. Formatting and Style File Format: Please submit your manuscript in Portable Document Format (PDF) or LaTeX format. Manuscripts should be prepared using the JDSC LaTeX template. Submissions in PDF format are required for the initial review process.

3. Figures and Illustrations Figures must be high-resolution (at least 300 DPI) and submitted as separate files (TIFF, JPEG, or EPS) or embedded clearly within the text for initial review.

   Originality: Authors are responsible for obtaining written permission to reuse any figures previously published elsewhere. Ethical Imaging Standards: Strict Prohibition of Non-Inclusive/Copyrighted Test Images: To maintain the highest ethical and professional standards, this journal prohibits the use of copyrighted or historically controversial images. Specifically, the "Lenna" (or "Lena") image is strictly forbidden. We encourage authors to use modern, open-source, and diverse datasets (e.g., Kodak, McMaster, or standard USC-SIPI alternatives) that do not carry the copyright or social baggage associated with legacy test images.

4. Data Availability Authors are encouraged to share their underlying data and code. A Data Availability Statement must be included at the end of the manuscript, detailing where the data can be accessed or why it cannot be shared.

5. Ethical Considerations Conflict of Interest: Authors must disclose any financial or personal relationships that could inappropriately influence their work. Human/Animal

Rights: Studies involving human participants or animals must include a statement of approval from an institutional review board (IRB) or ethics committee.

6. Peer Review Process This journal operates a blind peer review process. Ensure that the main manuscript file does not contain author names or affiliations to maintain anonymity during the review.

Peer Review Process

All submissions undergo a rigorous double-blind peer-review process managed by the Editorial Board to ensure the highest scientific standards.

Contact Information

For submissions and editorial inquiries, please visit our website at:
`https://revista.amesdyc.org/index.php/JDSC/index`, or;
at ediesca.conference@amesdyc.org.

Publication Note

This second issue of the
Journal of Dynamical Systems and Complexity
(Vol. 1, No. 2)
was finalized and typeset on
July 1, 2026.

The editorial process, including peer review, layout design,
and final proofreading, was concluded in
Lagos de Moreno, Jalisco, México.

All rights reserved.